Universität Bremen*

Retrieval of shipping emissions from MAX-DOAS measurements

Ableitung von Schiffsemissionen aus MAX-DOAS-Messungen

Masterarbeit

im Studiengang Physik

an der Universität Bremen,

Fachbereich 1: Physik und Elektrotechnik,

Institut für Umweltphysik (IUP)

eingereicht von: André Seyler

geboren am: 13.08.1987, Reinbek

Matrikelnummer: 2295098

Betreuer: Dr. Folkard Wittrock

Gutachter: 1. Gutachter: Prof. Dr. John P. Burrows

2. Gutachter: PD Dr. Annette Ladstätter-Weißenmayer

eingereicht am: 16.05.2014

*EXZELLENT.

Contents

List of Figures

List of Tables

1. Introduction and Motivation

"Air pollution is now the world's largest single environmental health risk. Reducing air pollution could save millions of lives." (World Health Organization, 25 March 2014)

A recent study from the World Health Organization (WHO), published on 25 March 2014, estimates that in 2012 around 7 million premature deaths were linked to air pollution exposure. This represents one out of eight of the total annually global deaths, which is more than two-times more as previously estimated. The estimated deaths due to indoor air pollution (cooking over wood, coal or dung) is about 4.3 million, due to outdoor air pollution (urban and rural sources) about 3.7 million, that cannot be simply added, since a certain fraction of those people had been exposed to both.

This becomes a burden especially for South-East Asia and the Western Pacific Region, which account for 3.3 (indoor) and 2.6 million (outdoor) of these deaths. Especially in china, the construction of new coal power plants lead to record-breaking smog conditions in Beijing and Shanghai this winter.

The WHO also stated that often unsustainable policies in transport, energy and industry, that neglect the costs for health-care, are one reason for the excessive air pollution.

Shipping traffic is one of those sectors, that faces an enormous growth (world fleet doubled since the year 2000, see Chapter 4) and contributes substantially to the emissions from the transportation sector, but lacks regulations and controls. Shipping is not enclosed in the Kyoto Protocol. However the International Maritime Organization (IMO) introduced sulfur limits for marine heavy fuels, nitrogen oxide limits for newly-built ship engines and established Emission Control Areas (ECA) in the North and Baltic Sea as well as around North America with the *International Convention for the Prevention of Pollution from Ships* (MARPOL 73/78 Annex VI).
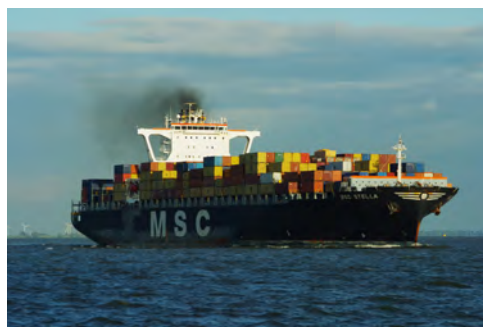
Figure 1.1.: Container ship on the river Elbe

Starting with January 2015, only 0.1 % sulfur content is allowed inside the Emission Control Areas, which, however, still is hundred times higher than the sulfur limit for car fuels. What indeed is not regulated, is the emission of particles, that are responsible for various health hazards and seem to be responsible for about 60 000 deaths annualy (Corbett et al., 2007). And not only the large oceangoing ships burning

heavy fuel oils, but also the small barges carrying the inland water transport burning ship diesel emit a large number of particles. Somehow, it is difficult to understand, why particle emissions from road transport are so strictly regulated, while ships can emit their exhausts unfiltered.

The project MeSmarT (measurements of shipping emissions in the marine troposphere), a cooperation between the University of Bremen, the German Federal Maritime and Hydrographic Agency (Bundesamt für Seeschifffahrt und Hydrographie, BSH) and the Helmholtz-Zentrum Geesthacht aims to measure ship emissions in the marine environment as well as to investigate their impact on the atmospheric boundary layer. To achieve this, the amounts of several trace gases and particles that are emitted by ships are measured with several instruments, using various measurement techniques.

Within this thesis, the MAX-DOAS (Multi Axis Differential Optical Absorption Spectroscopy) measurements of the shipping emission and air polution related atmospheric trace gases nitrogen dioxide (NO_2) and sulfur dioxide (SO_2) at the two MeSmarT measurement sites in Wedel and on Neuwerk were evaluated.

The main objectives of this thesis are:

- Carrying out a SO_2 fitting retrieval study on the data from Neuwerk and Wedel to determine the optimal fit parameter for the retrieval of SO_2 slant column densities (SCDs) from ship emissions for the MAX-DOAS measurements at both sites.

- Calculation of volume mixing ratios (VMRs) in the lowest atmospheric layer from the measured NO_2 and SO_2 SCDs with different approaches for the comparison of MAX-DOAS data with in-situ measurements:

    - applying a simple geometric approach

    - using the oxygen collison complex (O_4) SCDs measured in the UV and visible spectral range as a tracer to determine the length of the effective light path

    - using the water vapor SCD measured in the visible as a light path tracer, an approach which will be used for the first time

- Determine the wind direction dependence of the measurements by using wind speed and direction data.

- Allocate the measured emission plumes to the emitting ships by incorporation of AIS (Automatic Identification System) ship position data

- For the first time, determine emission ratios NO_2/SO_2 for single ships with MAX-DOAS measurements to compare the relative emission rates of NO_2 and SO_2.

The outline of this thesis is as follows: First, the general composition and structure of the Earth's atmosphere is introduced in Chapter 2. Chapter 3 describes the tropospheric chemistry of the investigated trace gases NO_2 and SO_2 and Chapter 4 gives information on shipping emissions. The interaction processes between light and matter are explained in Chapter 5. Chapter 6 focuses on the DOAS measurement technique, Chapter 7 on the MAX-DOAS instrument. The MeSmarT project and both measurement sites are described in Chapter 8 and Chapter 9. Chapter 10 presents the results of the SO_2 fitting retrieval study. The measurement results for Wedel and Neuwerk are shown in Chapter 11 and 12. Finally, Chapter 13 summarizes the results and gives an outlook for future tasks.

2. The Atmosphere

This chapter describes the general composition and vertical structure of the Earth's atmosphere. The relevant atmospheric chemistry is described in Chapter 3.

2.1. Composition of the Atmosphere

The Earth's thin gaseous envelope, the atmosphere, is a mixture of various chemical constituents. Although the largest part are gases, the small fraction of liquid droplets and solid aerosol particles also plays an important role.

The main constituents are the diatomic gases nitrogen (N_2) with a percentage of $78\,\%$ and oxygen (O_2) with about $21\,\%$. The next smaller fraction is the noble gas argon (Ar) with a percentage of $0.9\,\%$. These three most abundant gases as well as the other noble gases are the permanent constituents of the atmosphere with a temporal and spatial nearly constant distribution. They are characterized by a long chemical lifetime and are well-mixed in the so-called *homosphere* from the surface up to an altitude of 80–$90\,\mathrm{km}$.

Aside from the permanent constituents there is a multitude of different trace gases with more or less fluctuating concentrations and much shorter lifetimes of minutes to years. These gases are no permanent constituents and come from emissions or reactions. Despite their comparatively low concentrations, most trace gases play an important role in the radiative budget of the atmosphere, biogeochemical cycles and, as beeing mostly radicals, influence atmospheric lifetimes of other trace gases. Thereby, many trace gases like water vapor (H_2O), carbon dioxide (CO_2) or ozone (O_3) as well as liquid and solid aerosols have a crucial influence on our climate system (Brasseur, 1999; Roedel and Wagner, 2011).

The amounts of the various gases in the atmosphere can be expressed in number densitys $n = \dfrac{N}{V}$ (number of molecules per volume) or mass densitys $\rho = \dfrac{m}{V}$ (mass per volume) as well as dimensionless volume mixing ratios $\mathrm{VMR} = \dfrac{n_{\mathrm{gas}}}{n_{\mathrm{air}}}$ or mass mixing ratio $\mathrm{MMR} = \dfrac{\rho_{\mathrm{gas}}}{\rho_{\mathrm{air}}}$, respectively (Brasseur, 1999). Table 2.1 shows the main constituents of the dry atmosphere given in volume mixing ratios.

This thesis focuses on the trace gases NO_2 and SO_2 in marine environments. A detailed description of these gases is given in Chapter 3.

Table 2.1.: Volume mixing ratios of the main constituents of the dry atmosphere as well as nitrogen oxides and sulfur dioxide which were investigated for this thesis and are described in detail in Chapter 3. Values taken from Brasseur (1999).

Constituent	Chemical formula	Volume mixing ratio (VMR)
Nitrogen	NO_2	78.084 %
Oxygen	O_2	20.948 %
Argon	Ar	0.934 %
Carbon dioxide	CO_2	360 ppm
Neon	Ne	18.18 ppm
Helium	He	5.24 ppm
Methane	CH_4	1.7 ppm
Hydrogen	H_2	0.55 ppm
Nitrous oxide	N_2O	0.31 ppm
Carbon monoxide	CO	50–200 ppb
Ozone (stratosphere)	O_3	0.5–10 ppm
Ozone (troposphere)	O_3	10–500 ppb
Nitrogen oxides	$\mathbf{NO_x}$	**10 ppt–1 ppm**
Sulfur doxide	$\mathbf{SO_2}$	**10 ppt–1 ppb**

2.2. Vertical Structure of the Atmosphere

Space often seems to be very far away from us. Admittedly, 100 km (the so-called Karman-Line (Darrin and O'Leary, 2009)) is not nearby, but for many people in the world space is closer than the sea. Compared to the Earth's radius of about 6380 km, the atmosphere is a very thin layer around our planet. The International Space Station (ISS) has its orbit at 390 km altitude, Space Shuttle missions operate in heights of 300 to 400 km (Darrin and O'Leary, 2009).

The German astronaut Ulf Merbold described his view from the Space Shuttle Columbia onto the Earth's atmosphere in 1983 with the following words: *"For the first time in my life I saw the horizon as a curved line. It was accentuated by a thin seam of dark blue light – our atmosphere. Obviously this was not the ocean of air I had been told it was so many times in my life. I was terrified by its fragile appearance."* (Eddy, 2009)

The vertical profile of pressure shown in Figure 2.1 gives an idea about the vertical extend and structure of the Earth's atmosphere. Air pressure p decreases nearly exponentially with height z according to the barometric equation:

$$p(z) = p_0 \cdot e^{-\frac{z}{H}} \qquad \text{with the scale height} \qquad H = \frac{R \cdot T}{M \cdot g} \tag{2.1}$$

with the surface pressure p_0, temperature T, gravity of Earth g, the universal gas constant R and molar mass of air M (Brasseur, 1999).

The scale height H is defined as the height for which the pressure is reduced by a factor of $1/e \approx 1/3$.

Furthermore, it specifies the hypothetical height of a homogeneous atmosphere with constant surface density (Roedel and Wagner, 2011). For the Earth's atmosphere, H is in the range of 6 to 8.5 km. 50 % of the mass of the atmosphere are located in the first 5.5 km, at an altitude of 30 km even 99 % of the atmosphere can be found below (Wayne, 2006).
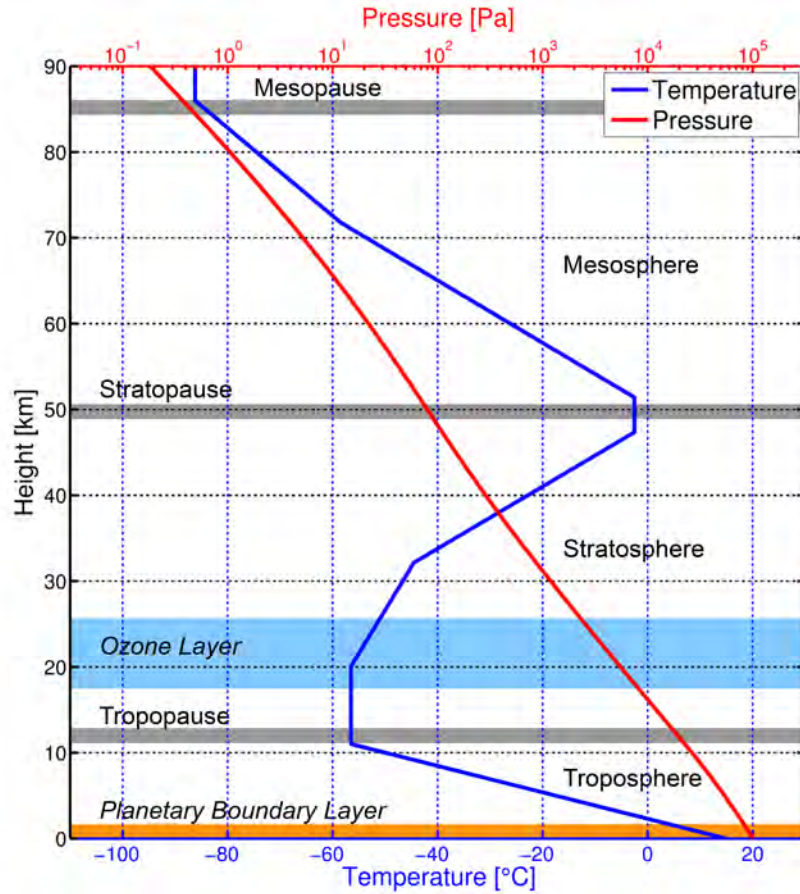
Figure 2.1.: Vertical profile of temperature and pressure for the U.S. Standard Atmosphere (1976). Note that the pressure is plotted on a logarithmic scale. The various layers of the atmosphere (tropopause height for mid-latitudes) are also highlighted.

To understand the formation of the vertical structure of the atmosphere including all (stable or unstable) layers one has to consider adiabatic processes, static stability and the concept of potential temperature.

The first law of thermodynamics states that the change of the internal energy dU in a system equals the sum of the exchanged heat δQ and the work performed on the system δW. In the case of an ideal gas the performed work is pressure-volume work and the internal energy only depends on the temperature with the specific heat capacity for constant volume C_V as a constant of proportionality (Roedel and Wagner, 2011):

$$\mathrm{d}U = \delta Q + \delta W \qquad \overset{\text{ideal gas}}{\Longleftrightarrow} \qquad C_V \cdot T = \delta Q - p \cdot \mathrm{d}V \qquad (2.2)$$

An adiabatic process is a physical process in which no heat is exchanged between the system and the surroundings, i.e. $\delta Q = 0$. This is the case when the system is well insulated or the process is very fast. For natural processes, the change of pressure or volume often takes place very quickly so that the heat transfer to the surroundings can be neglected. Adiabatic processes can be reversible when the entropy

in the system stays constant (which is called isentropic) or irreversible when entropy is produced in the system (Demtröder, 2008).

The first law of thermodynamics for an adiabatic process ($\delta Q = 0$) combined with the ideal gas law and the barometric equation (2.1) yields a term for the dry-adiabatic temperature gradient and the dry-adiabatic lapse rate Γ:

$$\Gamma = -\frac{\mathrm{d}T}{\mathrm{d}z}_{\text{adiabatic}} = \frac{M \cdot g}{C_P} \approx 1\,\mathrm{K}\big/100\,\mathrm{m} \qquad (2.3)$$

with the molar mass M and specific heat capacity for constant pressure $C_p = C_V + R$. The moist adiabatic lapse rate is always smaller (typical value: $0.5\,\mathrm{K}\big/100\,\mathrm{m}$) because of the higher heat capacity of water vapor and the additional release of latent heat caused by the condensation of liquid water(Roedel and Wagner, 2011). The potential temperature Θ is defined as the temperature that an air parcel with the actual temperature T and pressure p would have if it were compressed or expanded dry-adiabatically to the meteorological standard pressure p_s (defined as 1000 hPa or 1013.25 hPa):

$$\Theta = T \cdot \left(\frac{p_s}{p}\right)^{\frac{\kappa-1}{\kappa}} \qquad \text{with} \qquad \kappa = \frac{C_p}{C_V} = \frac{f+2}{f} \qquad (2.4)$$

with the adiabatic index κ and the degrees of freedom f. The potential temperature is a measure for the sum of potential and thermal (internal) energy and is conserved for dry-adiabatic motion. Since every air parcel has a characteristic value of Θ, one can compare the energy content of different air parcels and evaluate static stability (Holton, 2004; Roedel and Wagner, 2011).

When an air parcel is displaced upwards it has to expand due to the lower pressure there. The energy needed for this pressure-volume work is taken from the internal energy decreasing the air parcel's temperature according to the dry-adiabatic lapse rate (2.3). At this point, two cases have to be distinguished:

- The surrounding air is colder than the air parcel. This is the case when the actual (geometric) lapse rate γ of the surroundings is higher than the dry adiabatic lapse rate, i.e. $\gamma > \Gamma$. This situation is equivalent to a decrease of potential temperature with height $\left(\frac{\partial \Theta}{\partial z} < 0\right)$. The air parcel is warmer meaning it is less dense than the surrounding air and will continue rising up, vice versa for a downward displacement. This is an *unstable* condition.

- The surrounding air is warmer than the air parcel. This is the case when the actual lapse rate is smaller than the dry adiabatic lapse rate ($\gamma < \Gamma$), equivalent to a vertically increasing potential temperature $\left(\frac{\partial \Theta}{\partial z} > 0\right)$. The air parcel is colder meaning more dense than the surrounding air and will fall back. This leads to so-called buoyancy oscillations around the equilibrium. This condition is *statically stable* and causes a stable stratification. If warm air lays above cold air, which means that the temperature gradient is not only less negative but rather positive, the stability of the stratification can be enormous high inhibiting vertical exchange. This is called an inversion.

- A situation with $\gamma = \Gamma$ and $\frac{\partial \Theta}{\partial z} = 0$ is statically neutral.

(Roedel and Wagner, 2011; Holton, 2004)

The vertical temperature profile divides the atmosphere into various layers shown in Figure 2.1. The lowest layer is the *troposphere* where temperature decreases nearly linearly with height. It extends up to 18 km in the tropics, up to 12 km in the mid-latitudes and up to 6–8 km at the poles and contains

approximately 85–90 % of the mass of the entire atmosphere. Convection due to the heated surface often causes the troposphere to be a highly dynamic, unstable and well-mixed layer. Most of the known weather phenomenons happen in this layer showing its high variability.

The lowest part of the troposphere, where surface interactions play an important role, is called the *planetary boundary layer* (PBL). The mean vertical extend of the PBL is about 1 km but it can vary between a maximum value of 2 km and a minimum value of several meters depending on daytime and meteorological conditions (Brasseur, 1999).

At night, when no sunlight heats the ground, no convection takes place and the cold dense air can fall down. The surface is cold as well due to radiative cooling. A stable stratification is formed and the positive temperature gradient near to the surface causes a nightly ground inversion. In urban areas, this effect is much smaller due to the warmer surface. However, some turbulent mixing still happens at night in the lower part of the planetary boundary layer due to wind. After sunrise, the surface is heated and convection sets in eroding the stratification. On a cloudless day this convective mixing can capture the whole PBL up to 1–2 km. On clouded days or in winter time the developing mixed layer is much thinner.

Above this mixed layer, there is a stable layer called the entrainment layer which acts as a cap. This affects also the distribution of pollutants in the troposphere. Since their sources are mostly located at the ground they are trapped in the mixed layer. This is the reason, why pollutant and trace gas levels at the ground can be higher during the night time (Stull, 1994).The troposphere above the planetary boundary layer is called the *free troposphere*. The radiative cooling due to water vapor causes a temperature minimum at the top of the troposphere which is called the *tropopause*(Roedel and Wagner, 2011).

However, this diurnal variation of the boundary layer does not exist in marine environments due to the very stable water temperature on daily or weekly time scales. This is caused by the high heat capacity of water, which inhibits warming or cooling on short time periods. Water temperature changes happen on monthly time scales, so only a seasonal variation of the marine boundary layer exists and no diurnal cycle. Additionally, the annual cycle of the ocean's water temperature is delayed one or two months to the annual air temperature variation. In spring, when the water is still cold, the air above the water can be considerable warmer, causing a stable stratification. In autumn the water is still warm, but the air above can be significantly colder, leading to an unstable marine boundary layer. (Emeis, 2011; Böttcher, 2013)

The *stratosphere* above is a very stable layer with a positive temperature gradient (Brasseur, 1999). This stratospheric inversion is caused by heating due to absorption of solar UV and visible radiation in the ozone layer, which contains 90 % of the atmospheric ozone (Wayne, 2006). The stratosphere extends up to the *stratopause* in 50 km altitude where the temperature has a local maximum. The next layer extending from 50 km to 85 km is the *mesosphere* where temperature decreases again. According to conditions similar to the troposphere, this layer again shows a lot of vertical mixing and is dynamically unstable (Brasseur, 1999). The *mesopause* at about 85 km is characterized by the lowest temperature of the whole atmosphere. Above the mesopause, in the *thermosphere*, temperature increases again. This layer is heated due to absorption of high energetic solar UV radiation by oxygen molecules reaching a maximum temperature of 1200 to 1500 K with a large diurnal variation (Roedel and Wagner, 2011). The *exosphere* above is the transition layer to space (Brasseur, 1999).

3. Tropospheric Chemistry

This chapter focuses on the tropospheric chemistry of the trace gases NO_2 and SO_2 and air pollution in general, while shipping emissions are described in Chapter 4.

3.1. Nitrogen Oxides (NO_x)

The term *nitrogen oxides* ($NO_x = NO + NO_2$) refers to the two reactive nitrogen compounds nitric oxide (NO) and nitrogen dioxide (NO_2), which rank among the most important trace gases in atmospheric chemistry (Seinfeld and Pandis, 2006). Nitrogen oxides play an important role in ozone (O_3) production and depletion in the stratosphere and also in the troposphere, where high ozone concentrations are toxic for living organisms. Moreover, together with sulfur dioxide (SO_2), tropospheric NO_x is an important precursor for acid rain and photochemical smog (Brasseur, 1999).

Natural sources for nitrogen oxides in the troposphere are microbial production in fertilized soils and, with very uncertain amounts, lightning due to thunderstorms. These processes, which are of particular importance in the tropics, can be the most important NO_x sources in clean, rural regions. Anthropogenic sources of nitrogen oxides are, in the first place, high-temperature combustion processes of fossil fuels in industry and transportation, for example in shipping emissions (see chapter 4). Another important source is biomass burning which can be either natural (forest fires) or anthropogenic (land clearing). Aircraft engines provide an anthropogenic source of NO_x in the upper troposphere and lower stratosphere. (Brasseur, 1999; Wayne, 2006; Seinfeld and Pandis, 2006)

The fact, that the lifetime of nitrogen oxides is short compared with typical transport time scales and that the sources are mostly located at the surface results in almost no transport of NO_x from the troposphere into the stratosphere. Therefore, the main stratospheric source is oxidation of nitrous oxide (N_2O), which has a much longer lifetime and is therefore able to reach the stratosphere. In the upper troposphere, injection from the stratosphere tends to be more important than surface emissions. (Wayne, 2006; Brasseur, 1999) A very important tropospheric sink for nitrogen oxides is the reaction with the OH radical to easily soluble nitric acid (HNO_3) and subsequent wet deposition by precipitation. Also important is dry deposition and uptake by plants. In the stratosphere, photo-dissociation by UV radiation is the most important sink. (Seinfeld and Pandis, 2006; Wayne, 2006)

Table 3.1 lists numbers for the estimated global NO_x emissions given by the IPCC Assessment Reports 3 (2001) and 4 (2007).

Typical volume mixing ratios of nitrogen oxides in the planetary boundary layer range from 0.02–0.04 ppb (20–40 ppt) in remote ocean regions, to 0.2–10 ppb in rural areas, to 10–1000 ppb in cities and industrial regions (Seinfeld and Pandis, 2006).

Table 3.1.: Estimated global emission sources of NO_x for the 1990s in teragram nitrogen per year (1 Tg = 1 mio. t), numbers taken from the IPCC Assessment Reports 3 (2001) and 4 (2007)

	Emissions in Tg N per year	
Source	AR 3	AR 4
Fossil fuel combustion and industrial processes	33.0	25.6
Biomass burning (and biofuels)	7.1	5.9
Agriculture	2.3	1.6
Aircraft	0.7	
Total anthropogenic emissions	43.1	33.4
Soils (natural vegetation)	3.3	7.3
Lightning	5.0	1.1 to 6.4
Atmospheric Chemistry	< 5.0	
Total natural emissions	8.8	8.4 to 13.7
Total emissions	51.9	41.8 to 47.1

3.2. Nitrogen Dioxide (NO_2) in the Troposphere

As described above, the main (anthropogenic) source for nitrogen oxides in the troposphere is combustion at high temperatures. This process as well as lightning produce mainly nitric oxide (NO), which than reacts with ozone to form nitrogen dioxide (NO_2):

$$NO + O_3 \longrightarrow NO_2 + O_2 \tag{3.1}$$

The newly formed nitrogen dioxide molecules can be photolysed by UV radiation ($\lambda < 420\,nm$) creating ground state oxygen atoms and restoring the nitrogen monoxide:

$$NO_2 \xrightarrow{h \cdot \nu} NO + O \tag{3.2}$$

The created oxygen atom reacts mostly with molecular oxygen (O_2) forming ozone:

$$O + O_2 + M \longrightarrow O_3 + M \tag{3.3}$$

This reaction is a three-body-collision reaction meaning that an additional component M which usually is an oxygen (O_2) or nitrogen molecule (N_2) is needed for absorbing the excess energy. (Brasseur, 1999; Wayne, 2006; Seinfeld and Pandis, 2006)

The reactions 3.1, 3.2 and 3.3 form a cycle, which in the presence of daylight and neglecting other reactions, results in a dynamic equilibrium of both concentrations $[NO]/[NO_2]$ (a so-called *null-cycle*). Since transformation takes place very fast, NO and NO_2 are often summarized as NO_x (Seinfeld and Pandis, 2006).

Reaction 3.1 has a considerable activation energy ($\approx 13\,k\,J/mol$) which means that the ratio $[NO]/[NO_2]$ is larger at higher altitudes in the troposphere because of the decreasing temperature and ozone concentrations with height: ≈ 0.1 at noontime, ≈ 12 at $10\,km$. During nighttime there is no photolysis of NO_2, so almost all NO_x is available as NO_2. (Wayne, 2006; Seinfeld and Pandis, 2006)

An important sink for NO_2 in the troposphere is the reaction with the OH radical forming nitric acid

(HNO$_3$):

$$NO_2 + OH + M \longrightarrow HNO_3 + M \qquad (3.4)$$

During daylight, photo-dissociation of the nitric acid molecules can occur reversing the reaction:

$$HNO_3 \xrightarrow{h \cdot \nu} NO_2 + OH \qquad (3.5)$$

In the presence of liquid water the easily soluble nitric acid can be released from this equilibrium cycle and through subsequent wet deposition released from the atmosphere. For that reason cloud formation and precipitation is a very important sink for nitrogen dioxide in the lower troposphere and especially in the planetary boundary layer. (Brasseur, 1999)

The lifetime of nitrogen dioxide ranks between a few hours up to a day in the planetary boundary layer in summer and one to two weeks in the upper troposphere (Brasseur, 1999; Seinfeld and Pandis, 2006).

3.3. Sulfur Dioxide (SO$_2$) in the Troposphere

Sulfur is essential for living organisms on earth, it is important for assimilation (especially for plants) and released by their metabolism. The atmospheric sulfur cycle is dominated by anthropogenic activities (75 %), from which 90 % occur in the northern hemisphere. Anthropogenic sources are combustion processes using fossil fuels like coal and oil, biomass burning and roasting of sulfur ores, releasing mostly sulfur dioxide (SO$_2$) (Brasseur, 1999; Wayne, 2006). Especially the heavy fuel oils (bunker fuel), used to power ship engines, have a high total sulfur content (see Chapter 4).

The natural sources of sulfur dioxide are volcanoes and other sulfur gases like dimethyl sulfide (DMS), hydrogen sulfide (H$_2$S), carbon disulfide CS$_2$ or carbonyl sulfide (OCS). These reduced sulfur compounds are oxidized by the OH radical forming SO$_2$ as a common intermediate. A high fraction of these biogenic sulfur compounds are oceanic emissions of DMS, but terrestrial vegetation and soils contribute, too. In contrast to anthropogenic sources, the natural sources are nearly equally distributed in northern and southern hemisphere. (Brasseur, 1999; Wayne, 2006)

An important sink for SO$_2$ is the oxidation by the OH radical to sulfur trioxide (SO$_3$):

$$SO_2 + OH + M \longrightarrow HOSO_2 + M \qquad (3.6)$$
$$HOSO_2 + O_2 \longrightarrow HO_2 + SO_3 \qquad (3.7)$$

SO$_3$, which is the anhydride of sulfuric acid (H$_2$SO$_4$), is extremely hygroscopic and reacts rapidly with liquid water:

$$SO_3 + H_2O \longrightarrow H_2SO_4 \qquad (3.8)$$

The created H$_2$SO$_4$ aerosol is then released from the troposphere by wet deposition. Another path is the direct solution of SO$_2$, which is moderately soluble, in water droplets forming sulfurous acid (H$_2$SO$_3$). Producing such strong acids, sulfur dioxide, as well as nitrogen dioxide, is an important precursor for acid rain precipitation and also very important in the formation of photochemical smog (Brasseur, 1999).

The lifetime of SO_2 of approximately one week in the free troposphere is therefore based on the reaction with OH. Another very efficient sink is dry deposition, leading to a very short lifetime of about one day in a 1 km PBL, even shorter when clouds are present (Seinfeld and Pandis, 2006).

3.4. Oxygen Collision Complex $(O_2)_2$

The oxygen collision complex $(O_2)_2$, in contrast to the isolated oxygen molecule O_2, shows several prominent absorption bands in the spectral range from the near UV to visible to near infrared and therefore has to be considered in the DOAS trace gas fitting retrieval. At usual atmospheric temperatures these absorption features are due to collision induced dipole transitions, however, for very low temperatures rotational-vibrational transitions in a O_2-O_2 van der Waals molecule is a dominant process. An often-used brief description is O_4. The oxygen dimers absorption strength is proportional to the oxygen partial pressure and shows hardly any temperature dependence. (Camy-Peyret and Vigasin, 2003; Pfeilsticker et al., 1997)

4. Shipping Emissions

4.1. Emitted Species and Environmental Impacts

Shipping emissions account for a significant part of the emissions from the transportation sector (Eyring et al., 2005b). On a global scale the exhaust gases and particles have an influence on the composition of the atmosphere and climate, on a local scale, they influence the air quality and human health (Eyring et al., 2010b).

The most important emitted pollutants are carbon dioxide (CO_2), carbon monoxide (CO), nitrogen oxides (NO_x), sulfur dioxide (SO_2), black carbon (BC), volatile organic compounds (VOC) and particulate matter (PM) (Eyring et al., 2010a). During the tank ship loading process, also evaporation of hydrocarbons (HC) takes place (Eyring et al., 2005a). Table 4.1 shows the annual shipping emission and fuel consumption estimates for four different years.

Table 4.1.: Estimates of the annual shipping emissions and fuel consumption for today, the near past and the future

	1950[a]	1970[a]	2001	2050[d]
No. of ships ($> 100\,GT$)	30 800	52 400	89 000[a]	126 800–172 400
CO_2 [Tg C]	51	98	249[b]/ 222[c]	302–546
NO_x [Tg N]	1.6	3.3	6.87[b]/ 6.5[c]	1.7–20.9
SO_2 [Tg S]	1.4	2.7	6.49[b]/ 6.0[c]	1.8–13.0
PM_{10} [Tg]	0.39	0.74	1.64[b]/ 1.67[c]	1.45–3.92
HC [Tg]	0.9	1.74	0.769[b]/ 3.92[c]	3.65–6.53
Fuel consumption [Mt]	64.5	124	289[b]/ 280[c]	402–725

[a] All numbers for 1950 and 1970 taken from Eyring et al. (2005b)
[b] Corbett and Koehler (2003)
[c] Eyring et al. (2010b)
[d] All numbers for 2050 taken from Eyring et al. (2005a), number ranges represent different future scenarios

As can be seen from Table 4.1, the number of ships, fuel consumption as well as emissions increased considerably in the last decades. Shipping emissions in 2001 accounted for 2.7 % of the total anthropogenic CO_2 emissions, provided 15 % of all anthropogenic NO_x and 8 % of all anthropogenic SO_2 emissions. Ship engines which are working at high temperature and pressure lead to the high percentage of NO_x emissions, and also missing reduction technologies for NO_x play a role. The high fraction of SO_2 emissions is mainly due to the high sulfur content in fuels (on average 2.4 % to 2.7 %). (Eyring et al., 2010a)

In addition, ship traffic has increased massively in the last years. The capacity of the global merchant fleet has more than doubled since the year 2000 as can be seen from Figure 4.1. This means that also the fraction of shipping emissions on the total anthropogenic emissions is increasing.
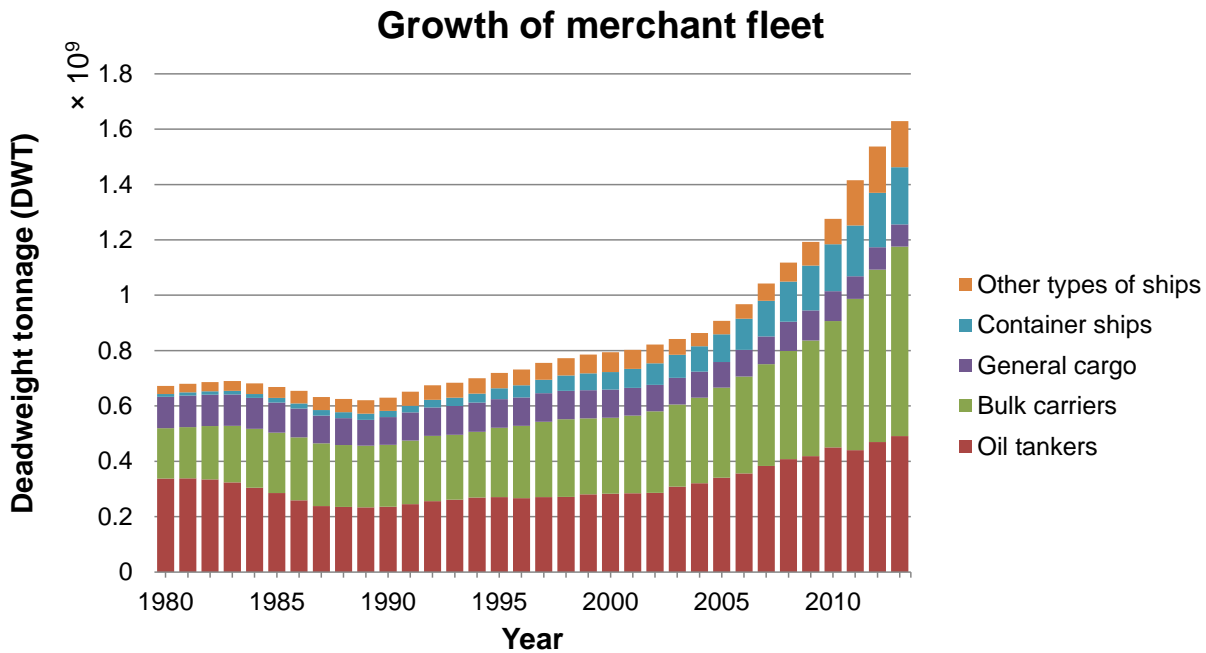
Figure 4.1.: Evolution of the capacity of the global merchant fleet in the time period from 1980 to 2013 [Numbers taken from `http://unctadstat.unctad.org` (09.05.2014)]

The global pathways of the ships can even be seen in the NO_2 measurements from various satellite instruments: from GOME (**G**lobal **O**zone **M**onitoring **E**xperiment) (Burrows et al., 1999) over the Indian Ocean (Beirle et al., 2004), from SCIAMACHY (**Sc**anning **I**maging **A**bsorption Spectro**m**eter for **A**tmospheric **Ch**artograph**y**) on board the ENVISAT satellite (Bovensmann et al., 1999) over the Indian Ocean and the Red Sea (Richter et al., 2004) and in even more detail from the successor GOME-2 on board MetOp-A (Callies et al., 2000), showing a lot more ship tracks (Richter et al., 2011), which is shown in Figure 4.2.
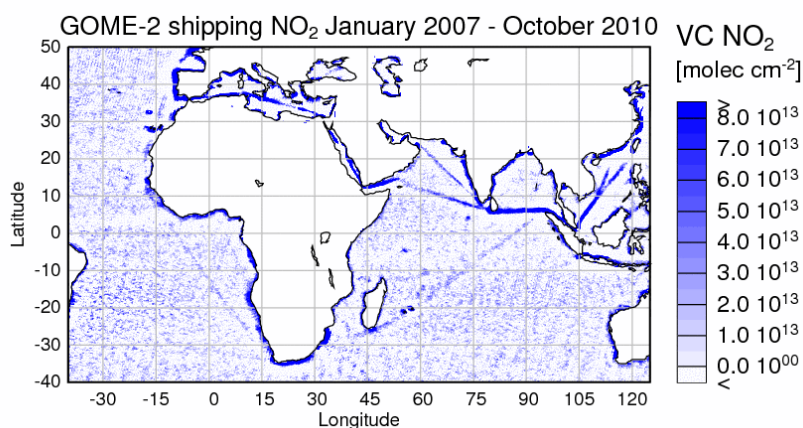
Figure 4.2.: Global ship tracks visible in long-term satellite measurements of NO_2 from the instrument GOME-2 onboard MetOp-A (Richter et al., 2011)

Eyring et al. (2005a) showed that the development of shipping emissions in the future does more depend on the technologies used than on the economic growth rates. They proposed that the use of efficient NO_x reduction technologies can lead to a substantially decrease in NO_x emissions compared to today,

despite a huge increase in the number of ships. If no better reduction technologies additional to today's will be installed, NO_x emissions from ships in the future will exceed today's road transport emissions. Further regulations of the sulfur content of the fuel will determine SO_2 emissions in the future. The CO_2 emissions from ships, in contrast, depend to a high extend on the total fuel consumption and therefore on the economic growth rate.

On a local scale, shipping emissions have an impact on human health due to emissions of particulate matter, sulfur and formation of tropospheric ozone in the boundary layer (Eyring et al., 2010a). On a global scale, emissions of exhaust gases and particles from ships lead to a change of climate and the composition of the atmosphere (Lawrence and Crutzen, 1999; Endresen et al., 2003).

Air pollution by particles can lead to various health hazards including heart attacks, asthma, premature mortality and hospital admissions (Corbett et al., 2007). Furthermore, Corbett et al. (2007) estimate that particulate matter emissions from ships account for about 60 000 deaths due to cardiopulmonary and lung cancer. A majority of those deaths occur in coastal regions of Europe as well as South and East Asia, regions where both high population densities and high shipping-related particle concentrations appear. Thereby, shipping emissions are responsible for 3 % to 8 % of the total worldwide deaths due to atmospheric particles (Eyring et al., 2010b).

NO_x, CO and unburned hydrocarbons are important precursors for the formation of tropospheric ozone. High concentrations of ground-level ozone can also lead to health issues and harm natural vegetation. It is radiatively active and can change the radiative budget, therefore effecting climate (Eyring et al., 2005a). Moreover, formation of tropospheric ozone leads to an increase of hydroxyl-radical (OH) concentrations, representing an increase of the oxidizing capacity of the marine boundary layer and the free troposphere. This can cause a significant decrease of the lifetime and abundance of methane (CH_4), an important greenhouse gas (Eyring et al., 2005a; Lawrence and Crutzen, 1999).

Emitted sulfur dioxide is oxidized by OH to sulphate aerosols (see Chapter 3.3). Sulfate particles influence climate directly by scattering and absorption of solar radiation and indirectly by changing the properties of clouds. Aerosols can form cloud condensation nuclei (CGN) leading to increasing cloud condensation and higher concentration of droplets. Such changes of cloud reflectivity and lifetime change also the Earth's albedo. (Lauer et al., 2007; Eyring et al., 2010b; Lawrence and Crutzen, 1999)

The influence of shipping emissions on climate change is rather complex and shows a contradictory behavior. The enhanced SO_2 emissions increase the formation of aerosol particles and clouds leading to a cooling effect. NO_x emissions play an important role in the formation of tropospheric ozone. Although this greenhouse gas contributes with a warming effect, NO_x also reduces the levels of the greenhouse gas methane (CH_4) by increasing the OH concentrations, which then leads to a cooling. (Fuglestvedt et al., 2009; Lawrence and Crutzen, 1999)

However, the climate impact of sulfate is on the order of decades, while the climate response of CO_2 is on the order of centuries. This means that despite the cooling related to SO_2 emissions, the warming due to the very long lived CO_2 will dominate in the future, especially when further reductions of SO_2 and NO_x emissions take place. (Fuglestvedt et al., 2009; Eyring et al., 2010b)

Emissions of NO_x and SO_2 also lead to an acidification of 3–10 % in certain coastal regions, causing more acid rain formation (Endresen et al., 2003).

While around 70 % of shipping emissions occur within 400 km of land, they can contribute substantially to air pollution in coastal areas (Eyring et al., 2010b). Ship emissions provide a dominant source of air pollution in harbour cities (Eyring et al., 2010a). In addition to that, transport of ozone and aerosol precursors (NO_x and SO_2 as well as particles) over several hundreds of kilometers also affect air quality and human health further inland, far away from their emission point (Eyring et al., 2010a,b).

4.2. MARPOL Regulations

Shipping emission is a transnational problem, because it is very difficult to assign the emissions to specific countries. This problem of undecided responsibility is a reason why shipping emissions are not regulated by the Kyoto protocol. (Fuglestvedt et al., 2009; Eyring et al., 2010b)

International ship traffic is subject to regulations of the International Maritime Organization (IMO). Shipping emissions are regulated by the *International Convention for the Prevention of Pollution from Ships* (MARPOL 73/78 Annex VI). This Annex was added in 1997 and entered into force in 2005. A revision with more stringent emission limits was adopted in 2008 and went into force 2010.

MARPOL Annex VI aims for the minimization of exhaust gas emissions from ships (SO_2, NO_x, VOCs, ozone depleting substances (ODS)). Also the contribution of shipping emissions to local and global environmental problems as well as air pollution should be minimized. It sets limits on sulfur content in heavy oil fuels (see Table 4.2) globally as well as establishes local *Sulfur Emission Control Areas* (SECA) with more stringent restrictions and controls .

Table 4.2.: Marpol Annex VI sulfur content limitations

Date	Sulfur Content Limit in Fuel [% m/m]	
	inside SECA	global (outside SECA)
2000	1.5	4.5
2000 (July)	1.0	
2012		3.5
2015	0.1	
2020 or 2025[a]		0.5

[a] The decision on the actual date will be published in 2018, depending on the availability of appropriate fuel oils.

The Baltic Sea was the first SECA, later the North Sea as well as two SECAs in North America followed. Later, the SECAs were changed into general *Emission Control Areas* (ECA), which can be seen in Figure 4.3. In the North Sea and Baltic Sea only sulfur content is regulated, in the North American and United States Caribbean Sea area also NO_x and PM are limited.

Annex VI also establishes limits on the emission of NO_x for newly built diesel engines. Table 4.2 states the sulfur content limits; Figure 4.4 illustrates the evolution of the sulfur content limits and Figure 4.5 the engine power depending NO_x limiting curve.

If the ships comply with the regulations and if this reduces air pollution in the marine environment is one of the aims of the MeSmarT project (see Chapter 8).

Figure 4.3.: Map of the established Emission Controlled Areas (ECA) as well as possible future ECAs [Source: `http://blogs.dnvgl.com/lng/2011/02/lng-for-greener-shipping-in-north-america` (09.05.2014)]
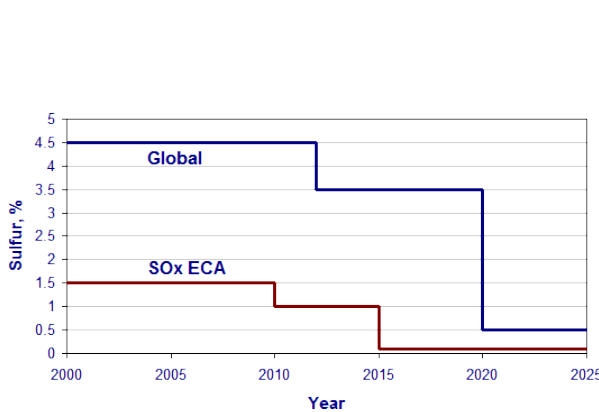
Figure 4.4.: Evolution of MARPOL Annex VI sulfur content regulations inside Sulfur Emission Control Areas (SECA) and globally (outside SECA) [Source: `http://www.dieselnet.com/standards/inter/imo.php` (09.05.2014)]
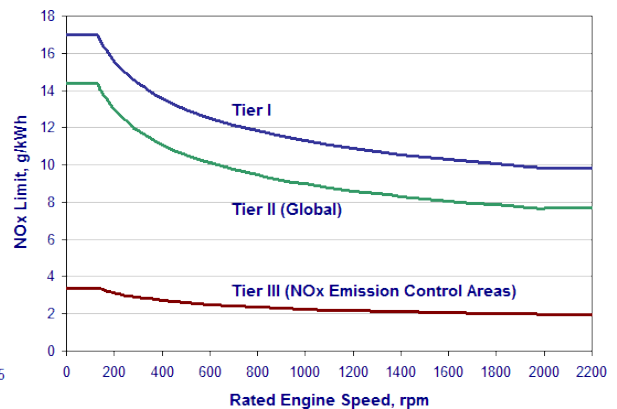
Figure 4.5.: MARPOL Annex VI NO_x emission limits as a function of engine power for engines built after 2000 (Tier I), 2011 (Tier II) and 2016 (Tier III) [Source: `http://www.dieselnet.com/standards/inter/imo.php` (09.05.2014)]

5. Radiation Physics

5.1. Absorption and Emission of Light

The main interaction processes of light with matter are absorption and emission. When a photon of the appropriate frequency ν is emitted or absorbed by an atom, the energy state of the atom changes according to $\Delta E = E_{\text{initial}} - E_{\text{final}} = h \cdot \nu$.
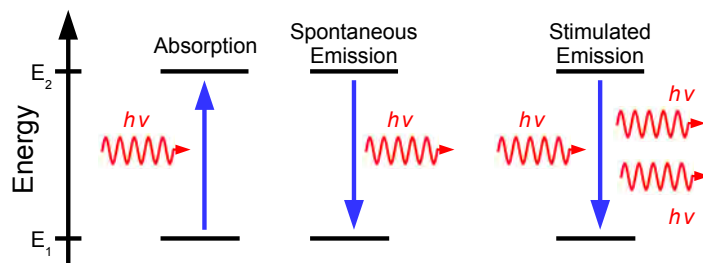
Figure 5.1.: Absorption and emission of light

The transitions between the electronic energy states, characterized by the quantum numbers (n, l, m_l, m_s), also have to obey quantum mechanical selection rules, which describe whether a transition is allowed and which intensity the according spectral line has. A prominent example for a line spectrum is the Balmer series of the hydrogen atom or Fraunhofer lines in the solar spectrum (see Figure 6.1). The lines in such an absorption or emission spectrum are not entirely monochromatic, but show a finite width. This is true, even if the measurement device has a perfect resolution. This line broadening is caused by various effects:

- The natural line broadening is a result of the life time of the excited states. A rapidly decaying state creates a very broad line according to Heisenberg's uncertainty principle: $\Delta E \cdot \Delta t \geq \hbar/2$ with $\hbar = h/2\pi$. The resulting spectral line shows a Lorentzian profile.

- Doppler broadening is due to the thermal velocity distribution in a gas. The Doppler effect creates a positive or negative wavelength shift, depending on the moving direction of the gas atom relative to the observing instrument. The width of the broadening is proportional to the temperature as the Doppler shift increases with temperature, but decreases with increasing atom mass (inertia). It results in a Gaussian line shape and is about two orders of magnitude stronger than the natural line broadening in the visible spectral range.

- Pressure broadening is caused by elastic or inelastic collisions between gas atoms, which change the atomic energies and the phase of the emitted light. It is proportional to the pressure in the gas and also stronger than the natural line broadening. The resulting line shape has as also a Lorentzian profile.

For typical conditions, Doppler broadening and pressure broadening are the relevant processes that have to be considered. The observed line shape is a mixture of a Gaussian and a Lorentzian profile. (Demtröder, 2010; Haken and Wolf, 2004; Lipson et al., 1997)

Depending on the energy of the absorbed photon, several processes are possible. Low energetic photons are simply absorbed if their frequency fits to the energy difference ($h \cdot \nu \overset{!}{=} \Delta E$), increasing the electronic energy. Higher energetic photons can be absorbed causing an electron to be removed from the atom, which is called the photo-electrical effect. If the energy is increased further the Compton effect occurs, where additional to the Compton-electron also a new photon is created. For very high photonic energies, pair production of an electron and a positron can happen. (Demtröder, 2010)

In the case of emission, one distinguishes two processes: spontaneous emission and induced or stimulated emission (see sketch in Figure 5.1). The spontaneous emission is the decay of an energetically excited electronic state. As described above, the line width of the emitted photon depends on the decay time. Stimulated emission can be used to create a self-enhancing decay chain, working like a chain reaction. The produced light is monochromatic and very intense and is used as laser (**l**ight **a**mplification by **s**timulated **e**mission of **r**adiation).

While for transitions of outer, weak-bonded electrons the produced light is in the spectral range from UV to infrared, transitions of the strong-bonded electrons near to the atomic core cause the emission of high energetic x-ray radiation. (Demtröder, 2007; Haken and Wolf, 2004; Demtröder, 2010)

In addition to line spectra, there are also continuous spectra, which are emitted by black bodies like a glowing solid state body or a high-density gas. Einstein stated in 1917, that the dynamic of the three important interaction processes – absorption, spontaneous and induced emission – can be described using rate equations with the so-called Einstein-coefficients as proportionality constants. He also showed that by incorporating the Boltzmann distribution $\left(\frac{N_2}{N_1} = e^{-\frac{E_2 - E_1}{k_\mathrm{B} \cdot T}} \right)$ for the energy level occupation numbers N_i and considering Rayleigh-Jeans law $\left(u(\nu) = \frac{8 \cdot \pi \cdot \nu^2}{c^3} \cdot k_\mathrm{B} T \right)$ as a limiting case one can deduce Planck's law:

$$u(\nu) \cdot \mathrm{d}\nu = \frac{8 \cdot \pi \cdot h}{c^3} \cdot \frac{\nu^3}{e^{\frac{h \cdot \nu}{k_\mathrm{B} \cdot T}} - 1} \cdot \mathrm{d}\nu \tag{5.1}$$

with the spectral radiance u, Planck constant h, Boltzmann constant k_B, speed of light c and temperature T. Planck's law describes the radiation spectrum emitted by a black body at a specific temperature. In Figure 6.1 it can be seen that the solar spectrum is nearly a planck curve. Integrating equation 5.1 over the half-sphere and all frequencies delivers the Stefan-Boltzmann law, which gives us the total power P of the radiation emitted by the black body with surface A:

$$P = \sigma \cdot A \cdot T^4 \tag{5.2}$$

Differentiation of Planck's law (Equation 5.1) with respect to frequency and numerical methods deliver Wien's displacement law for the frequency (or wavelength) maximum:

$$\frac{\nu_\mathrm{max}}{T} = const. \approx 5.88 \times 10^{10}\,\mathrm{Hz/K}, \qquad \lambda_\mathrm{max} \cdot T = const. \approx 2898\,\mathrm{\mu m\,K} \tag{5.3}$$

(Demtröder, 2010; Haken and Wolf, 2004)

5.2. Molecular Spectra

In addition to electronic excitations observed in atoms, molecules show also vibrational and rotational excitations. The total molecular energy E is approximately the sum of the electronic energy E_{el}, the vibrational energy E_{vib} and the rotational energy E_{rot}. The energies of the corresponding states and transitions differ significantly: $h \cdot \nu_{rot} \ll h \cdot \nu_{vib} \ll h \cdot \nu_{el}$. Table 5.1 shows the approximate energies, spectral ranges and typical units for the three transition types.

Table 5.1.: Overview of the three molecular transitions types with the corresponding energies, spectral ranges and typical quantities as well as units used in spectroscopy

Transition	Energy [eV]	Spectral range	Typical quantity and unit
rotational	10–1000 µeV	microwave	frequency [GHz]
vibrational	1–100 meV	infrared	wave number [cm^{-1}]
electronic	1–10 eV	visible, UV	wave length [nm]

A molecule consisting of N atoms has $3N$ degrees of freedom, which split up into translation, rotation and vibration: $3 \cdot N = f_{transl} + f_{rot} + f_{vib}$. Atoms as well as molecules can move in all three directions of space, meaning $f_{transl} = 3$. Molecules also show rotational and vibrational movement, but only for molecules with a permanent electric dipole moment the according transition lines can be observed. Non-linear molecules can rotate around three orthogonal axes ($f_{rot,non-linear} = 3$), whereas for linear molecules rotation around the connecting bond can be neglected because the corresponding moment of inertia is very small and also the electric dipole moment does not change ($f_{rot,linear} = 2$), which is a prerequisite for the interaction with light. There are $3N - 6$ (for non-linear molecules) or $3N - 5$ (for linear molecules) degrees of freedom left for the various vibration modes. (Haken and Wolf, 2006)

5.2.1. Rotational Spectra

Pure rotational spectra arise from rotational transitions, where only the quantum number of rotation J changes, but vibrational and electronic states remain the same. The resulting spectra consist of closely spaced, nearly equidistant lines with a characteristic intensity distribution (maximum approximately in the middle). Assuming a two atomic molecule with an unflexible bond (rigid rotor model) delivers for the rotational energy levels:

$$E_{rot} = \frac{\hbar^2}{2\Theta} \cdot J \cdot (J+1) = hc \cdot B \cdot J \cdot (J+1) \qquad \text{with} \qquad B = \frac{h}{8 \cdot \pi^2 \cdot \Theta \cdot c} \qquad (5.4)$$

Since the rotational constant B is proportional to $1/\Theta$, the rotational spectra of heavier molecules have less energy (longer wavelength). This model can be extended to the non-rigid rotor, showing that the distance between the lines decreases slightly with increasing J and therefore increasing distance between the atoms. The selection rule for transitions is $\Delta J = \pm 1$ for $J = 0, 1, 2, 3....$ The intensity of the spectral lines depends on two factors: the degree of degeneracy $(2J + 1)$ which increases with increasing J and the thermal occupation of the energy levels (Boltzmann distribution), which decreases for increasing J. This means, that there has to be a population maximum somewhere in the middle. (Haken and Wolf, 2006)

5.2.2. Vibrational spectra

Observing vibrational spectra in the IR at low resolution shows a strong line at frequency ν and several overtones at 2ν, 3ν etc. Looking at these lines at higher resolution reveals that every line is a band consisting of many nearly equidistant rotational transition lines. Such a rotational-vibrational spectrum is created by transitions between the rotational energy levels of different vibrational levels, which means that both J as well as the vibrational quantum number ν change. The assumption that the bond in a two atomic molecule behaves like a harmonic oscillator potential (parabolic) delivers equidistant energy levels, but does not explain the overtones:

$$E_{\mathrm{vib}} = \hbar\omega \left(\nu + \frac{1}{2} \right) \tag{5.5}$$

A better approximation is the anharmonic oscillator with the empirically determined Morse potential, which explains the occurrence of the overtones and shows that the distance between the energy levels decreases towards the dissociation continuum. Vibrational and rotational transitions are coupled and vibrations are much faster than rotations (several thousand times). The rotational selection rule $\Delta J = \pm 1$ leads to the formation of two branches, the P-branch with shorter wavelengths and diverging lines and the R-branch with longer wavelengths and converging lines. The pure vibrational transition $\Delta J = 0$ (Q-branch) is often forbidden. The various vibration modes, e.g. symmetrical and antisymmetrical stretching or deformation, are infrared active only if the dipole moment changes. (Haken and Wolf, 2006)

5.2.3. Electronic Spectra

If in addition to rotational and vibrational transitions also the electronic state changes, one obtains an electronic spectrum, which is called a band system. The probability for such vibronic transitions and therefore the intensity of the spectral lines is governed by the Franck-Condon principle: The Born-Oppenheimer approximation states that the movement of the electron is very fast in comparison to the core's, which means that transitions in the energy level diagram occur vertically (see Figure 5.2). The probability for a transition is then determined by evaluating the vibrational overlap integral, also called the Franck-Condon factor. It can be deduced from the transition dipole moment (transition matrix element) by incorporating the Born-Oppenheimer approximation mentioned above. (Haken and Wolf, 2006)
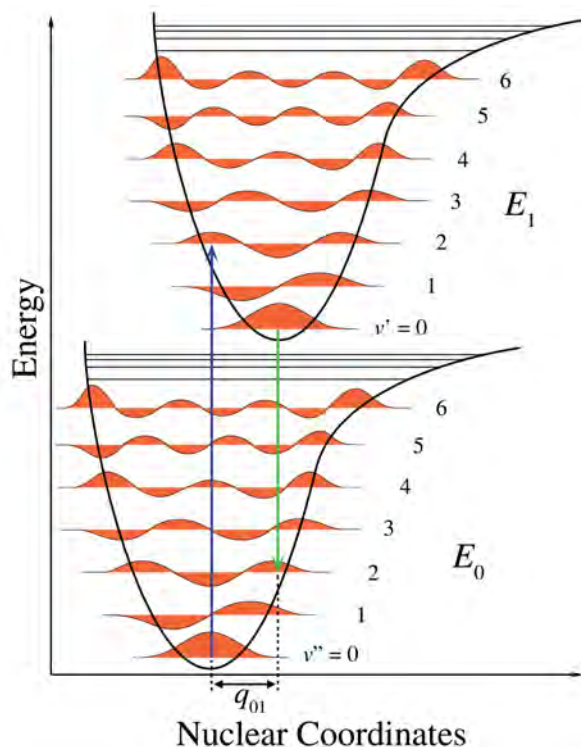
Figure 5.2.: Transitions between two electronic states E_0 and E_1 with their vibrational energy levels $\nu = 0, 1, 2, ...$ according to the Franck-Condon principle [Image source: `http://upload.wikimedia.org/wikipedia/commons/0/0e/Franck-Condon-diagram.png` (14.05.2014)

5.3. Scattering

The oscillating electromagnetic field of a light beam hitting a dielectric (uncharged) particle in the atmosphere causes a periodical polarization of the particle by displacing the centers of charge and forcing an oscillation. After a certain time the excited particle emits electromagnetic radiation which can then be detected as scattered light. During this process the energy of the particle is either conserved (elastic scattering) or increased or rather decreased (inelastic scattering). Depending on the ratio between light wavelength and particle size one can distinguish several types of light scattering which are described by different theories (Roedel and Wagner, 2011). A classification is possible by defining the so-called particle size parameter, which is a dimensionless quantity:

$$\alpha = \frac{2 \cdot \pi \cdot r}{\lambda} \tag{5.6}$$

with the radius of the particle r (assumed to be spherical) and the light wavelength λ. Scattering by particles which are small compared to the light wavelength ($\alpha << 1$) like air molecules and small aerosol particles is called Rayleigh scattering. Particles which are nearly equal in size to the light wavelength ($\alpha \approx 1$) like aerosol particles or water droplets in clouds cause Mie scattering. For very large particles ($\alpha >> 1$) the scattering process can be described by simple geometric optic. (Roedel and Wagner, 2011; Seinfeld and Pandis, 2006). Rayleigh scattering and geometric optic are special borderline cases of the more general Mie theory (Hecht, 2005).

Rayleigh scattering has a strong wavelength dependence of nearly $\propto \lambda^{-4}$. This explains the blue color of the cloudless sky because shorter wavelength radiation (blue light) is scattered stronger away from

the beam direction than longer wavelength radiation (red light). The scattered light intensity for non-polarized light is proportional to $1 + \cos^2 \vartheta$ with the scattering angle ϑ (angle between incident and scattered light beam). This weak angle dependence means that the scattered light is approximately equally distributed in all directions. Rayleigh scattering produces non-polarized light in forward and backward direction and maximum linear polarized light orthogonal to the incident light beam which can be seen by looking at the sky through a polarization filter.(Roedel and Wagner, 2011)

The scattering cross-section of Mie scattering is proportional to λ^{-a} with the Angstrom exponent $-1 < a \leq 4$ with typical values in the range between 0.5 and 2.5 (Roedel and Wagner, 2011; Platt and Stutz, 2008). On the contrary, Mie scattering shows a strong angular dependence with a strongly pronounced maximum in the incident direction and several additional maxima and minima. The shape of the curve (scattering cross-section vs. scattering angle) and the number of maxima also depends on the particle size parameter α. (Roedel and Wagner, 2011). Additional to elastic Rayleigh scattering also 2–4 % of the photons undergo inelastic scattering by air molecules. This is mainly due to (rotational) Raman scattering. The change of the energy of the photons due to the change of the kinetic energy of the particle results in a wavelength shift. This shift can be up to 2 nm (Roedel and Wagner, 2011).

5.4. The Ring Effect

When light passes through the atmosphere inelastic rotational Raman scattering can cause a wavelength shift in the range of a few nanometers. If this wavelength shift is large enough, it can change the shape of absorption lines. This process is called the Ring effect and was first observed for the Fraunhofer lines by Grainger and Ring (1962). Since the wavelength of the scattered light is shifted (e.g. by $\Delta\lambda$), the loss of intensity at a certain wavelength λ is proportional to the local intensity $I(\lambda)$. The gain of intensity at wavelength λ is proportional to the intensity at the adjacent wavelengths $\lambda \pm \Delta$. For absorption lines, this results in a filling-in, like it is observed for deep Fraunhofer lines. (Burrows et al., 2011; Richter, 1997)

Because the Ring effect can be one order of magnitude larger than trace gas absorption, it has to be included in the trace gas retrieval (see Chapter 6.3), which is often accounted for by including a pseudo-absorber cross-section (Solomon et al., 1987), often called the Ring spectrum, which can be computed with radiative transfer models. The influence from vibrational Raman scattering in the atmosphere, on the contrary, is small and can be neglected. (Burrows et al., 2011; Platt and Stutz, 2008)

6. Differential Optical Absorption Spectroscopy (DOAS)

This chapter describes the differential optical absorption spectroscopy (DOAS) technique as a measurement method for atmospheric trace gases.

6.1. Optical Spectroscopy

Optical spectroscopy is one of the most important physical measurement methods for the investigation of atoms and molecules. It is based on spectral decomposition of light that has interacted with matter and the analysis of the obtained spectra. For optical spectroscopy, various spectral ranges can be used, including gamma, x-ray, ultraviolet (UV), visible, infrared, microwaves, radar and radio.

Optical spectroscopy evaluates either the light which is directly emitted by the inspected sample (emission spectroscopy), or the light which has passed through an absorbing sample located in the light path (absorption spectroscopy).

Optical spectra can be distinguished into continuous spectra, line spectra and band spectra. Continuous spectra are emitted by glowing solid state bodies or high-density gases, which are nearly black body radiators, e.g. the sun, which can be seen in Figure 6.1. Line spectra, often grouped in characteristic series, can be assigned to atoms. A prominent example are Fraunhofer lines in the spectrum of the sun, which are produced by atomic absorption in the sun's atmosphere. Band spectra contain groups of multiple lines very close to each other and can be assigned to molecules. Many band structures can only be separated by using a very high spectral resolution. In addition to electronic excitations observed in atoms, molecules show also vibrational and rotational excitations (see Chapter 5.2). (Haken and Wolf, 2004)

Differential optical absorption spectroscopy (DOAS) is a measurement technique for atmospheric trace gases in which absorption spectra in the visible and UV spectral range are investigated. The characteristic absorption spectra are assigned to the different trace gases. The strength of the particular absorption is a measure for the number of gas molecules along the light path. *Differential* means that only the narrow-band vibrational structures of the absorption spectra are considered. This is done by splitting up the wavelength dependent absorption cross-section into both a slowly and rapidly *(differential)* varying part. (Richter, 1997)
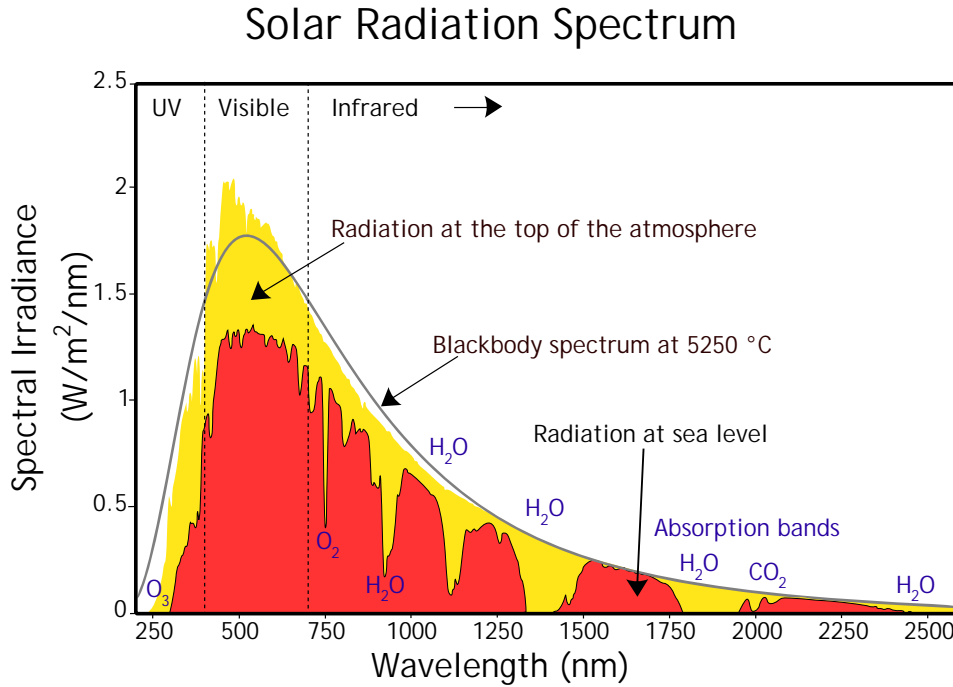
Solar Radiation Spectrum

Figure 6.1.: Schematic plot of the terrestrial and extraterrestrial solar irradiance as a function of the wavelength for the spectral range of 250 nm-2500 nm covering a part of the UV, the visible and infrared. Also shown is the radiation spectrum of an ideal black body at a temperature of 5523 K which coincides well with the extraterrestrial solar spectrum. This indicates that the surface temperature of the sun is approximately around this value. (Data based on: American Society for Testing and Materials (ASTM) Terrestrial Reference Spectra; image source: `http://commons.wikimedia.org/wiki/File:Solar_spectrum_en.svg`, 10.03.2014)

6.2. Lambert-Beer Law

The basic principle of optical absorption spectroscopy is that the intensity of light decreases while passing through an absorbing medium. The differential decrease of the light intensity $\mathrm{d}I$ along the infinitesimal distance $\mathrm{d}s$ is proportional to the number density $n = {}^{N}/{}_{V}$ (in $^{\mathrm{particles}}/_{\mathrm{volume}}$) and the absorption cross-section σ (dimension of an area) of the absorbing medium and to the intensity I itself:

$$\frac{\mathrm{d}I}{\mathrm{d}s} = -n \cdot \sigma \cdot I \tag{6.1}$$

The product of number density and absorption cross-section has the dimension $^{1}/_{\mathrm{length}}$ and is often called the absorption coefficient $K_a := n \cdot \sigma$. Integration along the light path assuming that N and σ do not depend on s (special case) and subsequent exponentiation gives the well-known Lambert-Beer law (also known as Beer–Lambert–Bouguer law):

$$I(s) = I_0 \cdot e^{-n \cdot \sigma \cdot s} = I_0 \cdot e^{-K_a \cdot s} = I_0 \cdot e^{-\tau} \tag{6.2}$$

with $I_0 \equiv I(s=0)$, the intensity of the incident light, the absorption coefficient $K_a = n \cdot \sigma$ and the optical depth or optical thickness $\tau = K_a \cdot s = n \cdot \sigma \cdot s = \ln \frac{I_0}{I}$. (Roedel and Wagner, 2011; Burrows et al., 2011; Haken and Wolf, 2004)

This formula describes only a special case for an isotropic medium and is only valid for monochromatic light because both the intensity and the absorption cross-section depend on the wavelength. Furthermore the absorption cross-section depends also on temperature and pressure of the absorbing medium. For the general case of an anisotropic medium n and σ are not constant along the lightpath and we have to replace equation (6.2) with:

$$I(s, \lambda, T, p) = I_0(\lambda) \cdot \exp\left\{ -\int_0^s n(s') \cdot \sigma(\lambda, T(s'), p(s')) \cdot \mathrm{d}s' \right\} \tag{6.3}$$

(Roedel and Wagner, 2011; Haken and Wolf, 2004)
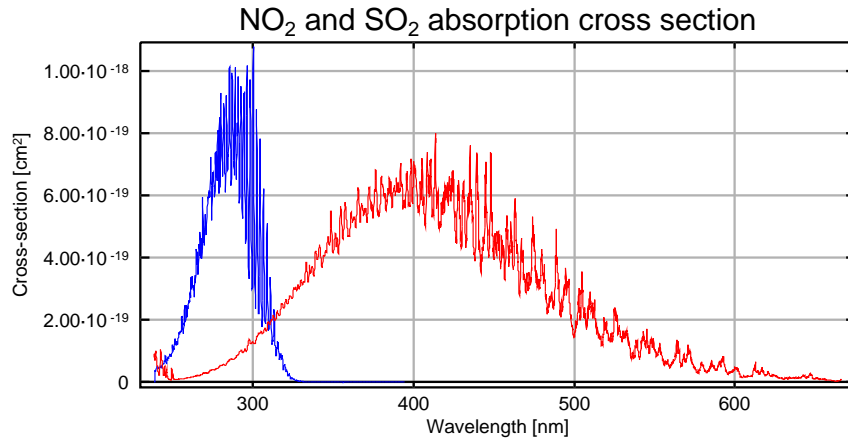
6.3. DOAS-Method

Figure 6.2.: Absorption cross section of NO_2 (298 K, Vandaele et al. 1996) in red and SO_2 (293 K, Bogumil et al. 2003) in blue

The DOAS-method is based on Lambert-Beer's law (6.3). However, for the application of optical absorption spectroscopy in the atmosphere this simple model has to be extended. As described in chapter 2.1, the atmosphere contains a large number of different trace gases, which means that multiple absorbers i with different number densities n_i and absorption cross-sections $\sigma_i(\lambda)$ (see Figure 6.2 for NO_2 and SO_2) have to be included. Both n_i and σ_i depend on the altitude in the atmosphere and therefore on the light path s.

In addition to absorption also light scattering on air molecules and aerosol particles has to be taken into account as another important extinction process. The most important scattering processes are elastic scattering by small particles like air molecules (Rayleigh scattering), by large particles like aerosols or water droplets (Mie scattering) and inelastic scattering by air molecules (Raman scattering) which is responsible for the Ring effect (see Chapter 5.4). The light extinction cause by these processes can be described by the Lambert-Beer law using their scattering cross-section as a pseudo cross-section. Applying the additions to equation (6.3) we obtain the measured spectrum $I(\lambda)$ at the location of the detector:

$$I(\lambda) = I_0(\lambda) \cdot \exp\left\{ -\int \left[\sum_{i=1}^{N} n_i(s) \cdot \sigma_i(\lambda, s) + n_j(s) \cdot \sigma_j(\lambda, s) \Big|_{j=\mathrm{Ray,Mie,Ring}} \right] \mathrm{d}s \right\} \tag{6.4}$$

To simplify this equation we assume that the absorption cross-sections do not depend on altitude and light path s. Defining the so-called slant column density of a trace gas as the integrated number density along the light path $\text{SCD}_i = \int n_i(s)\mathrm{d}s$ and treating the Ring effect as an additional absorber (Solomon et al., 1987) gives:

$$I(\lambda) = I_0(\lambda) \cdot \exp\left\{-\left[\sum_{i=1}^{N+1} \text{SCD}_i \cdot \sigma_i(\lambda) + \text{SCD}_{\text{Ray}} \cdot \sigma_{\text{Ray}}(\lambda) + \text{SCD}_{\text{Mie}} \cdot \sigma_{\text{Mie}}(\lambda)\right]\right\} \tag{6.5}$$

The quantity that should be derived from this formula is the SCD. To obtain the SCD of a specific trace gas it would be necessary to obtain all information about the other trace gases and processes. Unlike in the case of laboratory measurements, the separation of the different contributions in the free atmosphere is not possible. Another problem is strong and broadband fluctuations of the light intensity caused by clouds. (Platt and Stutz, 2008; Richter, 1997)

One way to overcome this problem is a separation of the absorption cross-section $\sigma_i(\lambda)$ into a slowly varying function $\sigma_{i,0}(\lambda)$ accounting for the broadband structures and a rapidly varying part $\sigma_i'(\lambda)$, the *differential* cross-section, considering the narrow-band structures. This method is called *differential optical absorption spectroscopy* (DOAS) (Platt and Stutz, 2008). The separation is be done by fitting a low-order polynomial to $\sigma_i(\lambda)$ and subsequent subtraction (Richter, 1997). The differential cross-sections $\sigma_i'(\lambda)$ are taken from laboratory measurements or literature (Platt and Stutz, 2008). As described in section 5.3, the scattering cross-section for Rayleigh scattering is nearly proportional to λ^{-4} and for Mie scattering proportional to λ^{-a} with an Angstrom exponent of $-1 < a \leq 4$ (mostly $0 < a < 2$). Therefore, both scattering processes and the broadband part of the absorption cross-section $\sigma_{i,0}(\lambda)$ can be approximated by a low-order polynomial $\sum_p c_p \cdot \lambda^p$.

$$I(\lambda) = I_0(\lambda) \cdot \exp\left\{-\left[\sum_{i=1}^{N+1} \text{SCD}_i \cdot \sigma_i'(\lambda) + \sum_p c_p \cdot \lambda^p\right]\right\} \tag{6.6}$$

Rearranging and taking the natural logarithm gives the so-called **DOAS equation**:

$$\ln\left(\frac{I(\lambda)}{I_0(\lambda)}\right) = -\sum_{i=1}^{N+1} \text{SCD}_i \cdot \sigma_i'(\lambda) - \sum_p c_p \cdot \lambda^p + \text{RESIDUAL}(\lambda) \tag{6.7}$$

The unknown variables SCD_i and the coefficients c_p of the polynomial are calculated by using a linear least-squares fit (Richter, 1997). For this, a wavelength window including strong and distinct absorption structures and avoiding disturbing interferences between different trace gas cross-sections has to be selected. Such a retrieval study has been done for the trace gas sulfur dioxide (SO_2) within the work for this thesis (see Chapter 10).

6.4. Air Mass Factors and Vertical Columns

The slant column densities retrieved by the DOAS fit are the total number densities of the trace gases along the light path. To obtain the total number density above the instrument, these slant columns have to be converted into vertical column densities using the so-called air-mass factor (AMF). The AMF is

defined as the ratio of the slant column density to the vertical column density (Richter, 1997):

$$\text{AMF}_i = \frac{\text{SCD}_i}{\text{VCD}_i} \tag{6.8}$$

The air-mass factors can be obtained by using radiative transfer models or approximated by using a simple geometrical estimation (see Section 6.7).

6.5. DOAS Measurement Setups

The DOAS method can be applied to a large number of different measurement geometries. Different arrangements of the light path are possible as well as different measurement modes using various light sources. One can distinguish between active DOAS, which uses artificial light sources like lasers or lamps and passive DOAS, which relies on natural light sources like the sun, moon or stars. Active DOAS techniques are for example the long-path DOAS (Perner et al., 1976), which was the first application of the DOAS method, the tomographic DOAS and the folded-path DOAS. Passive DOAS techniques often use the sun as a light source and differ in using either direct sunlight (ground-based, balloon measurements, occultation measurements from satellites) or scattered (ground-based zenith-sky DOAS (e.g. Noxon, 1975; Solomon et al., 1987) and Multi-Axis-DOAS (Hönninger et al., 2004; Wittrock et al., 2004)) or backscattered sunlight (airborne DOAS (e.g. Schönhardt et al., 2014) and satellite-borne DOAS (e.g. Burrows et al., 1999; Bovensmann et al., 1999; Burrows et al., 1995) in limb/nadir geometry). (Platt and Stutz, 2008)

The DOAS measurements for this thesis have been taken using ground-based Multi-Axis-DOAS (MAX-DOAS) and zenith-sky measurements. Also some measurements taken from airborne imaging DOAS (iDOAS) and from satellite DOAS are shown.

6.6. Measurement Geometry

The distance covered by the photons between the sun and the instrument and therefore the actual light path in the atmosphere and the retrieved slant column density (SCD) depends on the solar zenith angle (SZA). The SZA is the angle between the line of sight from the instrument to the sun and the imaginary line to the zenith perpendicular to the Earth's surface. It obviously depends on the measurement location, the date and time. In the following, this dependency is explained for zenith-sky measurements. The measurement geometry for off-axis or Multi-Axis-DOAS (MAX-DOAS) measurements, where smaller elevation angles closer to the horizon are used will be discussed later.

If we assume a cloudless sky and that the light is scattered only once (in the zenith), the photons pass through a long *slant* path in the atmosphere before being scattered vertically downward towards the instrument. As can be seen from Figure 6.3, the distance covered in the stratospheric absorber layer increases with increasing SZA. This implies, that the measurement sensitivity for stratospheric absorbers is higher for large SZAs (low sun elevation). (Richter, 1997)

It is impossible to know the actual height in which the photons measured at the ground had been scattered because there are numerous possible light paths. But it is possible to consider the most likely scattering
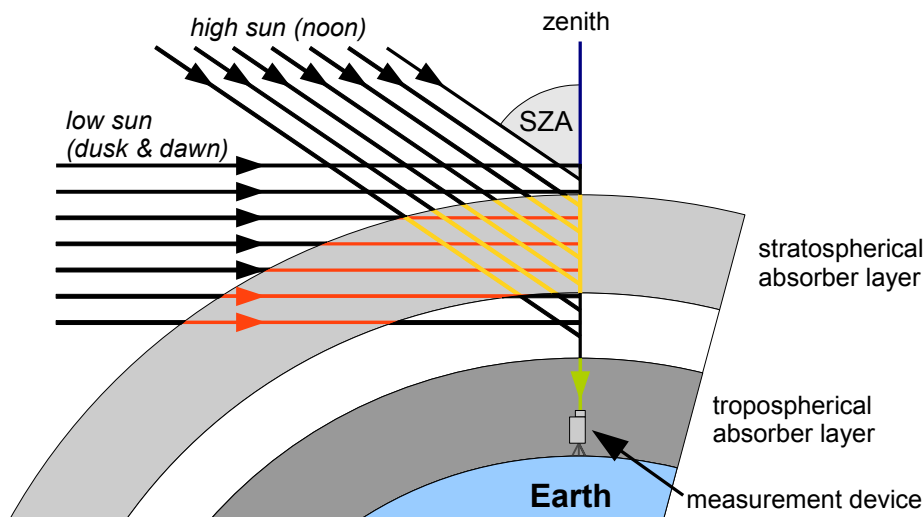
Figure 6.3.: Schematic plot of the measurement geometry for zenith-sky DOAS measurements for both high and low solar zenith angle (SZA) conditions

altitude. On the one hand, the number of scattered photons should be higher for higher altitudes, because the light is more intensive there.

On the other hand, we also know that the density of the air and therefore the scattering possibility decreases nearly exponentially with height (see chapter 2.2). This opposite trends suggest that a most likely scattering altitude exists and that this altitude should increase with increasing SZA. The slant column density retrieved from the measurement therefore represents a mean number density averaged over all possible light paths. (Richter, 1997)

For zenith-sky measurements the tropospheric light path barely depends on the SZA. For off-axis or MAX-DOAS measurements, where the telescope can point into various elevation and azimuth angles, the determination of the actual light path in the troposphere is more complicated. This is due to scattering by aerosol particles and cloud droplets which can influence the light path length. Also multiple scattering is possible, most likely in clouds. Moreover, photons which have been scattered at the ground can get scattered back into the light path. (Richter, 1997)

The measurement geometry for off-axis or MAX-DOAS measurements is sketched in Figure 6.4. As can be seen in this sketch, smaller elevation angles result in a longer light path in the lower troposphere but the light path in the upper atmosphere does almost not change. This results in an enhanced sensitivity for tropospheric trace gases when applying a low elevation angle. If the scattering point is located above the boundary layer, the light path through the boundary layer can be approximated geometrically if the absorber is located in the BL. If it lies inside the layer, this is much more difficult. A high aerosol concentration in the lower troposphere increases the scattering possibility and shifts the most probable scattering point towards the instrument shortening the light path. By taking measurements at multiple, slightly ascending elevation angles it is possible to calculate a vertical trace gas profile using radiative transfer models in combination with optimal estimation techniques . (Wittrock, 2006; Peters, 2013)

Figure (6.4) also shows that by taking a zenith spectrum close in time to the measured spectrum as the reference spectrum I_0 it is possible to remove the stratospheric part of the light path. This approach, which has been used for the measurements described in this thesis, also minimizes possible instrumental
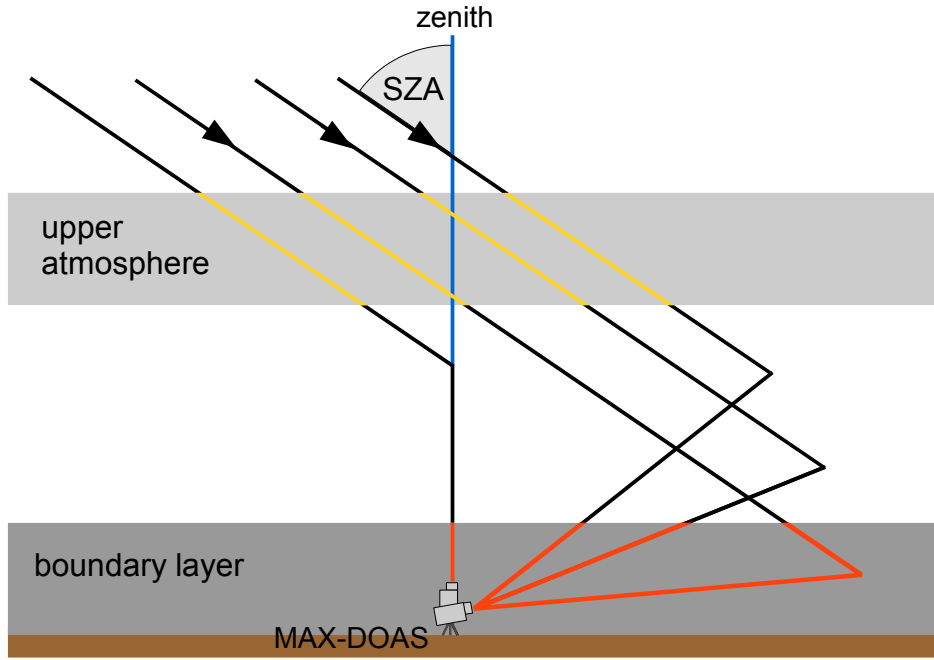
Figure 6.4.: Schematic plot of the measurement geometry for MAX-DOAS measurements in the planetary boundary layer

artifacts. Another possibility is the use of a zenith spectrum taken at noon (lowest SZA) when the atmospheric light path and therefore the atmospheric trace gas absorption is minimal.

The retrieved slant column density for ground-based MAX-DOAS measurements is not an absolute, but a differential slant column density which for simplicity is often only called slant column density (or slant column) (Peters, 2013):

$$DSCD_{\text{off-axis}} = SCD_{\text{off-axis}} - SCD_{\text{ref}} \qquad (6.9)$$

6.7. Geometrical Approximation for Tropospheric Measurements

As described in Section 6.6, the light path and therefore the trace gas absorption in the stratosphere is approximately the same for contemporary off-axis and zenith-sky measurements. Thus, a simple subtraction then yields the tropospheric (differential) slant column density:

$$DSCD_{\text{trop}} = DSCD_{\text{off-axis }(\alpha)} - DSCD_{\text{zenith }(90°)} \qquad (6.10)$$

with the elevation angle α. If we also assume that the most probable scattering altitude is located above the trace gas layer, the tropospheric air mass factor can be approximated by:

$$AMF_{\text{geom}} = \frac{1}{\sin(\alpha)} \qquad (6.11)$$

Combining these assumptions with Equation 6.8 gives the tropospheric vertical column density:

$$\text{VCD}_{\text{trop}} = \frac{\text{DSCD}_{\text{trop}}}{\text{DAMF}_{\text{trop}}} = \frac{\text{DSCD}_{\alpha} - \text{DSCD}_{90°}}{\text{AMF}_{\text{geom},\alpha} - \text{AMF}_{\text{geom},90°}} = \frac{\text{DSCD}_{\alpha} - \text{DSCD}_{90°}}{\sin(\alpha)^{-1} - 1} \tag{6.12}$$

(Wagner et al., 2010; Pinardi and Hendrick, 2008)

6.8. Conversion from Slant Column Densities to Volume Mixing Ratios

As introduced in Section 2.1, the volume mixing ratio $\text{VMR} = {n_{\text{gas}}}/{n_{\text{air}}}$ as the quotient of number densities describes the atmospheric fraction of a trace gas. The number density of air can be estimated using the ideal gas law:

$$n_{\text{air}} = \frac{N_{\text{air}}}{V_{\text{air}}} = \frac{p_{\text{air}} \cdot k_{\text{B}}}{T_{\text{air}}} = \frac{p_{\text{air}} \cdot N_{\text{A}}}{T_{\text{air}} \cdot R} \tag{6.13}$$

The calculation of the number density of the trace gas can be done in different ways:

- One possibility is using the geometric approximation described above, assuming a typical mixing layer height (MLH):

$$n_{\text{gas,geom}} = \frac{\text{VCD}_{\text{trop}}}{\text{MLH}} \qquad \Longrightarrow \qquad \text{VMR}_{\text{geom}} = \frac{\text{VCD}_{\text{trop}}}{\text{MLH}} \cdot \frac{T_{\text{air}} \cdot R}{p_{\text{air}} \cdot N_{\text{A}}} \tag{6.14}$$

  A disadvantage of this method is that one has to *assume* a typical mixing layer height, if no independent measurement of the MLH (e.g. using LIDAR) is available.

- A second possibility is using the mountain MAX-DOAS-approach (Gomez et al., 2013). The basic principle of this method is the estimation of the horizontal light path length L using the slant column density of the O_4-molecule with well-known number density:

$$n_{\text{gas}} = \frac{\text{DSCD}_{\text{gas},0°} - \text{DSCD}_{\text{gas},90°}}{L_{O_4}} \qquad \text{with} \qquad L_{O_4} = \frac{\text{DSCD}_{O_4,0°} - \text{DSCD}_{O_4,90°}}{n_{O_4}} \tag{6.15}$$

  while $n_{O_4} = \left(n_{O_2}\right)^2 = (0.20942 \cdot n_{\text{air}})^2$ can be easily calculated. Since the O_4-SCD is retrieved both in the visible and in the UV DOAS-Fit, this method can be used for both NO_2 and SO_2. However, the difference of the light paths due to the slightly different fitting windows in the UV for O_4 and SO_2 introduces an uncertainty, but this error is neglected in the following.

- The mountain MAX-DOAS-approach can be extended by using the slant column density of water vapor (H_2O). The number density of water vapor can easily be calculated if one has measured data for relative humidity, temperature and pressure. Since water vapor is only retrieved in the visible light range, it can only be used to determine the volume mixing ratio of NO_2.

7. Instruments

7.1. MAX-DOAS Instrument

In general, both MAX-DOAS instruments used for the measurement of shipping emissions in the MeSmarT project consist of a telescope on a pan-tilt head, an optical fiber bundle, one (Wedel) or two (Neuwerk) spectrometers each with an attached CCD detector and a computer. In the following sections, each part of the instrument is described in detail

7.1.1. Telescope

The telescope is used to collect the light in a specific viweing direction and to inject the light into the optical fiber. The telescope consists of a rainproof stainless steel box with an detachable side plate. This box contains the optical and electrical components and is attached to a pan-tilt head, which can either be mounted on a tripod (MAD-CAT Mainz) or on a fixed mounting plate (Wedel, Neuwerk, Celtic Explorer). The pan-tilt head allows to point in different azimuth angles (panning) as well as different elevation angles (tilting).
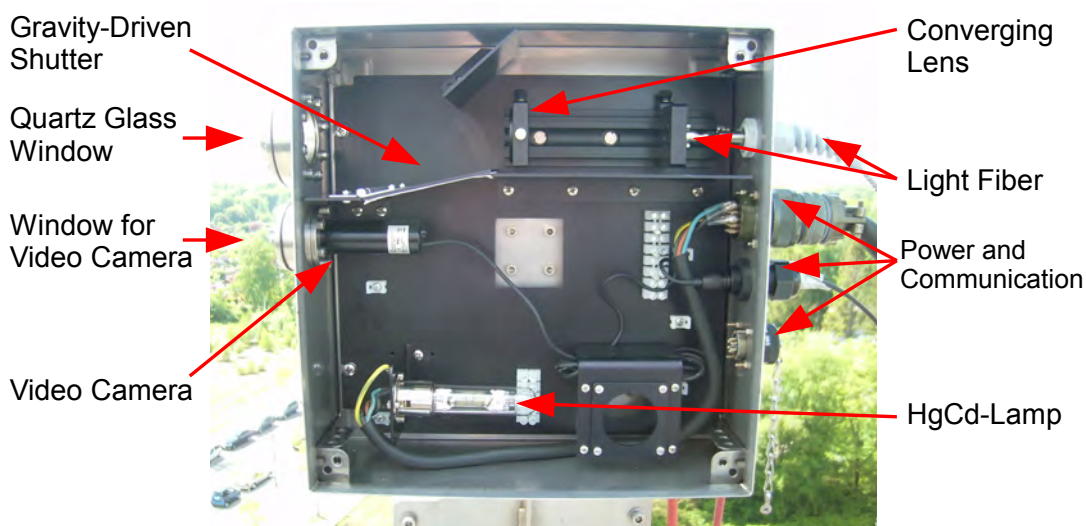

Figure 7.1.: Construction of the MAX-DOAS telescope box

The general construction of the telescope box can be seen in Figure 7.1. The scattered, incident light passes through the topmost window, is collected and bundled by a converging lens and injected into the light fiber. The window is made of quartz glass being transparent for UV radiation. The included video camera simplifies the manual alignment for certain viewing directions and the pictures taken by

the measurement software allow to check the measurement conditions later on. If the telescope is tilted 90° downwards, the "gravity-driven" shutter ((Peters, 2013)) hinges down preventing any exposure to ambient light. In this state, dark measurements for the determination of the CCD's dark current as well as line lamp measurements using the included HgCd lamp are possible.

7.1.2. Light Fiber

The optical light fiber cable is a bundle of cylindrical, thin and flexible quartz fibers. Each quartz fiber consists of an inner core, the surrounding cladding and an outer protective coating made of plastic. The core has a higher refraction index (typical value $n_{\mathrm{core}} = 1.48$) than the cladding ($n_{\mathrm{cladding}} = 1.46$). A light wave, injected into the core, propagates along the light fiber due to total reflection at the interface of core and cladding. Light fibers allow to transmit light on long distances with low conduction losses (Demtröder, 2009). The length and flexibility of the light fiber also allows a spatial separation of telescope and spectrometer. A weatherproof positioning of the spectrometer inside a building, for example, facilitates the temperature stabilization of spectrometer and CCD detector.

7.1.3. Spectrometer

A spectrometer is used for the spectral decomposition of light using a dispersive element like a prisma or reflection grating. For the measurements described in this thesis three spectrometers of the type Shamrock SR-303i have been used. This is a grating spectrometers in the common "Czerny-Turner" design with a reflective grating for the spectral decomposition. The basic construction of such a spectrometer is shown in Figure 7.2.
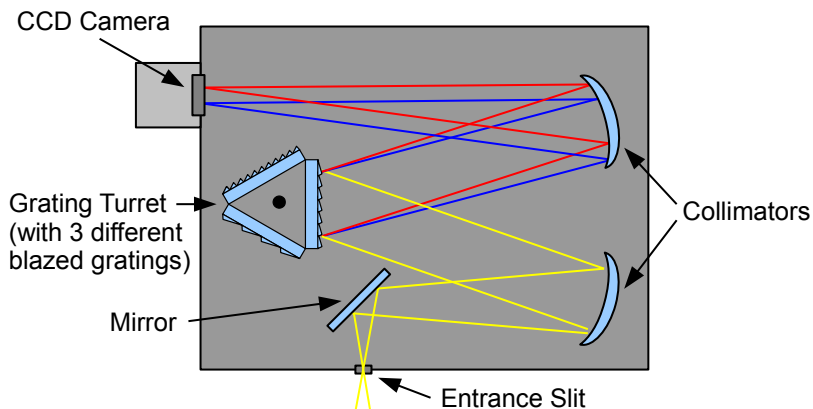

Figure 7.2.: Structure of a Czerny-Turner grating spectrometer (schematic)

The incident polychromatic light, which has passed through the entrance slit, is turned into a parallel light beam by the first collimator and then hits the reflection grating. The spectral decomposition on such a reflective grating is based on the wavelength dependence of the conditions for constructive and destructive interference of light waves. The condition to be fulfilled is the grating equation, which describes the relation between the path difference Δs, the line spacing d and the incidence and diffraction

angles α and β :

$$\Delta s = d \cdot (\sin \alpha + \sin \beta) = m \cdot \lambda \qquad (7.1)$$

with an even-numbered or odd-numbered diffraction order m resulting in constructive or destructive interference, respectively (Demtröder, 2009).

A second collimator focuses the light (and therefore the image of the entrance slit) onto the CCD image sensor (monochromatic images of the entrance slit are laterally shifted). One spatial dimension of the sensor plane is therefore used for the spectral decomposition, on the other dimension the light coming from the different fibers in the light cable is binned and averaged for the improvement of the signal to noise ratio.

The grating used in the MAX-DOAS instruments is a blazed grating, which is schematically shown in Figure 7.3. It consists of a multitude of tilted, step-shaped grooves which are oriented parallel to the entrance slit. The grooves, which are scratched into a glass plate, are metalized with aluminum to enhance the reflectivity. Adjusting the blaze angle and the shape of the steps optimizes the grating for a specific wavelength range, for which the efficiency is maximal. The maximum spectral resolution of a grating with N lines is limited by diffraction ($\lambda/\Delta\lambda = m \cdot N$) and can only be obtained, if the grating is optimal illuminated. (Demtröder, 2007)
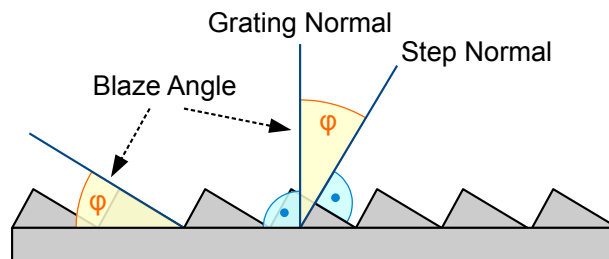

Figure 7.3.: Structure of a blazed grating (schematic)

7.1.4. CCD Camera

A charge-coupled device (CCD) is a two dimensional arrangement of metal oxide semiconductor (MOS) capacitors, the so-called *pixels*. The functionality of a CCD and therefore the path from the incident photons to the image can be divided into four different processes: charge generation, charge collection, charge transfer and charge measurement. Like in photo diodes, the charge generation in a metal-insulator-semiconductor structure is based on the inner photoelectric effect. When a photon with sufficient energy (higher than the band gap) hits the silicon body of the CCD it excites an electron (or more) from the valence band into the conduction band creating an electron hole pair. Recombination is avoided by applying an electric field. The charges are collected in the depletion region of the MOS capacitors. The charge transfer from the pixels to the output amplifier is done by shifting the charges line-by-line by applying a certain potential. The output diode then generates a voltage proportional to the amount of charge.

The advantage of a CCD detector is the good signal-to-noise ratio due to the high quantum efficiency and the low dark current and readout noise. The dark current is produced when electrons are excited ther-

mally. Another problem is electron diffusion leading to charge leakage between the pixels, especially when shrinking the pixel size for higher resolutions. The impact of these effects can be reduced considerably by cooling the detector. (Janesick, 2001; Demtröder, 2007)

7.1.5. Measurement Software and DOAS Data Analysis

The spectra obtained from the MAX-DOAS instrument are recorded by the measurement software AMAX_OMA (Richter, 1997). This computer program controls the movement of the pan-tilt head, the spectrometer, the CCD and the video camera. AMAX_OMA is capable of capturing single spectra as well as performing fully automated measurement sequences including nightly dark and line lamp calibration measurements.

The spectra captured by AMAX_OMA contain the light intensity (in counts) as a function of the pixel number. The calibration is done by execution of the program NKALIB which uses the line lamp measurements to transform the pixel number into a wavelength axis. NKALIB is called by the program NPREPARE which also rejects spectra with too small dynamic range (low light conditions) or pixels affected by high energetic cosmic radiation. Another program called RESOLUT calculates the slit function of the instrument which are later convoluted with the absorption cross-sections to account for the spectral resolution of the instrument. Both programs subtract the dark signal from the spectra minimizing the impact of the dark current and noise. The DOAS fit is performed by the program NLIN_D which delivers the slant column densities as well as the residuals.

7.2. Airpointer In-situ Device

The Airpointer in-situ device is a a commercially available system which combines four different instruments in a compact, air-conditioned housing. The manufacturer is MLU (`http://www.mlu.eu/`). The Airpointer device measures carbon dioxide (CO_2), nitrous oxides ($NO_x = NO + NO_2$), sulfur dioxide (SO_2) and ozone (O_3). Table 7.1 shows more detailed information about the different instruments and their measurement methods.

Table 7.1.: Airpointer in-situ device: measured trace gases, corresponding measuring techniques, measuring ranges and detection limits [Source: MLU (manufacturer), `http://www.mlu.eu/`]

Trace gas	CO_2	O_3	NO,NO_2	SO_2
Measuring technique	Non-dispersive IR spectroscopy LI-COR LI820	UV absorption (EN 14625)	NO Chemi-luminescence (EN 14211)	UV fluorescence (EN 14212)
Detection limit	1 ppm	0.5 ppb	0.4 ppb	0.25 ppb
Measuring range	up to 20 000 ppm	up to 200 ppm	up to 20 ppm	up to 10 ppm
Measuring period	1 s	<30 s	<60 s	<90 s

However, due to calibration problems the SO_2 values measured by the Airpointer are shifted into the negative. To compensate this, an additive offset of $+0.5$ ppb in Wedel and $+1.1$ ppb in Neuwerk was applied to the SO_2 data.

8. The MeSmarT Project

The project MeSmarT (measurements of shipping emissions in the marine troposphere) is a cooperation between the University of Bremen, the German Federal Maritime and Hydrographic Agency (Bundesamt für Seeschifffahrt und Hydrographie, BSH) and the Helmholtz-Zentrum Geesthacht. To estimate the impact of shipping emissions on the atmospheric boundary layer chemistry, elevated signals (ship peaks) as well as background concentrations of shipping-related trace gases and particles are monitored with various methods. Using different measurement techniques like in-situ measurements and remote sensing makes it possible to cover a wide range of relevant pollutants and to determine their spatial as well as seasonal distribution.

In-situ techniques are used to measure CO_2, NO_x, SO_2 and O_3, NO_2 and SO_2 as well by differential optical absorption spectroscopy (DOAS), a remote sensing technique that is applied on ground-based stations (Wedel and Neuwerk) as well as on ship cruises (Celtic Explorer) and airplane flights (iDOAS/AirMAP). Both methods deliver informations about the various trace gases with a time resolution of a few minutes. There are also active high volume filter sampling measurements of particles a time resolution of hours to days. These samples are analyzed for sulphate, nitrate, organics and elemental composition to gain information about ship emission derived compounds and their sources, sinks and conversion processes. Passive sampling measurements of NO_2 and SO_2 with a time resolution of months and satellite measurements (also with the DOAS technique) are used to determine the long-term effects of regulations like the *Sulfur Emission Control Areas* (SECA). The measured data is then the basis for the modeling of the physical and chemical processes with the aim to understand the impact of shipping emissions on coastal areas and the marine troposphere.

Therefore, the long-term objectives of the MeSmart project are:

- Assessment of different measurement systems such as remote sensing, in-situ, and passive sampling measurements as methods for long-term monitoring of shipping emissions in the North and Baltic Sea

- Establishment of remote sensing instruments like MAX-DOAS to support the surveillance of international emission regulations

- Improvement of ship emission data bases by measurements of the actual distribution of trace gases and aerosols related to ship emission

- Validation of satellite measurements and model data

- Description of the influence of ship emissions and its secondary products on the marine environment

- Development of a concept for controlling ship emissions

The web page of the project is accessible under `http://www.mesmart.de`, where a more detailed description of the project, measurement results, publications and contact information can be found.

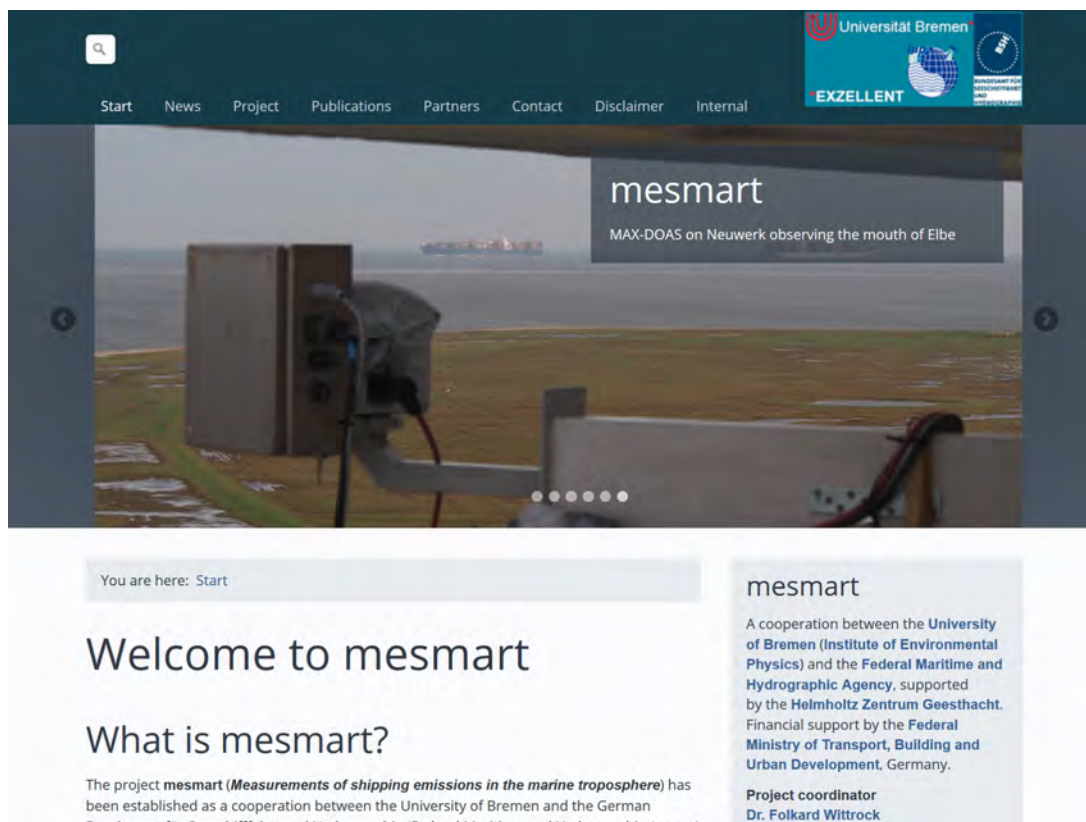Figure 8.1.: MeSMarT project web page, accessible under `http://www.mesmart.de` (10.05.2014)

9. Measurement Sites

This chapter describes the MeSmarT measurement sites in Wedel and on the island Neuwerk. The geografic position of both stations can be seen in the map in Figure 9.1.
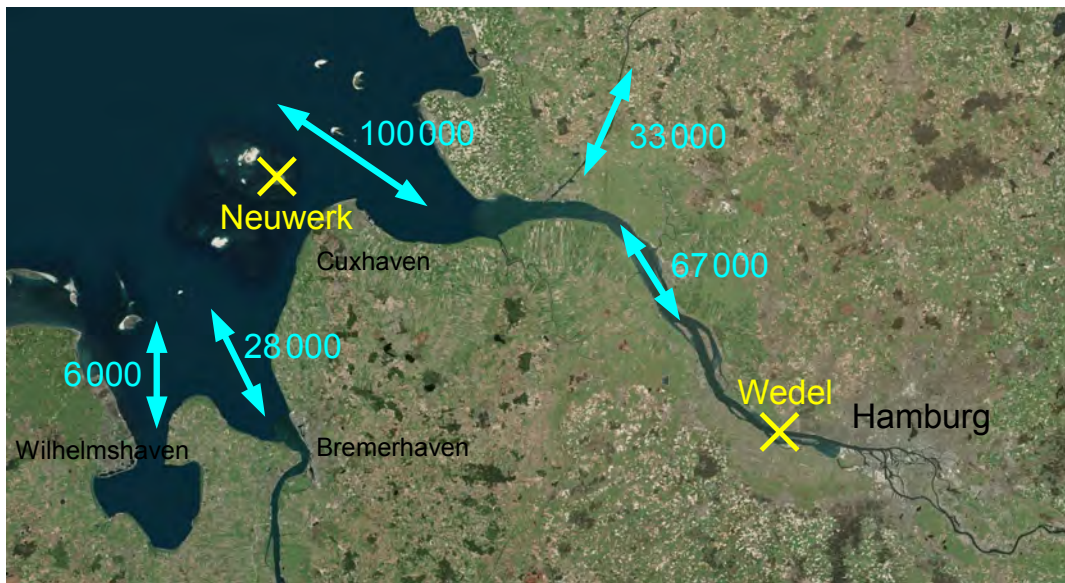

Figure 9.1.: Overview map for the river Elbe from Hamburg to the North Sea. Measurement sites depicted in yellow, number of ship movements (data from 2011/2012) in cyan. [Data source: Wasser- und Schifffahrtsverwaltung des Bundes (WSV), `http://www.wsd-nord.wsv.de/Schiff-WaStr/Schifffahrt/Schiffsverkehr_und_Gueterumschlag/index.html` and `http://www.ast-nordwest.gdws.wsv.de/schifffahrt/verkehr_gueterumschlag/index.html` (09.05.2014). Image source: `http://www.bing.com/maps/` (01.04.2014)]
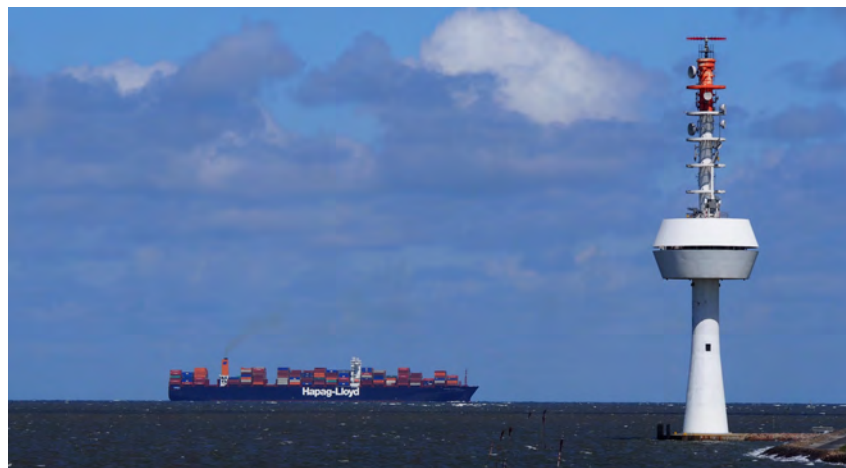

Figure 9.2.: MeSmarT Measurement site on the radar tower Neuwerk

9.1. Neuwerk

Neuwerk is a small island (about $3\,km^2$, ≈ 40 inhabitants) in the German Wadden Sea. It is located northwest of Cuxhaven at the mouth of the river Elbe, roughly $8\,km$ apart from the Coast. Historically, Neuwerk belongs to the city of Hamburg and is part of the Borough Hamburg-Mitte. Although Neuwerk is surrounded by the Hamburg Wadden Sea National Park it is relatively close to the main shipping lane from the North Sea into the river Elbe, which is the reason why it was chosen as a measurement site for the MeSmarT project. The measurement devices, including a two-channel MAX-DOAS instrument (UV and visible), the Airpointer in-situ measurement device, a high volume filter sampler and passive samplers as well as a semi-professional weather station and the AIS receiver, are positioned on main platform of a $60\,m$ height radar tower in a height of about $30\,m$ (see Figures 9.3 and 9.4).
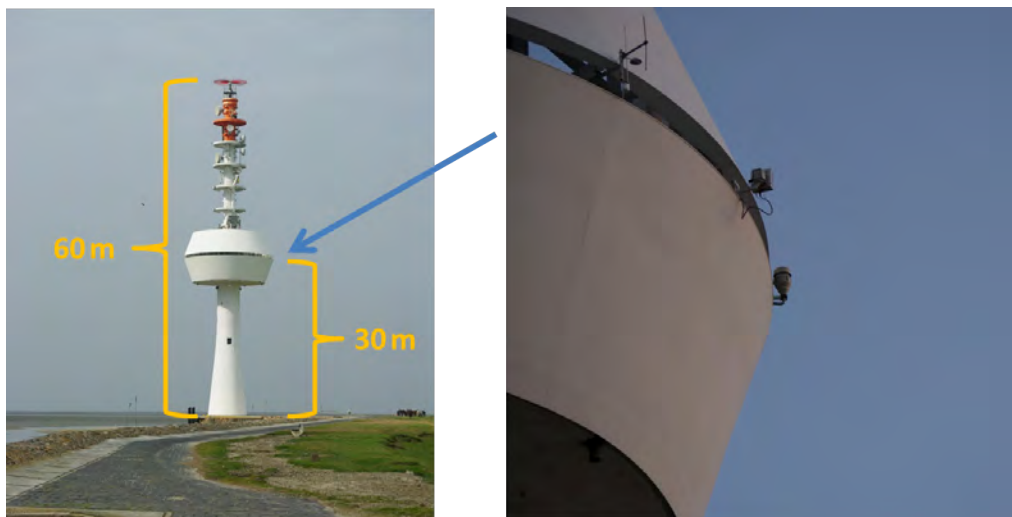

Figure 9.3.: Radar tower Neuwerk with the measurement devices installed at the main platform

MAX-DOAS   AIS Data   Wind (HPA)

Weather Station   Airpointer (in-situ)   High Volume Sampler
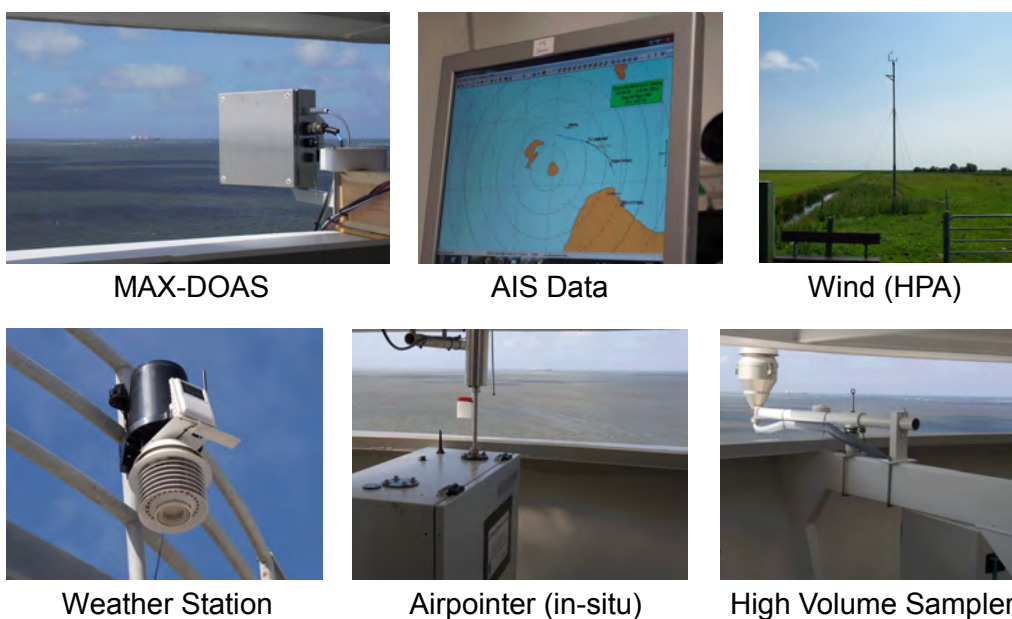
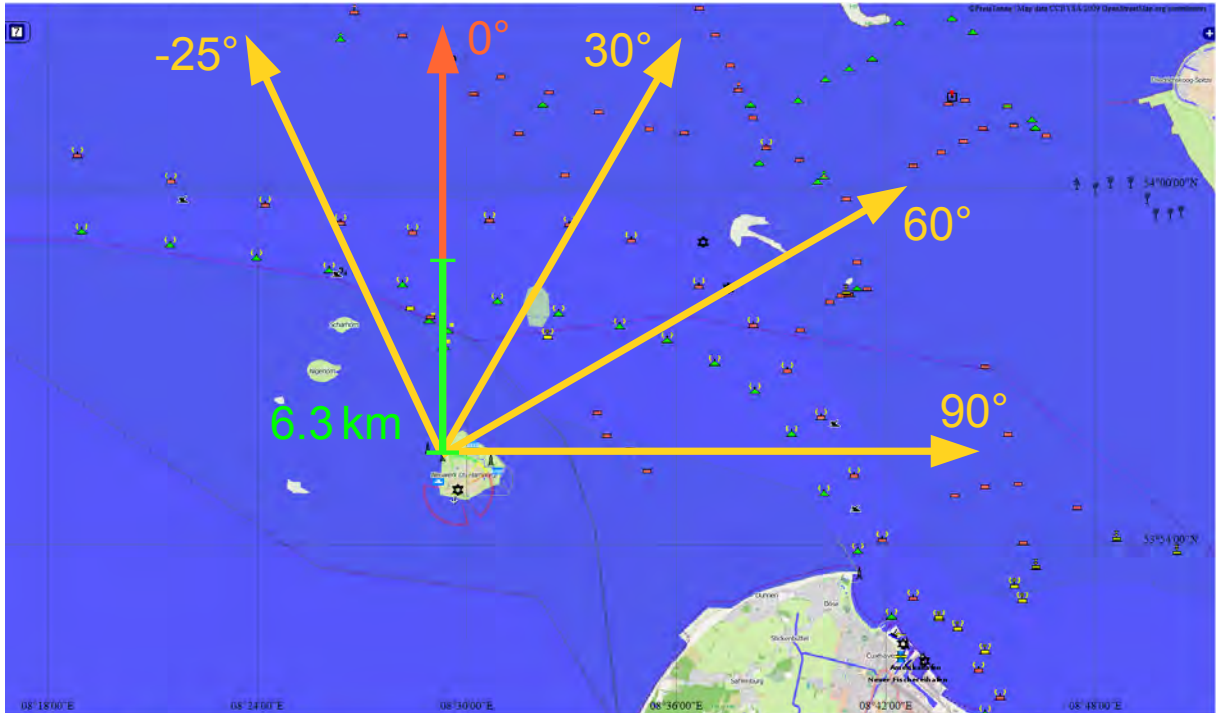Figure 9.4.: Measurement devices on Neuwerk

Figure 9.5.: Viewing Directions of the Neuwerk MAX-DOAS instrument towards the main shipping lane, which is designated by the line of buoys [Image source: `http://www.freie-tonne.de` (16.07.2013), based on Open Street Map data]

Figure 9.5 shows the azimuth viewing directions of the MAX-DOAS instrument. The viewing directions point towards the main shipping lane, which is marked by the schematic buoys. As can be seen from Figure 9.6, there often is a lot of ship traffic passing Neuwerk.

Figure 9.6.: View towards the main shipping lane

Additional wind data is measured by the Hamburg Port Authority (HPA) on Neuwerk (see Figure 9.4) and the neighboring island Scharhörn.

9.2. Wedel

Wedel is a small German town to the west of Hamburg. It is located at the right (northern) bank of the river Elbe and lies within the metropolitan area of Hamburg. The measurement devices are set up in and around a small building (see Figure 9.7) at the Wedel branch office of the Water and Shipping Authority of Hamburg (WSA), very close to the river (about 10 m apart). How close the ships are passing can also be seen in Figure 9.8, that shows the building from the other side.

Figure 9.7.: Measurement devices in Wedel

Figure 9.8.: Measurement site in Wedel

Included is a one-channel MAX-DOAS instrument measuring in the UV (see Figure 9.9), the Airpointer in-situ device, passive samplers, a high volume sampler and an AIS receiver. The azimuthal viewing directions of the MAX-DOAS instrument are shown in Figure 9.10.

Figure 9.9.: MAX-DOAS instrument in Wedel
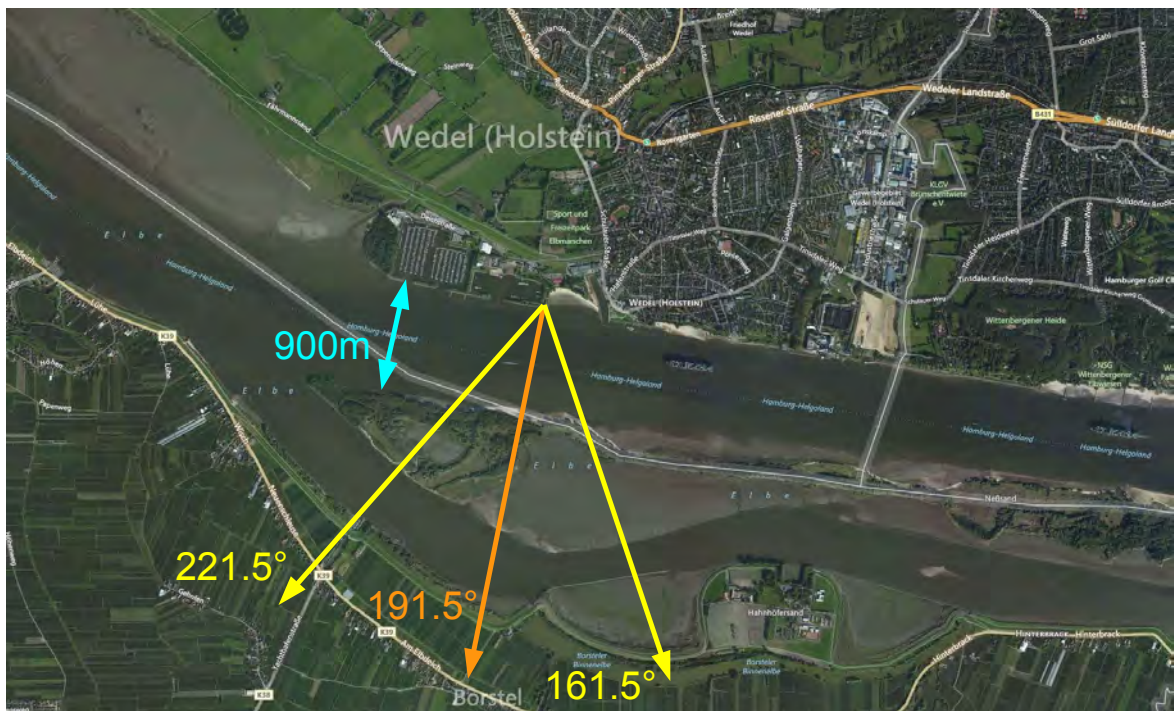
Figure 9.10.: Viewing Directions of the Wedel MAX-DOAS instrument towards the river Elbe [Image source: http://www.bing.com/maps/ (01.04.2014)]

10. Results of the SO$_2$ Retrieval Study

This chapter shows and discusses the results of the SO$_2$ fitting retrieval analysis that has been performed during the work for this thesis. The most appropriate set of fitting parameters were used for the MAX-DOAS SO$_2$ measurements in Neuwerk and Wedel presented in Chapters 11 and 12.

For this retrieval study, spectra measured in the UV with the MAX-DOAS instruments on Neuwerk and in Wedel have been fitted (DOAS technique see Chapter 6) with systematically varying parameters to find the best parameter set for SO$_2$ fits. First, a manual evaluation based on guesses, trial and error, and settings already used before was executed, to gain fit parameters that give more or less acceptable results. Than four days with good weather conditions (especially good visiblity) and high amounts of measured SO$_2$ have been selected, three different days on Neuwerk (24.08.2013, 26.08.2013 and 28.08.2013) with clearly visible SO$_2$ peaks coinciding with large NO$_2$ peaks and one day in Wedel (17.06.2013) with temporarily strongly enhanced SO$_2$ background values and several peaks. From the huge number of measurements on these days in various elevation and azimuth angles a subset of measurements with high SO$_2$ amounts were selected.

After this inital phase, a systematic analysis of these measurements was performed, varying the start and end wavelength of the fitting window, the used trace gas cross-sections and the number of coefficients for the DOAS polynomial:

- **Start wavelength:** ranging between 306 nm and 349.5 nm for Wedel and between 306.5 nm and 349.5 nm for Neuwerk, in 0.5 nm steps.

- **End wavelength:** ranging between 306.5 nm and 350 nm for Wedel and between 307 nm and 350 nm for Neuwerk, in 0.5 nm steps.

- **cross-sections:** SO$_2$ for 293 K (Bogumil et al., 2003), Ring (R_S_30_0_GOME2_GAUSS08.AIR, GOMETRAN simulation from Marco Vountas), stratospheric O$_3$ for 223 K (Bogumil et al., 2003), troposheric NO$_2$ for 298 K (Vandaele et al., 1996) and as an additional cross-section for O$_3$ either the one for 243 K, 273 K or 293 K (Bogumil et al., 2003). The SO$_2$ cross-section was always used, the other cross-sections were systematically added in the sequence above.

- **Number of polynomial coefficients:** 3 to 6

This sums up to a number of 107 184 fits that have been done for each single measurement (each spectrum) on each day chosen for Neuwerk, and 109 648 in Wedel. The fits were done on off-axis data using the zenith measurement closest in time as a reference. A constant intensity offset was applied compensating for stray-light effects.

Figures 10.1, 10.2, 10.3 and 10.4 show the mean RMS (root mean square) over all fitting windows (every possible combination of start and end wavelength) for each combination of cross-sections and number of polynomial coefficients for the four evaluated days.
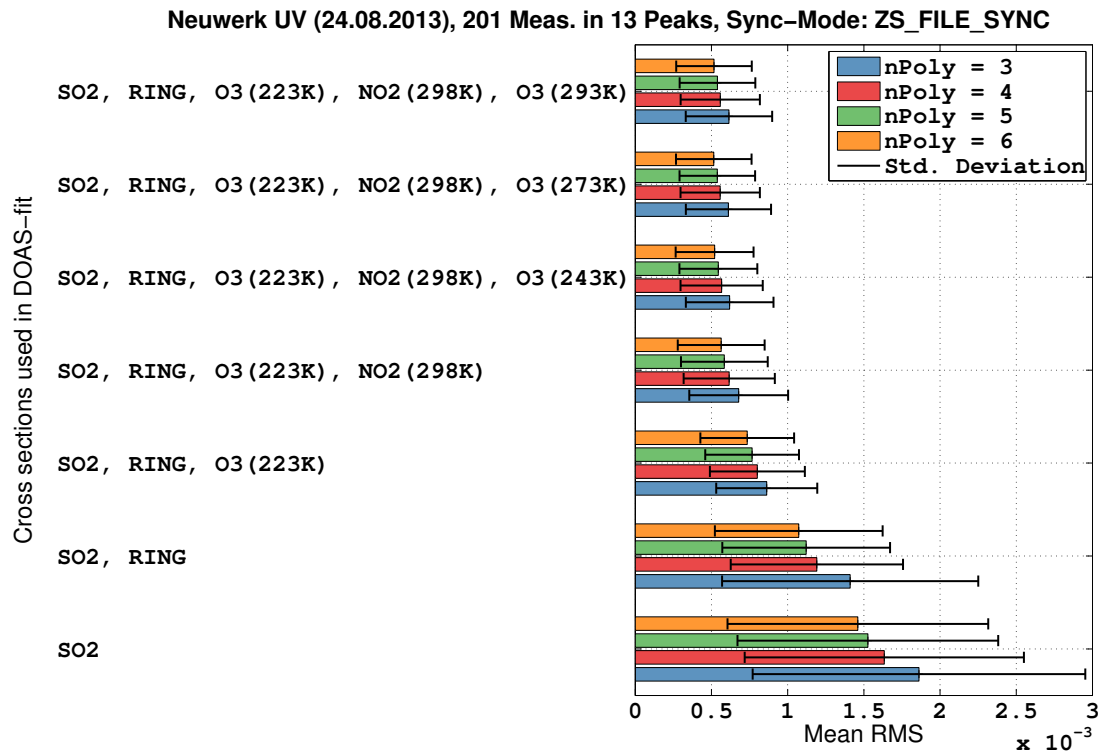
Neuwerk UV (24.08.2013), 201 Meas. in 13 Peaks, Sync−Mode: ZS_FILE_SYNC

Figure 10.1.: Mean RMS over all possible fitting windows for different cross-sections and numbers of polynomial coefficents for Neuwerk on Saturday, 24 August 2013. The black error bars represent one standard deviation.

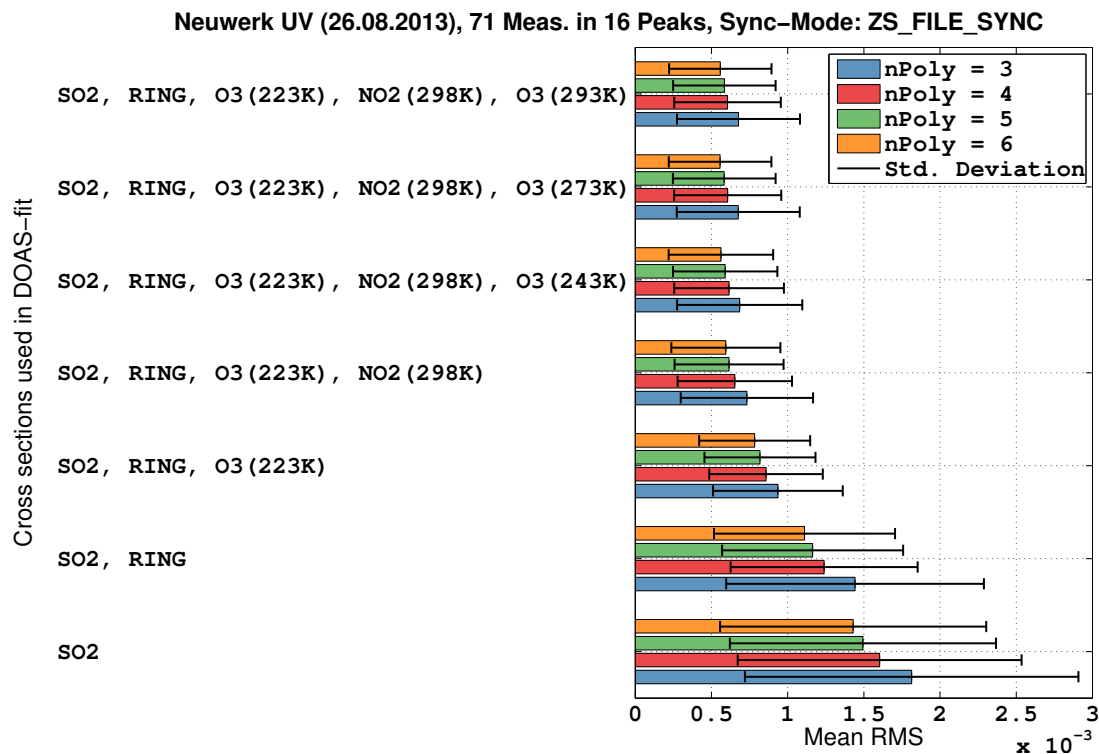**Neuwerk UV (26.08.2013), 71 Meas. in 16 Peaks, Sync−Mode: ZS_FILE_SYNC**

Figure 10.2.: Mean RMS over all possible fitting windows for different cross-sections and numbers of polynomial coefficents for Neuwerk on Monday, 26 August 2013. The black error bars represent one standard deviation.

Figure 10.3.: Mean RMS over all possible fitting windows for different cross-sections and numbers of polynomial coefficents for Neuwerk on Wednesday, 28 August 2013. The black error bars represent one standard deviation.
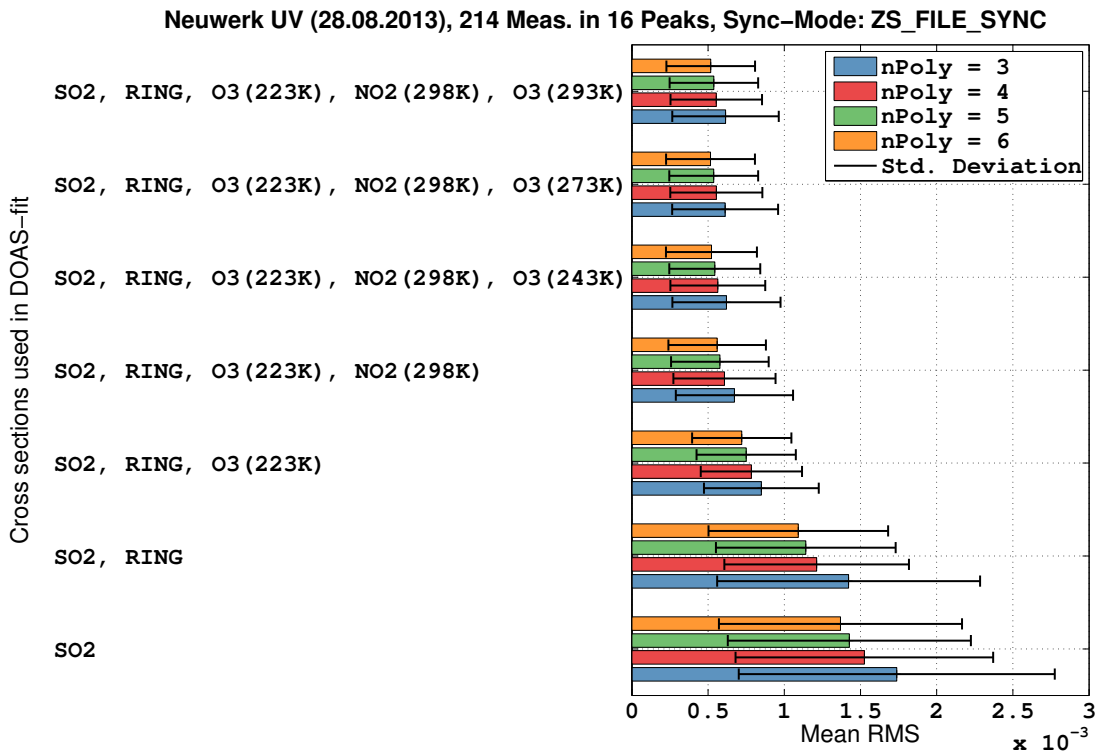

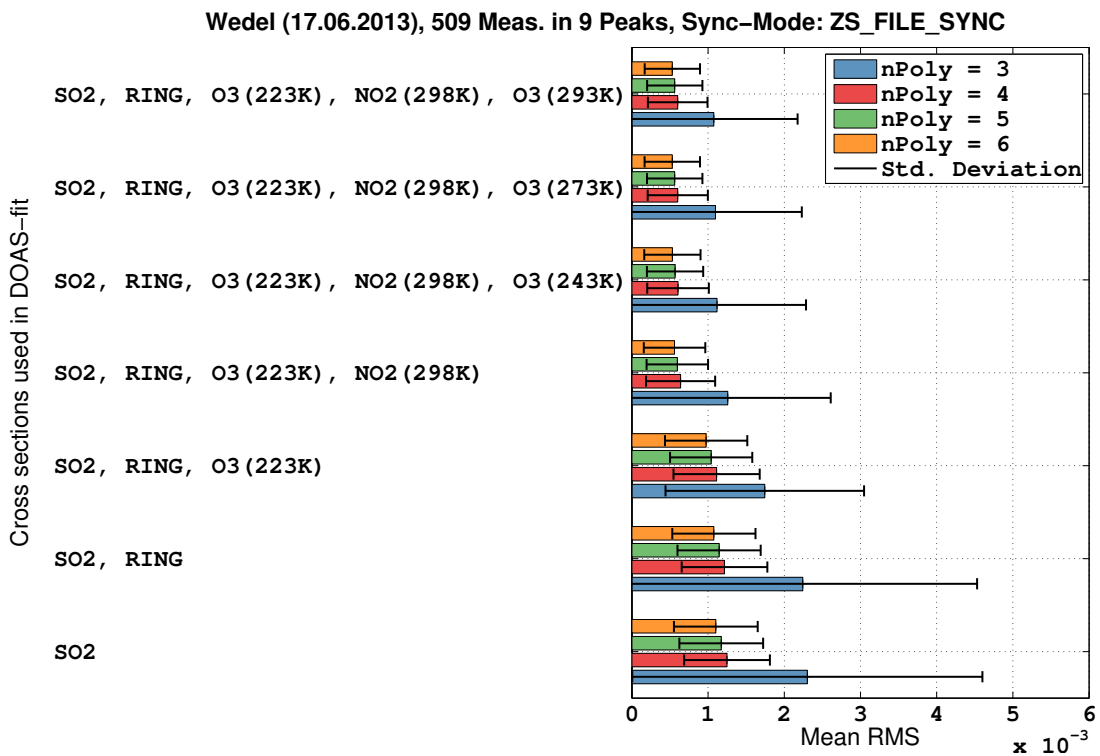
Figure 10.4.: Mean RMS over all possible fitting windows for different cross-sections and numbers of polynomial coefficents for Wedel on Wednesday, 17 June 2013. The black error bars represent one standard deviation.

These plots show that the largest benefits are achieved by adding the Ring, stratospheric O_3 and tropospheric NO_2 cross-sections. Adding a second ozone cross-section for higher temperatures gives only a slight improvement nearly regardless of which one is chosen. The most appropriate number of polynomial coefficients is 6 (i.e. a polynomial degree of 5).

To find the best fitting window, several criteria have to be fulfilled: The SO_2 fitting error and RMS have to be small and the resulting slant column density (SCD) should deliver reasonable values. In the following for the sake of clarity only the plots for Saturday, 24 August 2013 on Neuwerk are shown, because the results for all days look very similar. Only the plots with the cross-sections for SO_2, Ring, O_3 (223 K and 273 K) and NO_2 and 6 polynomial coefficients are shown, since these combination gives the best mean RMS.
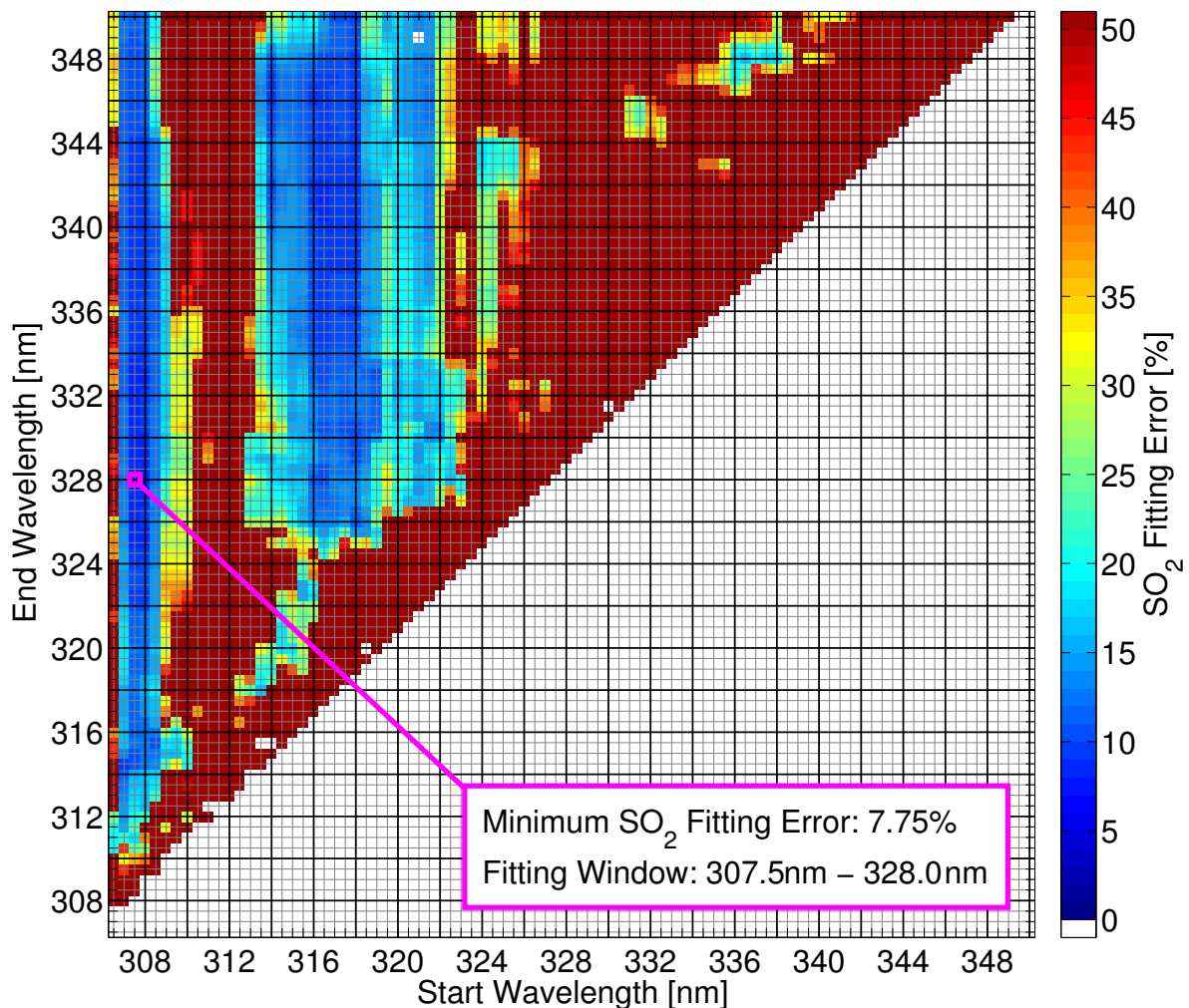

Figure 10.5.: Raster plot of SO_2 fitting errors depending on the fitting window for Neuwerk on Saturday, 24 August 2013. The x-axis denotes the start wavelength, the y-axis the end wavelength of the fit. The combination with minimum fitting error is highlighted in purple.

Figure 10.5 shows the SO_2 fitting error in a color-coded raster plot for all evaluated fitting windows. Every little colored square denotes one combination of start and end wavelength. The minimum SO_2

fitting error is highlighted by a purple box. It is achieved for the wavelength range 307.5 to 328 nm. However, there are a lot of combinations of start and end wavelength that produce fitting errors nearly as low as these combination. They group in the two larger blue patches. The first minimum patch can be seen on the left for a start wavelength of 307.5 to 308 nm and an end wavelength larger than 314 nm. Another blue patch can be observed in the upper middle for a start wavelength of 316 to 318 nm and an end wavelength larger than 326 nm. The actual end wavelength seems to be nearly irrelevant for both.

To evaluate which of these region gives the better results, we have to look into the resulting SCDs, that are plotted in Figures 10.6 and 10.7 for two different color-scales, one reaching up to values of 4×10^{16} molecules/cm^2, the other one up to 2×10^{17} molecules/cm^2.
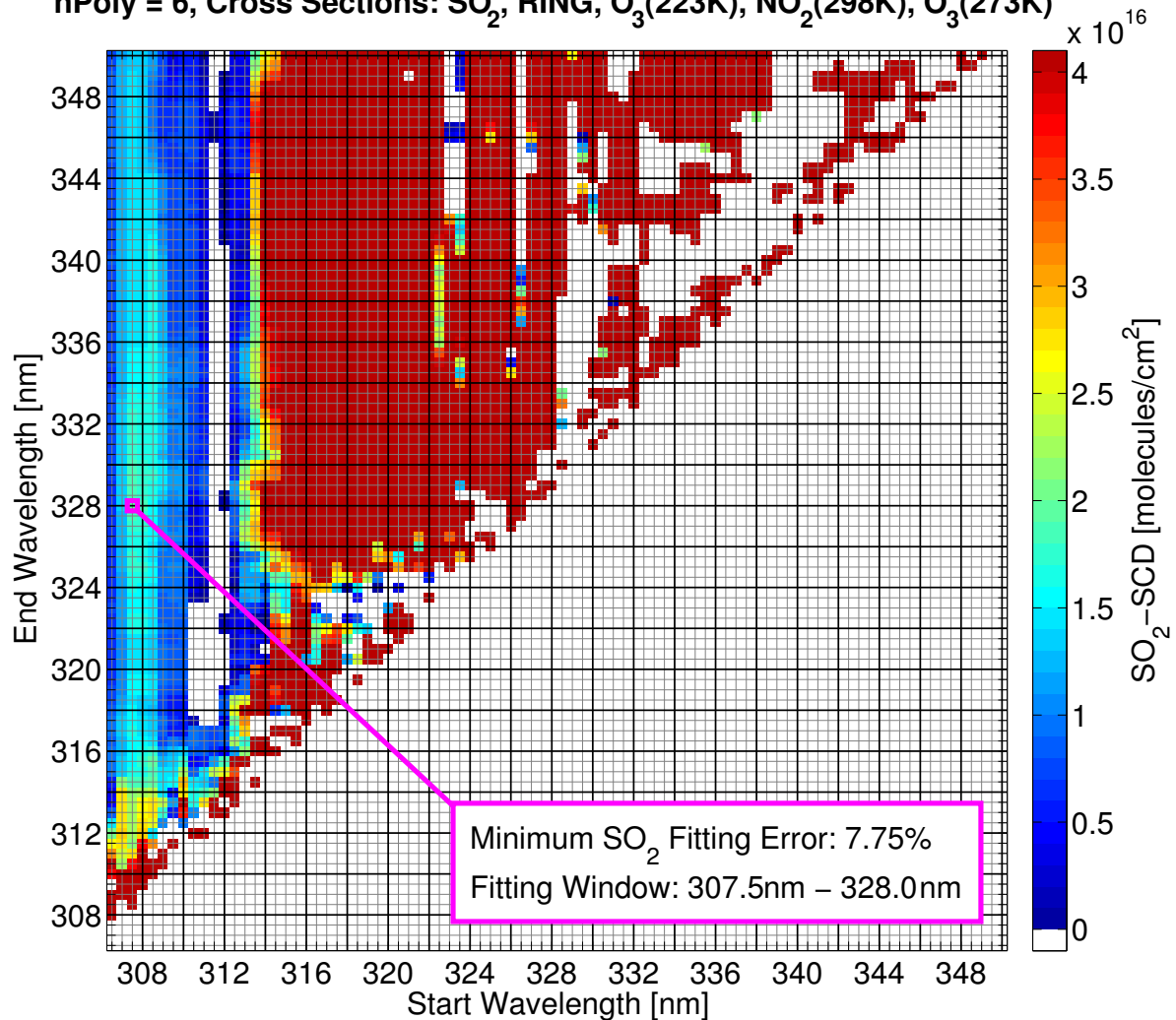

Figure 10.6.: Raster plot of SO$_2$-SCD (up to 4×10^{16} molecules/cm^2) depending on the fitting window for Neuwerk on Saturday, 24 August 2013. The x-axis denotes the start wavelength, the y-axis the end wavelength of the fit. The combination with minimum fitting error (see Figure 10.5) is highlighted in purple. Negative and missing values are shown in white.

Figure 10.6 shows that for the first identified patch (start wavelength of 307.5 to 308 nm) the SCDs are nearly constant for the entirely patch, with a hardly visible maxmimum of about 2×10^{16} molecules/cm^2 for end wavelengths of 328 to 330 nm. This is a reasonable magnitude for an average over more than

200 single SO$_2$ masurements on Neuwerk. For the second identified patch (start wavelength of 316 to 318 nm) the resulting SCDs (see Figure 10.7) are also quite stable, but substantially higher, reaching up to 1.3×10^{17} molecules/cm^2. This indeed is nearly one order of magnitude higher and therefore not reasonable.

Figure 10.7.: Raster plot of SO$_2$-SCD (up to 2×10^{17} molecules/cm^2) depending on the fitting window for Neuwerk on Saturday, 24 August 2013. The x-axis denotes the start wavelength, the y-axis the end wavelength of the fit. The combination with minimum fitting error (see Figure 10.5) is highlighted in purple. Negative and missing values are shown in white.

To determine which wavelength range of the first patch is the best one, having a closer look on the RMS is necessary. Figure 10.8 shows the corresponding RMS values. What can easily be seen is, that the RMS shows a strong dependence on the start wavelength, with lower values for higher start wavelengths. Hardly any dependence on the end wavelength is observed for start wavelengths up to 310 nm.

Weighing all aspects against each other a fitting window of 307.5 to 328 nm, including the cross-sections for SO$_2$ (293 K), Ring, O$_3$ (223 K and 273 K) and NO$_2$ (298 K) and 6 polynomial coefficients (polynomial degree of 5) seems to be the best setting. It gives the minimum SO$_2$ fitting error and the highest reasonable SCDs. However, slightly changes of the end wavelength will have nearly no effect on the

Neuwerk UV (24.08.2013), 201 Meas. in 13 Peaks, Sync–Mode: ZS_FILE_SYNC nPoly = 6, Cross Sections: SO$_2$, RING, O$_3$(223K), NO$_2$(298K), O$_3$(273K)
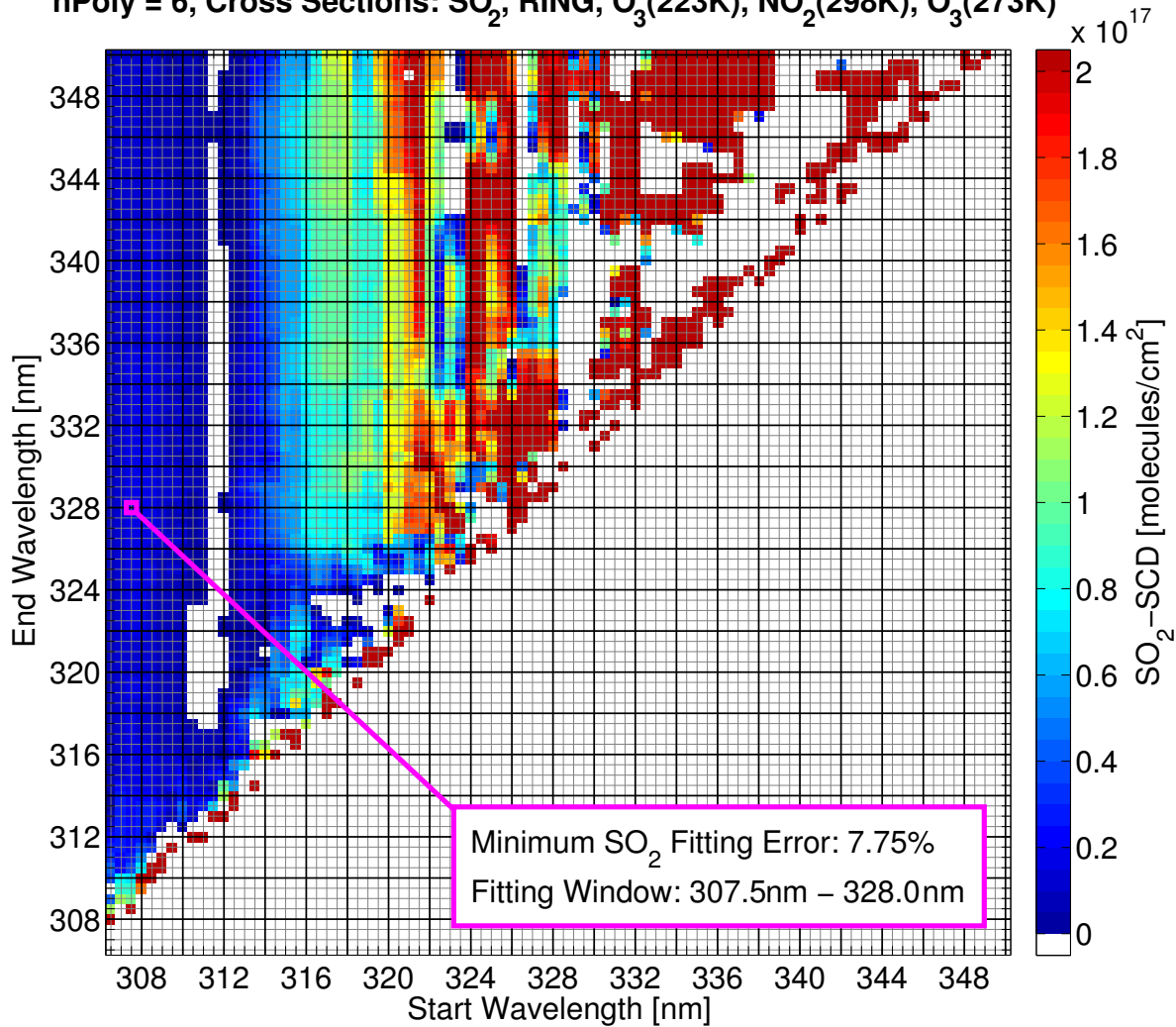
Mean RMS: 5.15×10^{-4}

Minimum SO$_2$ Fitting Error: 7.75%

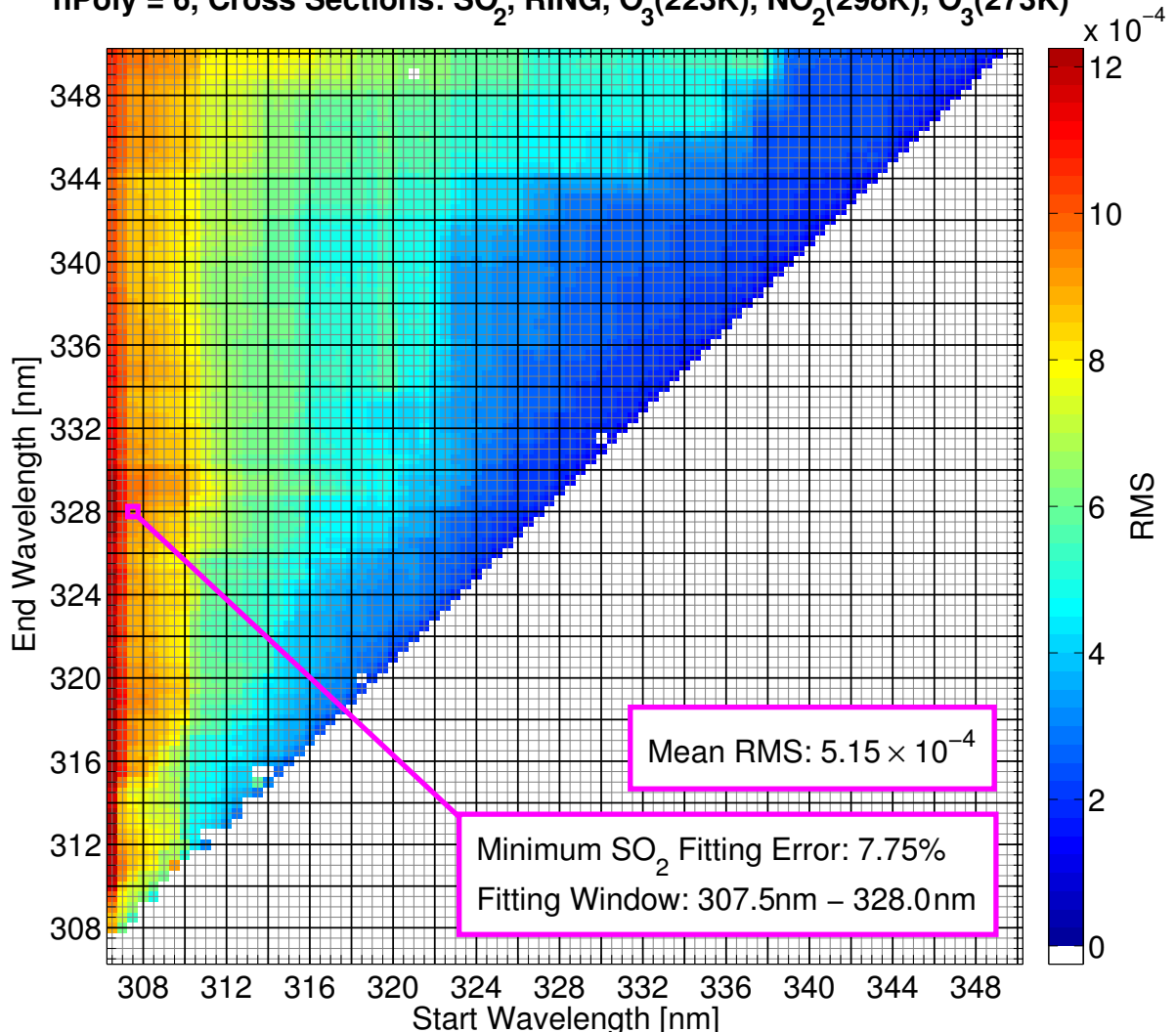Fitting Window: 307.5nm – 328.0nm

Figure 10.8.: Raster plot of RMS depending on the fitting window for Neuwerk on Saturday, 24 August 2013. The x-axis denotes the start wavelength, the y-axis the end wavelength of the fit. The combination with minimum fitting error (see Figure 10.8) is highlighted in purple. The mean RMS is denoted in the upper text box.

resulting measurements, as can be seen in Figure 10.6.

For the confirmation whether the selected cross-sections and polynomial degree are appropriate not only for the mean RMS over all possible fitting windows, but also for the selected wavelength range, Figure 10.9) shows an overview over SO$_2$ fitting error and RMS values for this fitting window. From this plot it can be seen that the selected parameter delivers the lowest RMS and a very SO$_2$ low fitting error. It illustrates also, that the second ozone cross-section can be exchanged to the one for 293 K, without much changes of the results.

An example fit for a typical SO$_2$ ship emission peak for Monday, 19 August 2013 in the morning is shown in Figure 10.10. The agreement between the reference SO$_2$ cross-section (solid line) and the fit (dashed line) is very good, especially for the low wavelengths, where the differential optical depth is higher.
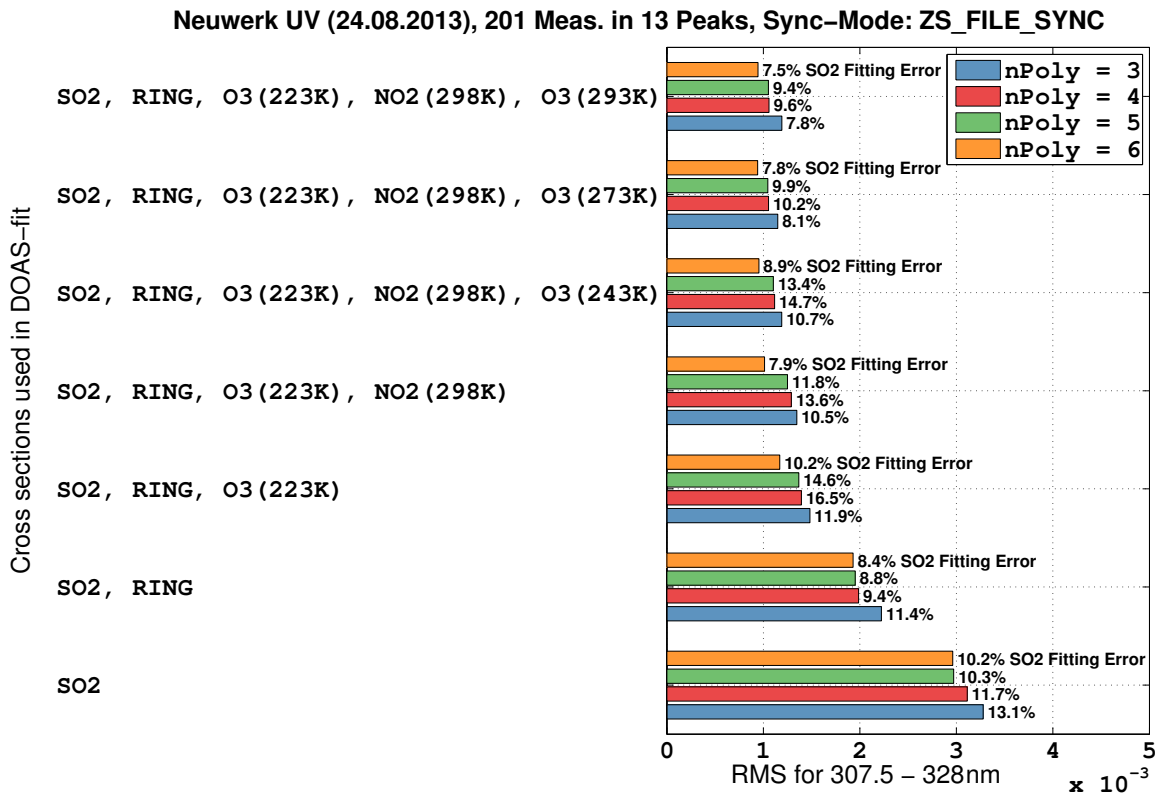
Figure 10.9.: RMS and SO$_2$ fitting error for fitting window 307.5–328 nm for different cross-sections and numbers of polynomial coefficents for Neuwerk on Saturday, 24 August 2013.
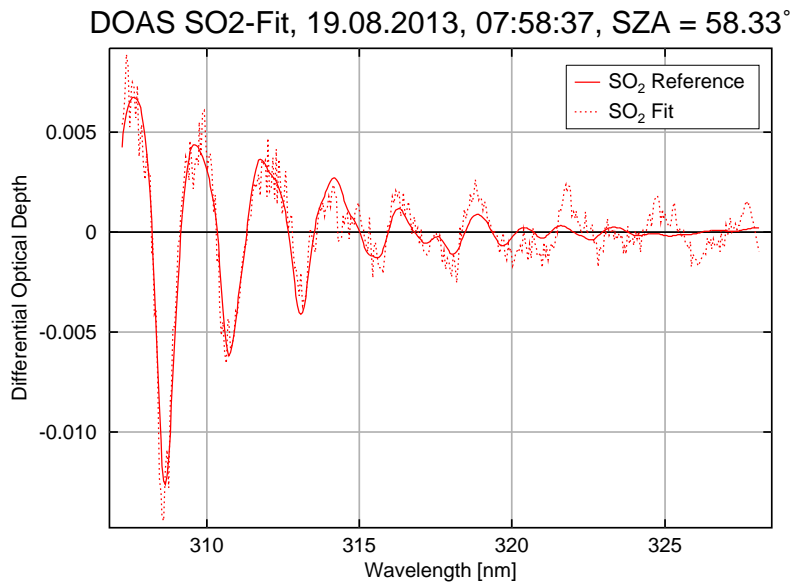

Figure 10.10.: Example of an SO$_2$ fit for Neuwerk on Monday, 19 August 2013. The solid line shows the reference SO$_2$ cross-section and the dashed line shows the fit.

A summary of the fit settings, together with those for NO$_2$ in UV and visible, can be found in the appendix.

11. Measurement Results for Wedel

This chapter presents the measurement results for the Wedel station. The fitting parameter for the MAX-DOAS measurements can be found in the appendix.

11.1. Suitability of the Wedel Station
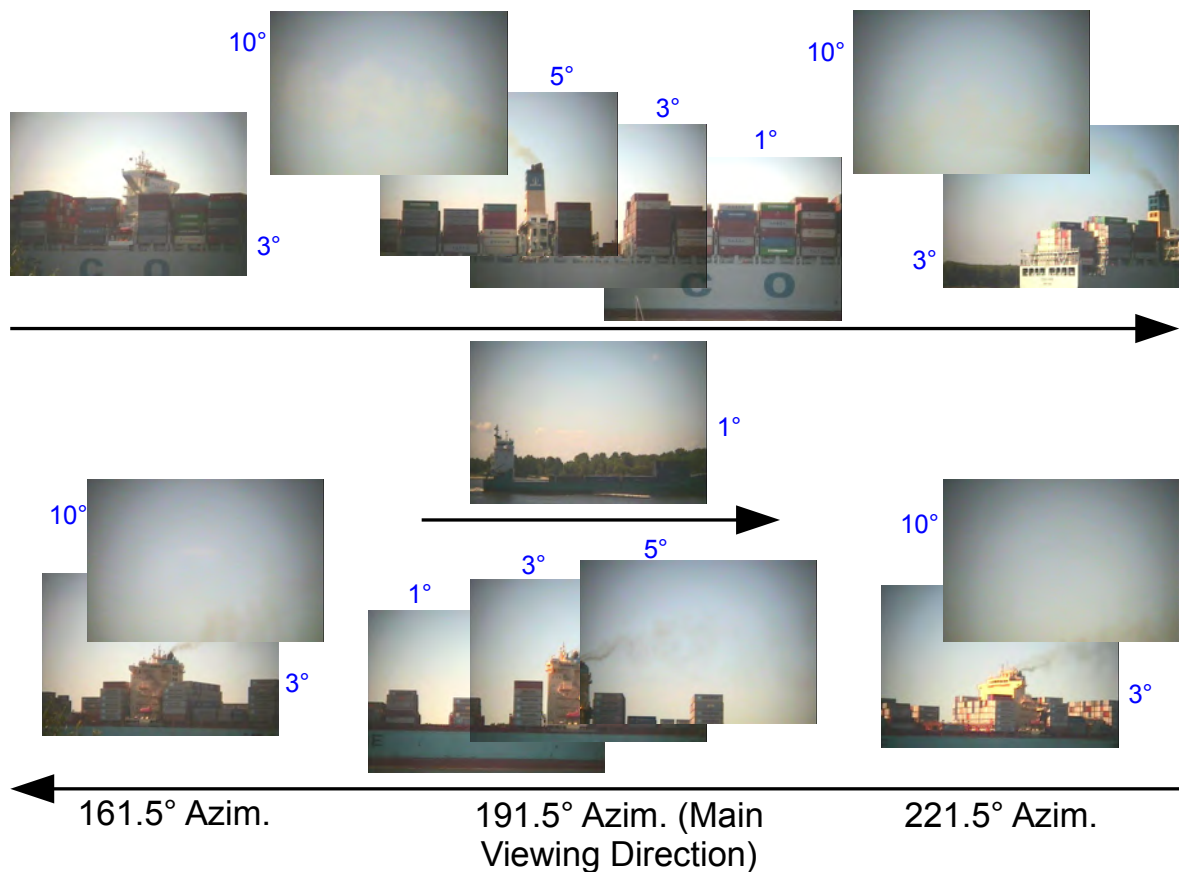
Figure 11.1.: Snapshots from three different ships taken at various azimuth and elevation angles with the video camera included in the MAX-DOAS telescope in Wedel

Figure 11.1 shows some images taken from the video camera included in the MAX-DOAS telescope in Wedel. These pictures illustrate how close the ships are passing the instrument. It also demonstrates that the line of sight (LOS) for large ships in the lowermost elevation angles is covered by the hull and superstructures of the ships and therefore the light path is blocked and significantly shortened. The

exhausted ship plumes are also clearly visible in the images, which shows that at this station the MAX-DOAS instrument can measure right trough the recently exhausted plumes. But it also illustrates, that measurements at different elevation angles are necessary to cover all the different ship sizes.

11.2. Single-Day Measurements

Figure 11.2a shows typical MAX-DOAS NO_2 and SO_2 slant column measurements in Wedel (for fitting parameter see appendix). For comparison, typical in-situ NO_2 and SO_2 volume mixing ratios are plotted in Figure 11.2b, to the right.

(a) MAX-DOAS NO_2 and SO_2 SCD

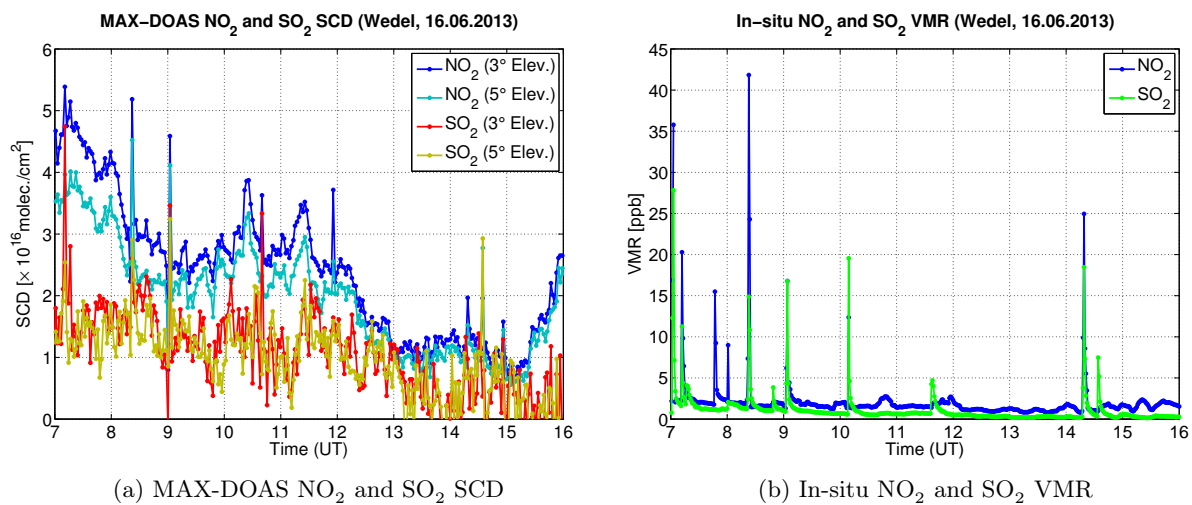(b) In-situ NO_2 and SO_2 VMR

Figure 11.2.: MAX-DOAS SCD (main viewing direction: $191.5°$ azimuth) and in-situ VMR measured in Wedel on Sunday, 16 June 2013

In both plots a lot of peaks can be seen, coming most likely from the passing ships. For most of the peaks measured by one of the instruments, corresponding peaks at approximately the same points in time can be seen in the measurements of the other instrument. However, the peaks measured by the in-situ instrument are very sharp and high and clearly stick out of the background. Some of the MAX-DOAS peaks are sharp and others broader. For most of the days in Wedel, the SO_2 peaks can clearly be distinguished from the noisy background, since the background pollution of SO_2 is quite low. For NO_2 on the other hand, the background pollution is often very dominant and the ship emission peaks are quite small. This general behaviour can also be seen in the plots for two other sample days in Figures 11.2a,b and 11.2a,b.

Using the geometric approximation described in Chapter 6.7 it is possible to calculate volume mixing ratios from the slant column densities measured by the MAX-DOAS instrument. For this, a mixing layer height has to be assumed. An indication for the right assumption gives the background pollution. Since the background NO_2 and SO_2 normally is well-mixed in the boundary layer around the instruments, both measurement devices despite their different measurement techniques should measure similar background values. Figure 11.5 shows the resulting geometric NO_2 and SO_2 VMRs for a two-hour time period of the SCDs measured on Friday, 28 June 2013 (shown above in Figure 11.3a) and the corresponding in-situ values.

(a) MAX-DOAS NO$_2$ and SO$_2$ SCD

(b) In-situ NO$_2$ and SO$_2$ VMR

Figure 11.3.: MAX-DOAS SCD (main viewing direction: 191.5° azimuth) and in-situ VMR measured in Wedel on Friday, 28 June 2013

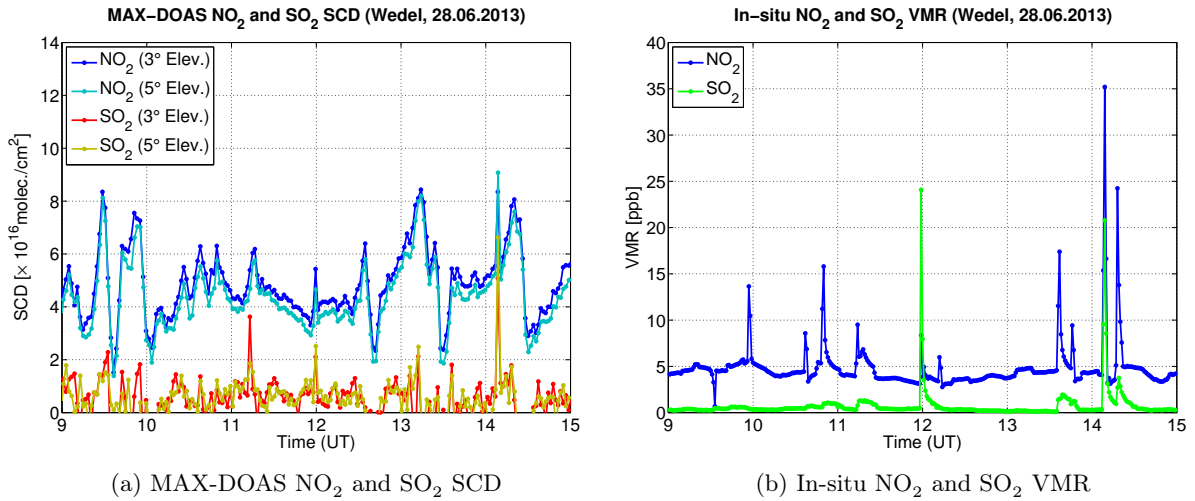(a) MAX-DOAS NO$_2$ and SO$_2$ SCD

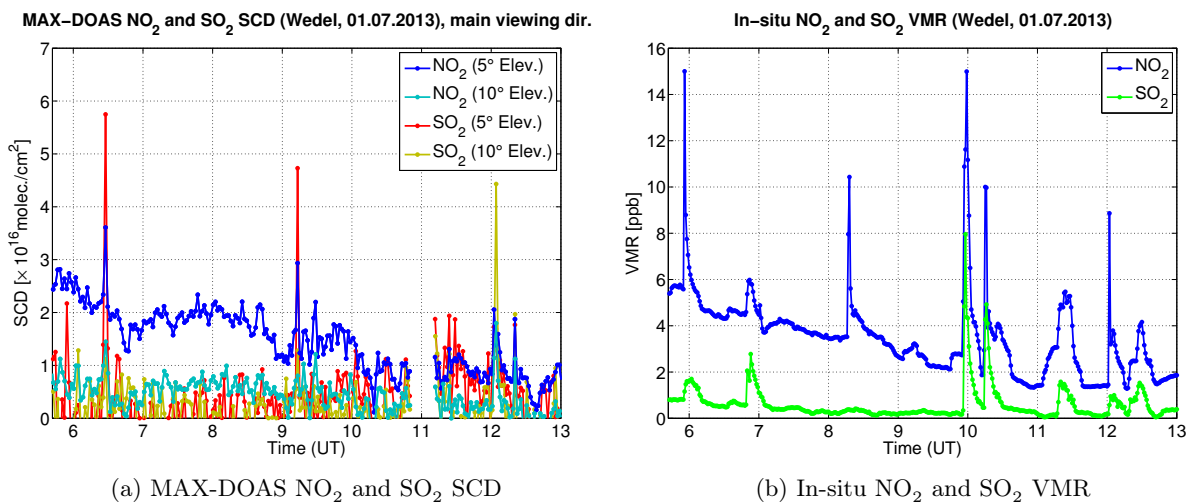(b) In-situ NO$_2$ and SO$_2$ VMR

Figure 11.4.: MAX-DOAS SCD (main viewing direction: 191.5° azimuth) and in-situ VMR measured in Wedel on Monday, 01 July 2013
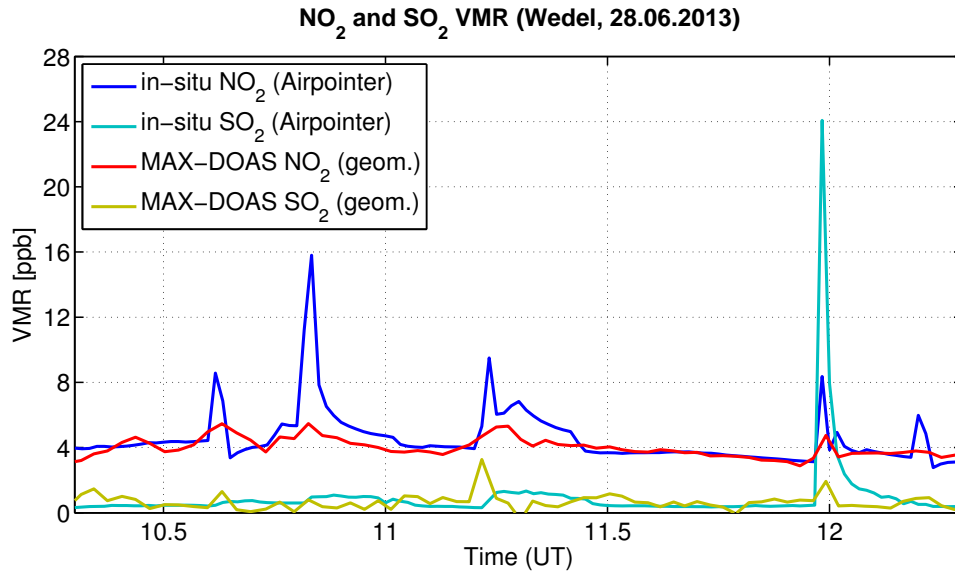
Figure 11.5.: Comparison of MAX-DOAS and in-situ NO_2 and SO_2 VMRs measured in Wedel on Friday, 28 June 2013. The MAX-DOAS VMRs were calculated using the geometric approximation for $3°$ elevation in the main viewing azimuth direction. The assumed mixing layer height is $250\,m$.

As can be seen from the figure, the background NO_2-VMR of about $4\,ppb$ is reproduced very well. Since the MAX-DOAS measurements represent an average over a certain light path, the measured peaks are very small compared to the in-situ peaks. This is even more obvious in Figure 11.5, which shows a short time period on Sunday, 16 June 2013 (corresponding SCDs: see Figure 11.2a). On this day, again the background agrees very well ($\approx 2\,ppb$), but the MAX-DOAS peaks are even smaller compared to the intense in-situ peaks.

For the MAX-DOAS NO_2 measurements there are also hints that at the time of the measurements most of the NO_x in the plumes is still in the form of NO and had not enough time to be converted to NO_2. This will be discussed later in Section 11.4.

In consideration of the differences a more detailed single-day comparison of the volume mixing ratios seems not to be reasonable. Therefore, the further, more detailed analysis will focus on the slant column densities and thereby on MAX-DOAS measurements. However, a long-term analysis of VMR time-series and wind direction dependence will follow in Sections 11.6 and 11.5.
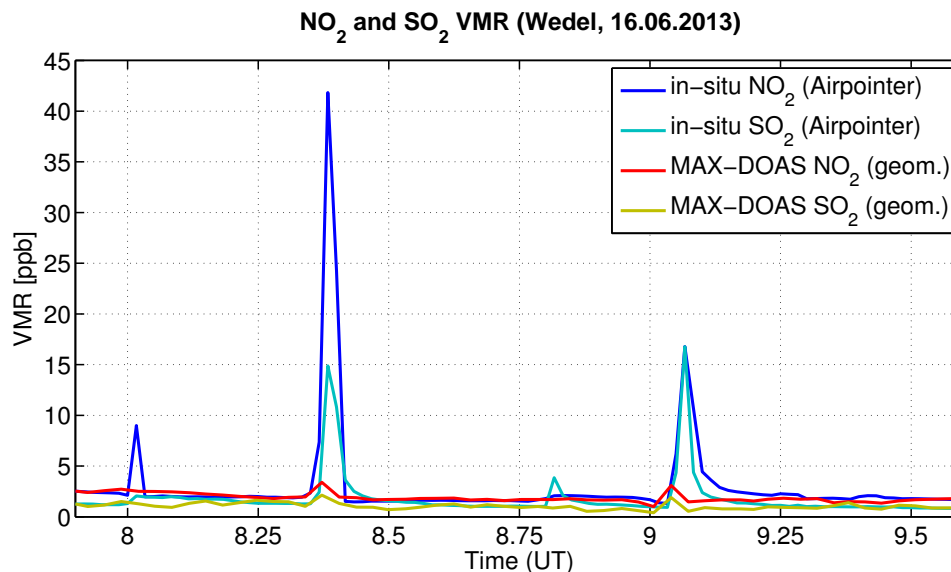
NO$_2$ and SO$_2$ VMR (Wedel, 16.06.2013)

Figure 11.6.: Comparison of MAX-DOAS and in-situ NO$_2$ and SO$_2$ VMRs measured in Wedel on Sunday, 16 June 2013. The MAX-DOAS VMRs were calculated using the geometric approximation for 5° elevation in the main viewing azimuth direction. The assumed mixing layer height is 500 m.

11.3. Allocation to Ships

For a further detailed analysis and to allocate the measured peaks to the corresponding emitting ship, it is indispensable to look into the AIS (*Automatic Identification System*) data as well as into the wind direction data.

Considering all the disadvantages of the measurement location in Wedel for the MAX-DOAS measurements mentioned above, one could ask why a MAX-DOAS system is even needed in Wedel. And why not only an in-situ instrument is installed at this station. Well, this chapter should highlight the various advantage of a MAX-DOAS over an in-situ device.

The first advantage points at measurement times and weather conditions. Although the used passive MAX-DOAS technique works only on daytime, which clearly is a disadvantage compared to the continuous working in-situ device, the in-situ device needs wind coming from southerly directions to measure the plumes of the passing ships (see also the map in Figure 9.10). If the wind is coming from the north, the plumes are blown away from the instrument and cannot be measured. The MAX-DOAS device, however, can measure the ship plumes independently from the wind direction.

Such a situation is shown in Figure 11.7. This plot contains three sub-plots: The upper one shows the MAX-DOAS and in-situ VMRs. The middle one includes various information about passing ships. The vertical bars indicate when a ship is in the line-of-sight of the MAX-DOAS instrument. Solid bars represent ships coming from the left and going to the right (in Wedel: from east to west), dashed bars vice versa. The color of the bars indicates the ship length, with small ships appearing in blue and very large ships in red. The lower sub-plot displays the wind speed and direction measured in Finkenwerder (blue and red) and Brokdorf (cyan and orange).

This figure shows that for northerly winds the measured in-situ curves, especially for SO$_2$, are very flat and show no ship emission peaks. However, the MAX-DOAS measurements contain clearly visible peaks
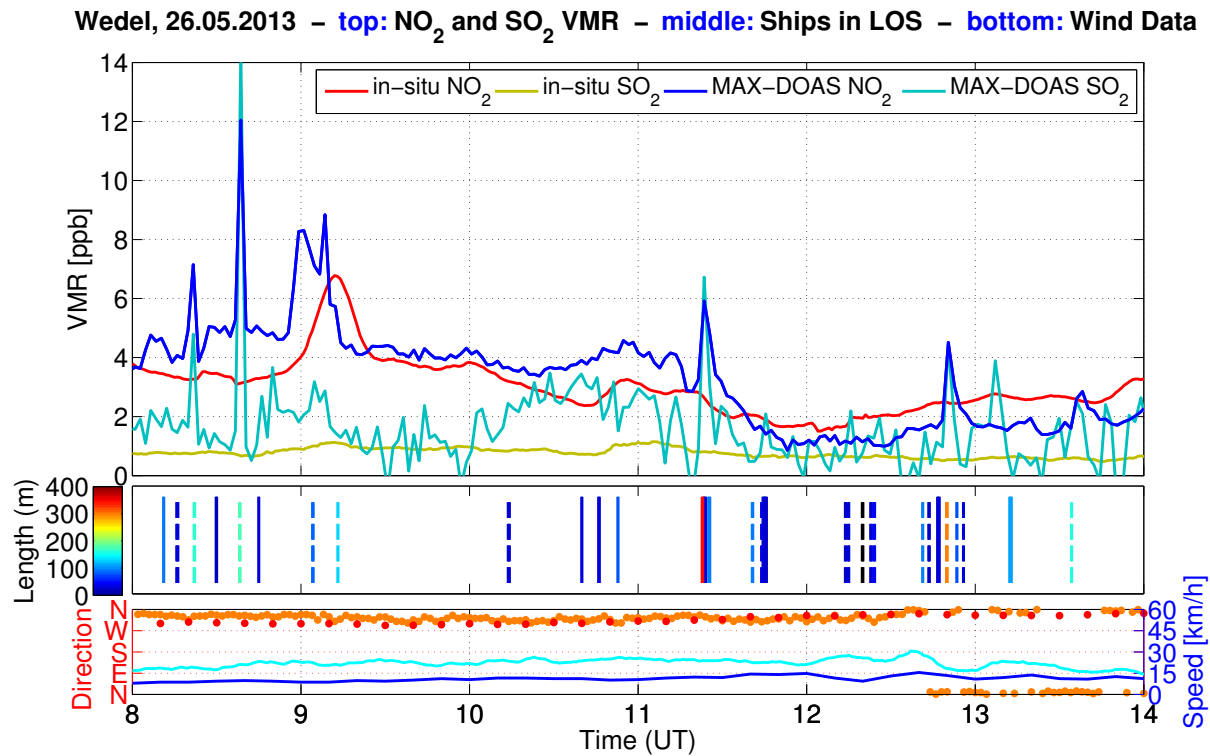
Figure 11.7.: VMR, AIS and wind data for Wedel on Sunday, 26 May 2013.
On top: in-situ and MAX-DOAS VMRs (geom., 3° elev., main dir., MLH = 150 m)
In the middle: bars indicating that a ship is in the line-of-sight, solid bars: ship moves from left to right (east to west), dashed vice versa, colors representing ship length
On the bottom: wind speed and direction from Finkenwerder (blue and red) and Brokdorf (cyan and orange)

when larger ships pass by the instrument, despite the plume is blown away from the instruments into the south.

Another advantage of the MAX-DOAS instrument is the possibility to point and measure in various elevation and azimuth angles. This makes it possible to gain information on the vertical and horizontal distribution of the emissions, whereas the in-situ device measures at one fixed location. The Figures 11.8 and 11.9 show NO_2 slant column densities measured in various elevation angles during the vertical scans.

In both figures, a lot of ship emission peaks can be seen, reaching into different heights. Especially the big ships often produce high peaks. Sometimes there are even large peaks in the 30° elevation angle visible. It can also be observed that the lowermost viewing directions are sometimes blocked by the ships shortening the light path and strongly decreasing the measured NO_2-SCDs for a short time, leading to dips in the curves.

On Saturday, 20 July 2013 (see Figure 11.8), there were very low wind speeds in the morning. The three very large ships (>300 m) that passed by, led to huge peaks in all viewing angles, especially in 10° elevation. How much of the strongly enhanced NO_2 levels in the morning comes from these ships and how much comes from traffic, remains unclear.

In Figure 11.10, which is a zoom in Figure 11.9, horizontal scans for two different elevation angles are

Wedel, 20.07.2013 – top: NO₂–SCD – middle: Ships in LOS – bottom: Wind Data
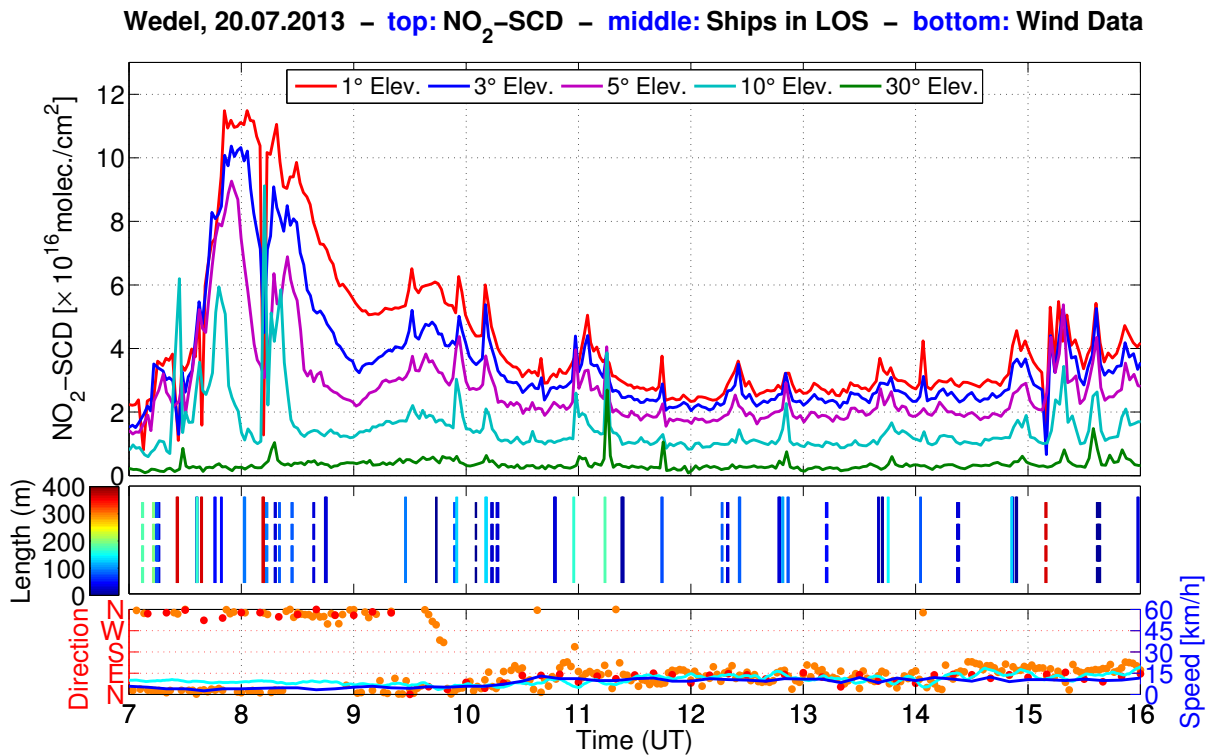
Figure 11.8.: NO₂-SCD, AIS and wind data for Wedel on Saturday, 20 July 2013.
On top: MAX-DOAS NO₂-SCDs measured in the main azimuth direction
In the middle: bars indicating that a ship is in the line-of-sight, solid bars: ship moves from left to right (east to west), dashed vice versa, colors representing ship length
On the bottom: wind speed and direction from Finkenwerder (blue and red) and Brokdorf (cyan and orange)

Wedel, 16.06.2013 – top: NO₂–SCD – middle: Ships in LOS – bottom: Wind Data
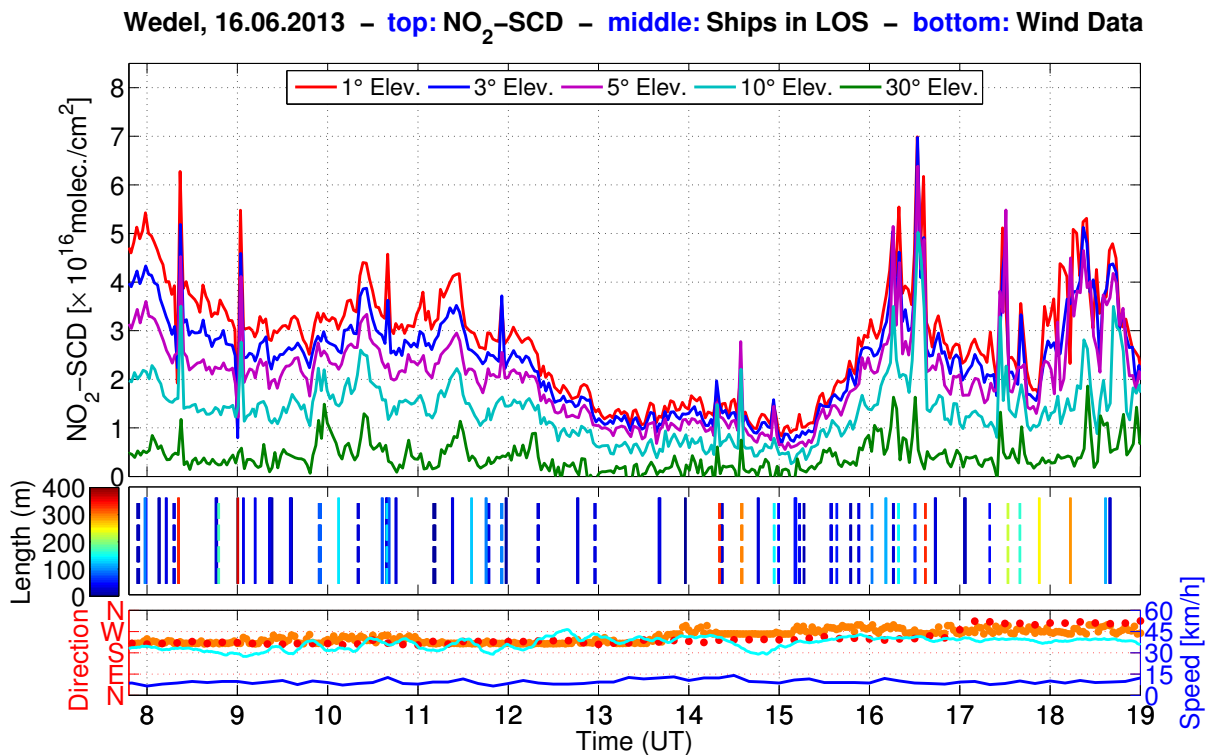
Figure 11.9.: NO₂-SCD (vertical scan), AIS and wind data for Wedel on Sunday, 16 June 2013.

plotted.

Figure 11.10.: NO$_2$-SCD (horizontal scan), AIS and wind data for Wedel on Sunday, 16 June 2013.
On top: MAX-DOAS NO$_2$-SCDs measured in horizontal scans
In the middle: bars indicating that a ship is in the line-of-sight, solid bars: ship moves from left to right (east to west), dashed vice versa, colors representing ship length
On the bottom: wind speed and direction from Finkenwerder (blue and red) and Brokdorf (cyan and orange)
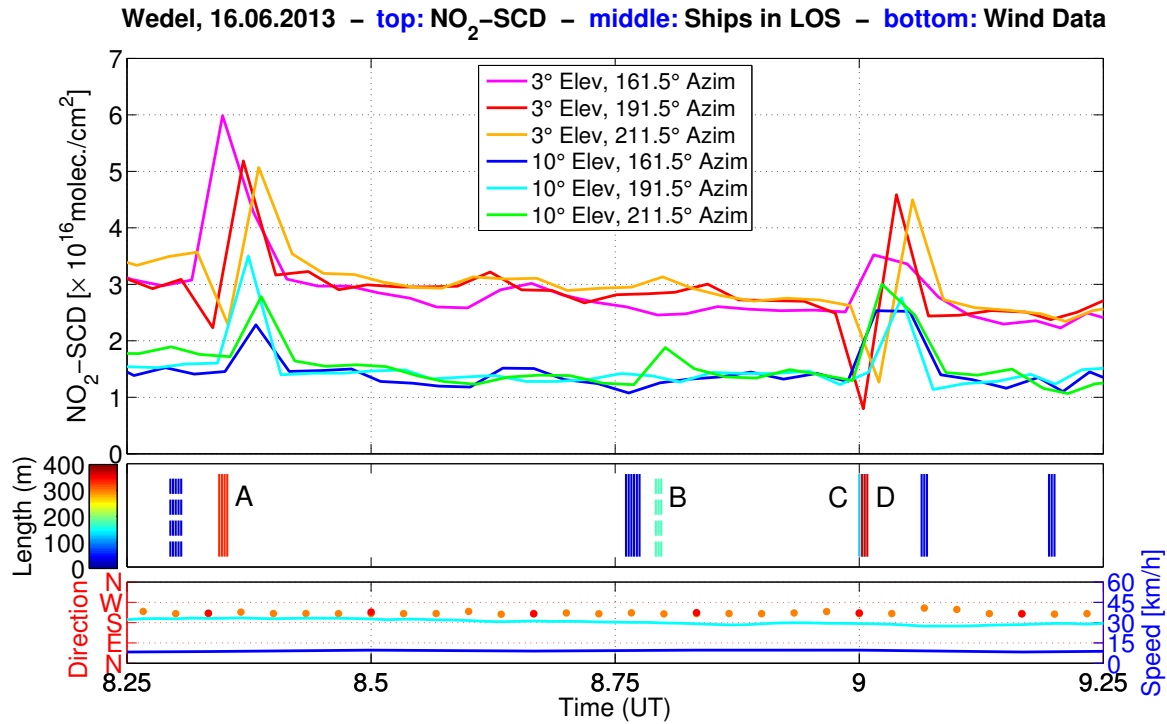
Table 11.1.: AIS information for large ships A,B,C and D in Figure 11.10

ID	Name	Length [m]	Speed [kn]	Type	MMSI	IMO
A	EVER LIVEN	335	11.0	Container	416481000	9595527
B	JONNI RITSCHER	178	11.5	Container	636091136	9333383
C	AURORA	134	13.6	Container	209627000	9234989
D	COSCO DEVELOPMENT	366	10.4	Container	477950300	9472139

In the 3° elevation angle horizontal scan it is clearly visible that the two big ships are coming from the left (east) and going to the right (west), since the peaks first appear at 161.5° azimuth, then at 191.5° and after that at 211.5°. This means, that the ships are coming out of the Port of Hamburg. If the second large peak at 9:00 UT is coming from ship C (AURORA) or D (COSCO DEVELOPMENT) or both is not clear. A look into a map with the plotted AIS ship position data (see Figure 11.11 shows that both ships passed the instrument side-by-side.
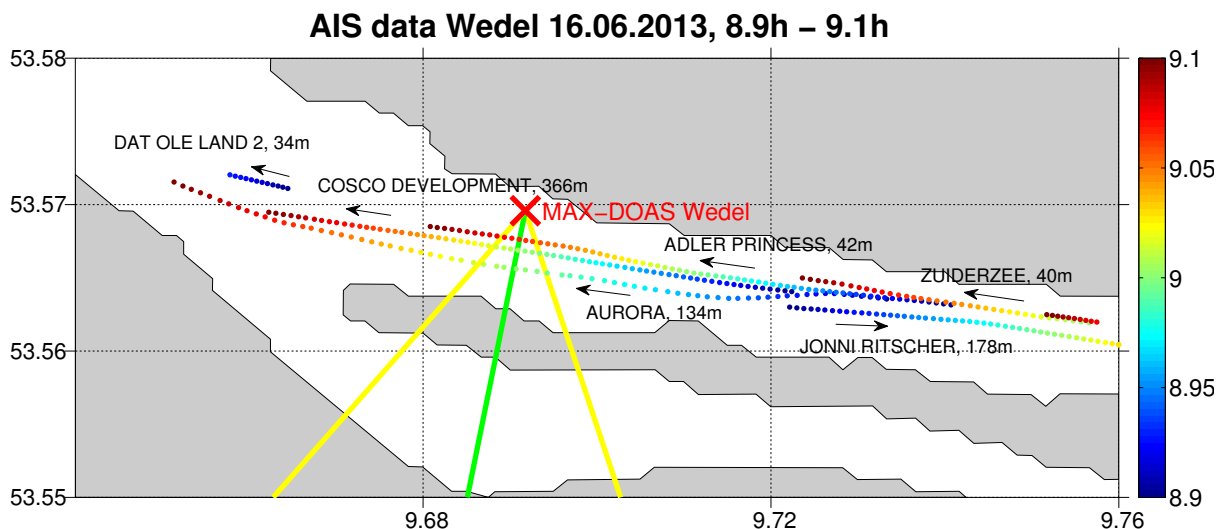
Figure 11.11.: Map with AIS ship position data for Wedel on Sunday, 16 June 2013 around 9:00 UT. The time is color-coded according to the color-scale on the right. The black arrows show the movement directions of the ships.

11.4. NO$_2$/SO$_2$ Ratios

To determine the relative emission rates of NO$_2$ and SO$_2$, the NO$_2$/SO$_2$ ratio can be calculated. Measurements of NO$_2$/SO$_2$ in different plumes makes it then possible to compare the emissions of different ships. By measuring these ratios over a longer time period, also future changes due to further regulations can be monitored (McLaren et al., 2012).

For the MAX-DOAS measurements presented in this thesis this has been done by dividing the UV NO$_2$-SCD by the SO$_2$-SCD, which is also measured in the UV. The difference of the light paths due to the slightly different fitting windows introduces an uncertainty that in the following is neglected.

For the Wedel station, such ratios for a selection of seven ships on two different days are shown in Figures 11.12 and 11.13. The value for the quotient NO$_2$/SO$_2$ is denoted next to the peaks.

As can be seen from these figures, the NO$_2$/SO$_2$ ratios measured in the selected time periods range between 0.09 ($\approx$ ten times more SO$_2$ than NO$_2$) for the 155 m-ship FREDERIK built in 2005 and 1.23 (slightly more NO$_2$ than SO$_2$) for the 332 m-ship MAERSK TAURUS built in 2008, which uses scrubber technology to reduce SO$_2$ emissions.

Most of the measured ratios are in the range from 0.26 to 0.65 and are thereby one order of magnitude smaller than those measured on Neuwerk (see Chapter 12.4). Also the values in other studies of shipping emissions are considerable higher: McLaren et al. (2012) measured a mean ratio of 2.86 (single measurements range between 0.77 and 5.64) during nighttime by DOAS in the Strait of Georgia, about 2 to 3 km away from the shipping lane.

Dividing the emission factors of NO$_2$ and SO2 published by Diesch et al. (2013) for in-situ measurements on the bank of the river Elbe downstream from Wedel, gives numbers of 7.8 (ships $<$ 5000 t), 4.1 (5000 to 30 000 t) and 3.6 (ships $>$ 30 000 t).

Wedel, 17.05.2013 – top: SO$_2$–SCD – middle: Ships in LOS – bottom: Wind Data
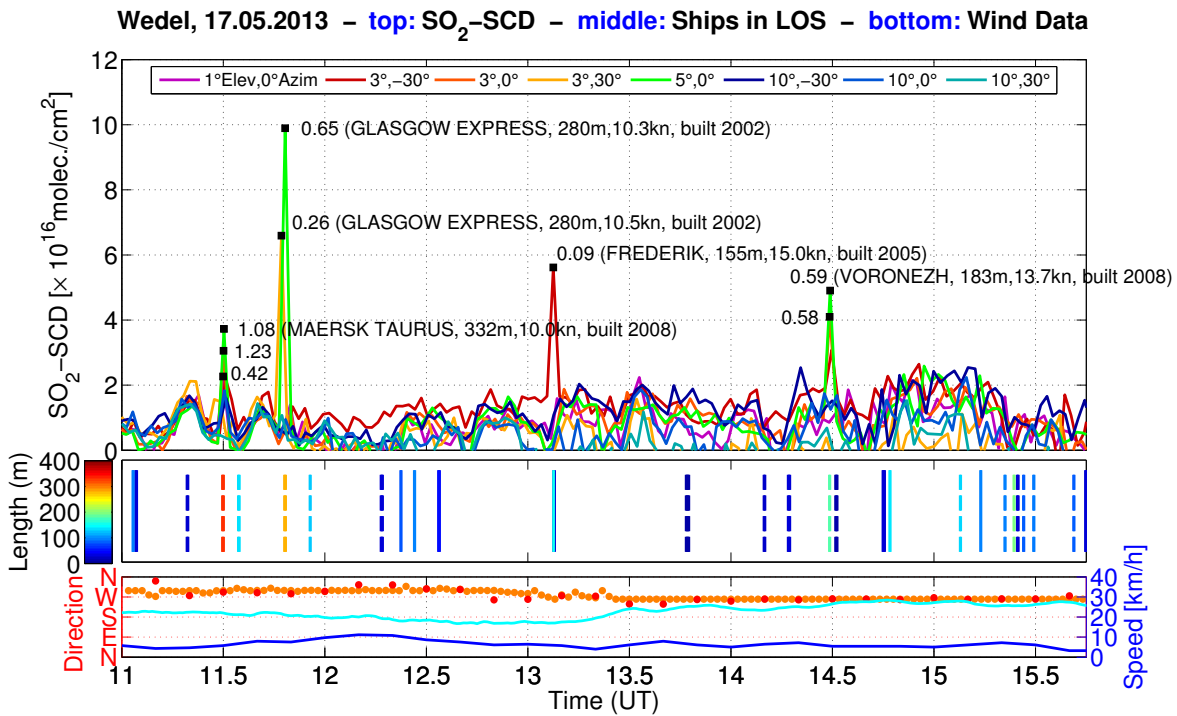
Figure 11.12.: SO$_2$-SCD, AIS, wind data and NO$_2$/SO$_2$ ratios for Wedel on Friday, 17 May 2013.
On top: MAX-DOAS SO$_2$-SCDs in various viewing directions, the numbers close to the peaks denote the NO$_2$/SO$_2$ ratio
In the middle: bars indicating that a ship is in the line-of-sight, solid bars: ship moves from left to right (east to west), dashed vice versa, colors representing ship length
On the bottom: wind speed and direction from Finkenwerder (blue and red) and Brokdorf (cyan and orange)

Wedel, 20.07.2013 – top: SO$_2$–SCD – middle: Ships in LOS – bottom: Wind Data

Figure 11.13.: SO$_2$-SCD, AIS, wind data and NO$_2$/SO$_2$ ratios for Wedel on Saturday, 20 July 2013.

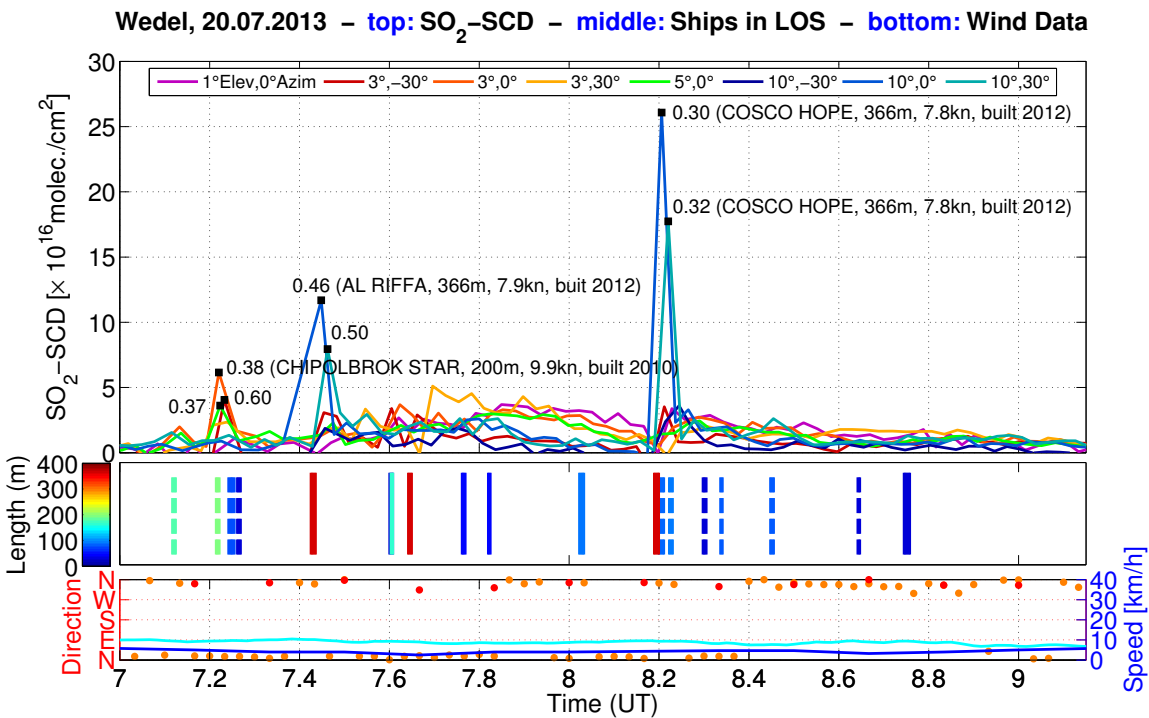This large deviation suggests the assumption that in Wedel the MAX-DOAS instrument measures through the fresh, just exhausted plumes, in which most of the NO_x is still in the form of NO and had no time to be converted to NO_2. The fact, that for a lot of multiple measured ship plumes the measured NO_2/SO_2 ratio increases with time, supports this assumption.
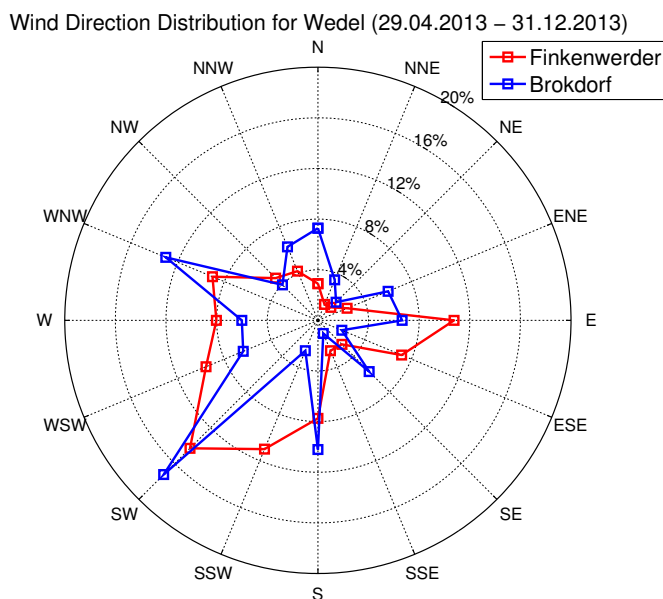
11.5. Wind Direction Dependence

Figure 11.14.: Azimuthal distribution of wind directions measured at two weather stations in Brokdorf and Finkenwerder, located downstream and upstream of Wedel

In Figure 11.14 the azimuthal distribution of the measured wind direction for Wedel with data from two different weather stations is shown. The first station is located in Hamburg-Finkenwerder, approximately 10 km upstream of Wedel, near to the factory premises of Airbus. The second station is located in Brokdorf, a small town 40 km downstream the river Elbe. Comparing the wind direction distributions measured at both stations, one can see that there is a rough agreement in the general pattern, with more frequent westerly and southerly winds. By looking closer at the different wind directions, significant differences in the frequencies can be seen. This is not astonishing, since the distance between both stations is quite large (50 km) and also their immediate surrounding is not similar. Brokdorf is near to the North Sea coast and experiences much higher wind speeds, the Finkenwerder station is located at the edge of a residential area. Despite these differences in the overall pattern, the progressions of the wind direction curves for single days agree very well, as can be seen later.

Having reliable wind data is very important for the determination of the appropriate sources for the measured peaks of air pollution, especially for the in-situ measurements, but in Wedel also for the background pollution in MAX-DOAS measurements.

With the help of this wind data, it is possible to assign the measured slant column densities (SCDs) of the investigated trace gases to the corresponding wind directions. Averaging over all measurements containing ship emission peaks as well as background values delivers a view of the mean azimuthal distribution of the air pollution, like it is shown in Figure 11.15.
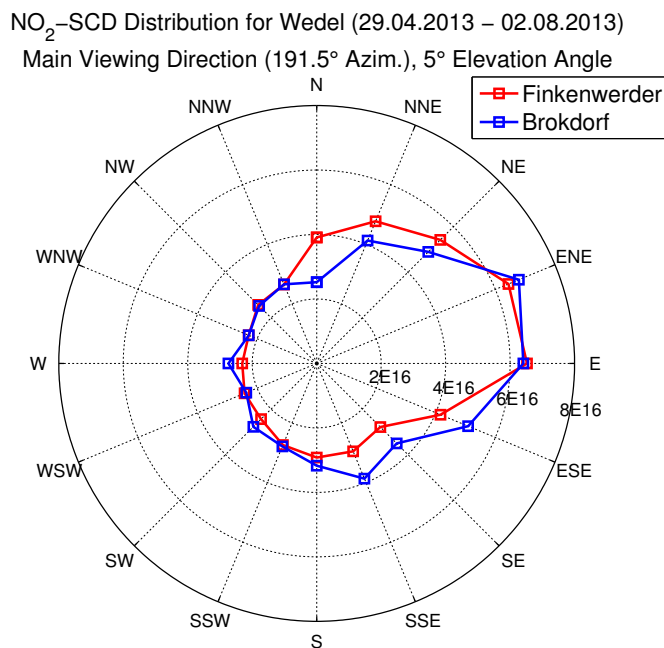
NO$_2$–SCD Distribution for Wedel (29.04.2013 – 02.08.2013)

Main Viewing Direction (191.5° Azim.), 5° Elevation Angle

Figure 11.15.: Wind direction dependence of NO$_2$ slant column densities measured in Wedel. Shown is the mean SCD measured in the main azimuth viewing direction (191.5°) at 5° elevation angle, using wind direction data from Brokdorf (blue) and Finkenwerder (red).

In spite of the distinct wind direction distributions for both stations, the wind direction dependence of the measured NO$_2$-SCDs looks very similar. High values of NO$_2$ are mostly coming from east and northeast directions. Comparing this plot with an underlying map of the region (see Figure 11.16) confirms, that these are most likely high background pollution values coming from Wedel as well as the city of Hamburg.

Using the geometric approximation (see Chapter 6.7), volume mixing ratios of NO$_2$ can be calculated and then be compared to the in-situ measurements. Such a comparison is shown in Figure 11.17. For most wind directions, the VMRs agree quite well. However, for south-easterly directions, there is a maximum difference of about 4 ppb. This deviation could be explained by the ship emission peaks, which are much higher in the in-situ measurements, because the MAX-DOAS measurements represent an average over a long light path.
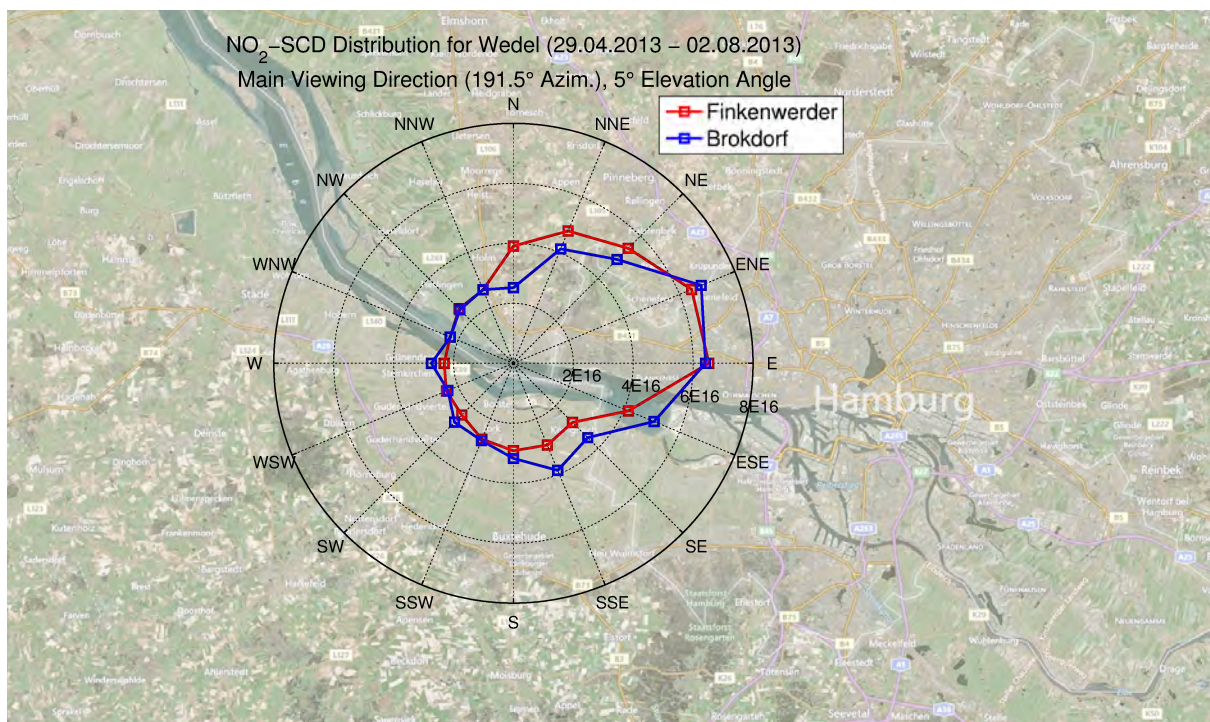
Figure 11.16.: Wind direction dependence of NO_2 slant column densities measured in Wedel with underlying map of the region [Image source: `http://www.bing.com/maps/` (01.04.2014)]
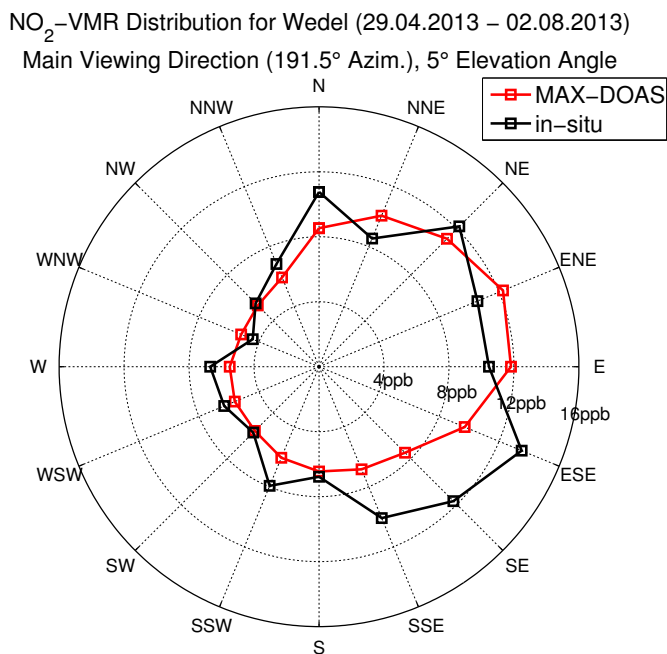
Figure 11.17.: Wind direction dependence of NO_2 volume mixing ratios measured with the MAX-DOAS (red) as well as the in-situ device (black) in Wedel. The MAX-DOAS VMRs were calculated using the geometric approximation with an assumed mixing layer height of 175 m. For both curves wind data from Finkenwerder was used.

11.6. Long-Term Time Series

A comparison of three-week time series of measured MAX-DOAS and in-situ NO_2 volume mixing ratios can be seen in Figure 11.18. Both time series show a consistent behavior and agree very well for almost all displayed days.

Figure 11.18.: Comparison of MAX-DOAS NO_2-VMR and in-situ NO_2-VMR time series. The MAX-DOAS VMRs (main viewing direction, 5° elevation angle) were calculated using the geometric approximation assuming a mixing layer height of 250m.

12. Measurement Results for Neuwerk

This chapter presents the measurement results for the Neuwerk station. The fitting parameter for the MAX-DOAS measurements can be found in the appendix.
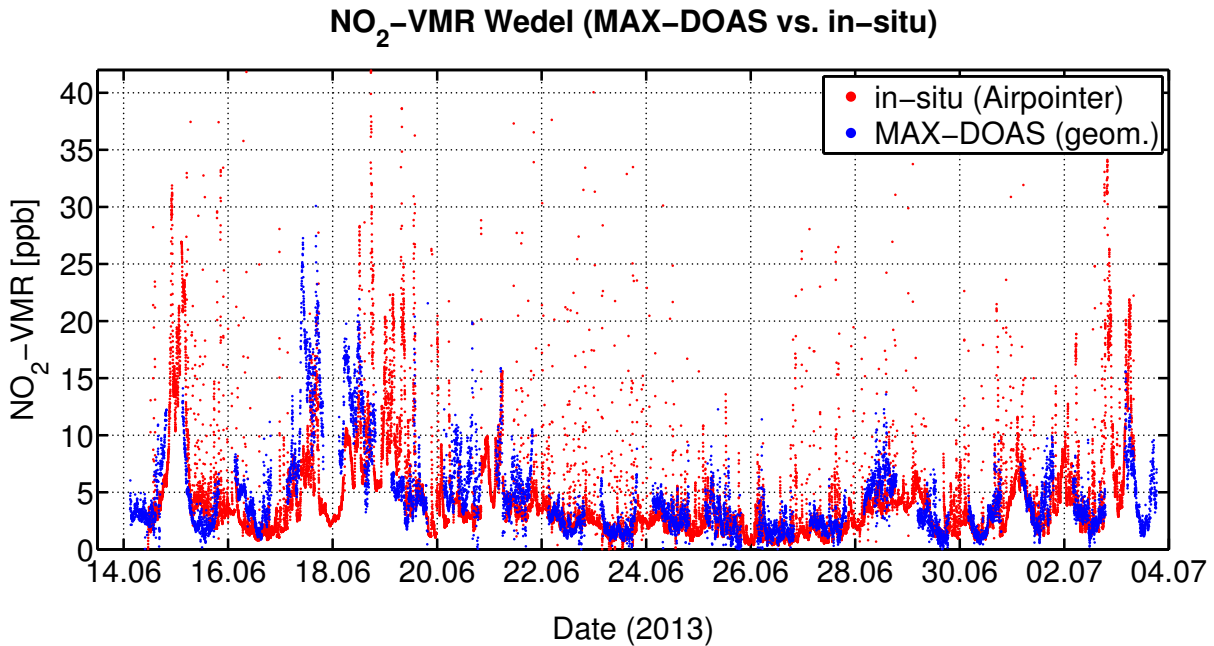
12.1. Suitability of the Neuwerk Station

Figure 12.1 shows a map with all received AIS ship position messages and the color-coded shiplength for the two-month time period from 08.07.2013 until 09.09.2013. This plot illustrates how close the main shipping lane runs along the islands Neuwerk and Scharhörn. The chosen MAX-DOAS viewing directions point directly towards the shipping lane and the different viewing azimuth angles cover a high extend of the region. This emphasizes that, despite the larger distance to the emitting ships compared to the Wedel station, the radar tower Neuwerk is a suitable station, providing also the possibility to study the horizontal distribution of the emitted trace gases.
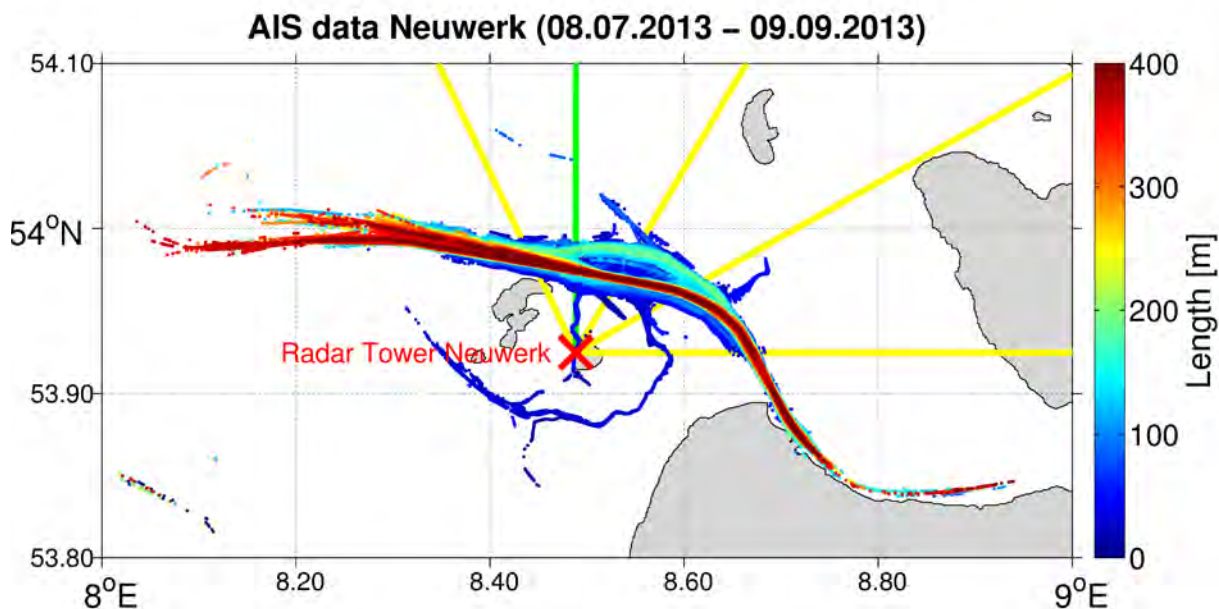
Figure 12.1.: Two-month overview of the AIS ship position data measured on Neuwerk. The ship length is color-coded according to the color scale on the right.

It can also be seen from this map, that the shipping lane in the mouth of the river Elbe near Cuxhaven is very narrow and runs very close to the left bank. In the north of Neuwerk, the very large ships ($>300\,\mathrm{m}$) follow a narrow shipping channel, smaller ships also use alternative waterways. The map shows also that the larger the ship, the longer the AIS signal is received due to the higher and larger antenna.

12.2. Single-Day Measurements

Figure 12.2 shows typical MAX-DOAS NO_2 and SO_2 slant column measurements (Figure 12.2a) as well as typical in-situ NO_2 and SO_2 volume mixing ratio measurements (Figure 12.2b).

There are clearly visible differences compared to the measurements in Wedel. First, for both instruments the measured peaks are much broader and seem to be blurred out. Especially for the in-situ measurements this is always the case and can be explained by spreading and dispersion of the ship plumes on the much longer distance. For the MAX-DOAS measurements the width of the peaks is also broader, but seems to depend on the wind direction, as is discussed later.

Another striking difference is that the dynamic between background values and emission peaks looks similar for both instruments. The progression of the measured trace gas abundances looks consistent and the peaks seem to be approximately at the same times.

(a) MAX-DOAS NO_2 and SO_2 SCD
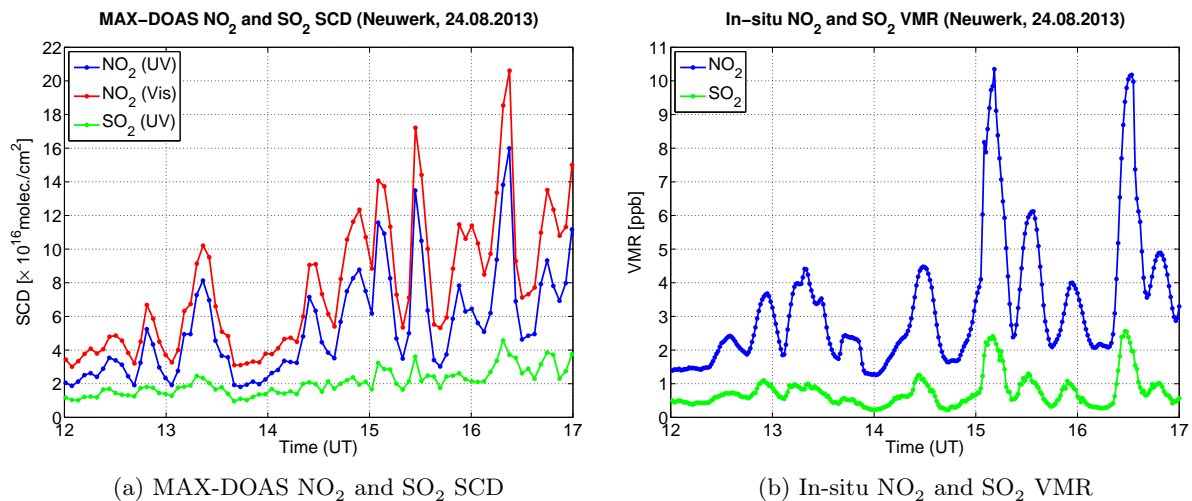
(b) In-situ NO_2 and SO_2 VMR

Figure 12.2.: MAX-DOAS SCD (0° elevation, 0° azimuth) and in-situ VMR measured on Neuwerk on Saturday, 24 August 2013

Two other sample-days are shown in Figures 12.3aa,b and 12.4aa,b. Both show characteristics similar to those stated above.

The simple geometric approximation described in chapter 6.7 is, except for the dependency on air temperature and pressure, simply something like a scaling factor. Comparing the SCD and VMR plots for the different days provides an indication that this approach could work quite well for the single days taken alone. But comparing Figures 12.2,12.3 and 12.4 particularly with regard to the y-axis limits in the MAX-DOAS and in-situ plots, already reveals that this method could not work for a longer time series. On 24 August 2013 (Figure 12.2) a scaling factor of approximately 2×10^{16} would be needed to get similar background values, on 14 August 2013 (Figure 12.3), however, the scaling factor is in the range of 3×10^{16} to 5×10^{16} and on 28 August 2013 (Figure 12.3) about 1×10^{16}. These differences can not be explained by the slight changes in the measured air pressure and temperature.

According to Chapter 6.8, the O_4 and H_2O slant column densities, which are measured simultaneously to the NO_2 and SO_2 slant columns, can be used as a proxy for the effective light path to calculate volume mixing ratios. This approach is especially feasible on Neuwerk, since for the Neuwerk data the 0° elevation angle shows the highest SCDs as well as the highest dynamic and is therefore the most beneficial viewing

(a) MAX-DOAS NO$_2$ and SO$_2$ SCD

(b) In-situ NO$_2$ and SO$_2$ VMR
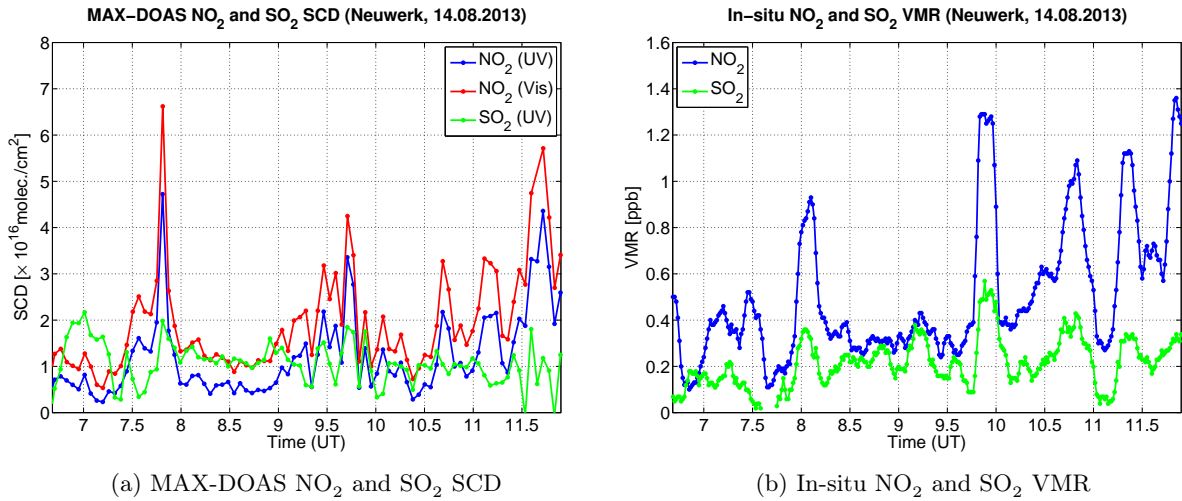
Figure 12.3.: MAX-DOAS SCD (0° elevation, 0° azimuth) and in-situ VMR measured on Neuwerk on Wednesday, 14 August 2013

(a) MAX-DOAS NO$_2$ and SO$_2$ SCD
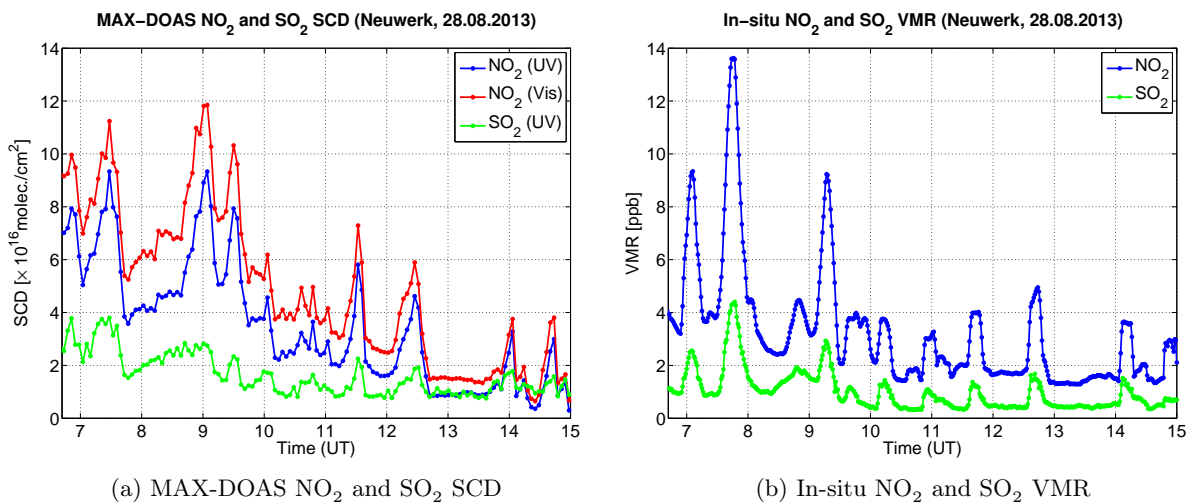

(b) In-situ NO$_2$ and SO$_2$ VMR

Figure 12.4.: MAX-DOAS SCD (0° elevation, 0° azimuth) and in-situ VMR measured on Neuwerk on Wednesday, 28 August 2013

angle for this measurement site. This is also due to the altitude of about 30 m, in which the MAX-DOAS instrument is located on the radar tower. In Wedel, on the contrary, the most useful elevation angles are 5° and 10°, as described above, making this approach inapplicable without further assumptions on O_4 and H_2O profiles.

Figure 12.5 shows these approaches applied to the measurements on Saturday, 24 August 2013 (SCDs see Figure 12.2a) and for comparison, in Figure 12.6 the geometric approach can be seen. In both plots also the in-situ values are included.
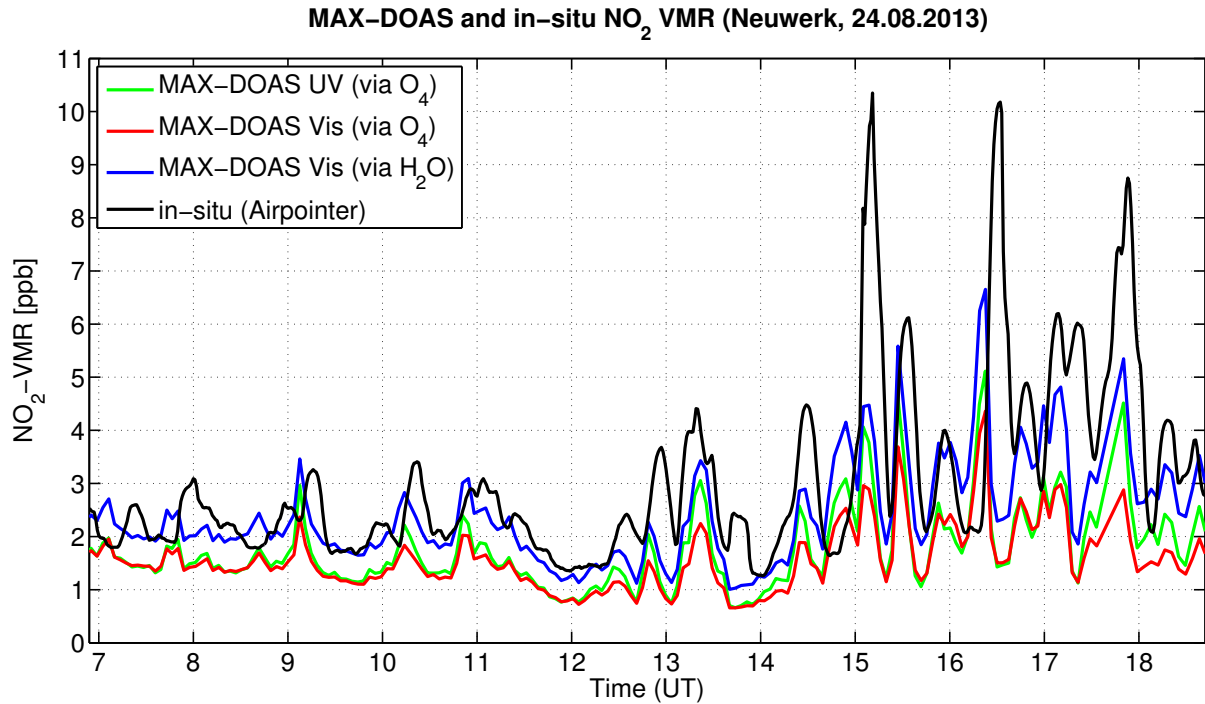

Figure 12.5.: Comparison of MAX-DOAS and in-situ NO_2 volume mixing ratios measured on Neuwerk on Saturday, 24 August 2013. The MAX-DOAS VMRs (0° elevation, 0° azimuth) were calculated using O_4 and H_2O as a light path tracer.

One advantage of this method over the simple geometric approximation is that the different light path lengths for UV and visible light are compensated by using the SCD of a trace gas with well-known concentrations as a tracer. This is clearly visible for the UV and visible VMRs calculated via O_4, which agree very well. Regarding the background pollution values, the VMRs calculated using the water vapor slant column density show the best agreement with the in-situ measurements for this day, but also for a lot of other days that are not shown here. However, often the MAX-DOAS VMRs via H_2O are slightly lower than the in-situ values, seen also in the long-term time-series analysis later. Indeed, a small offset of the in-situ measurements cannot be ruled out.

A similar approach can be used to calculate the SO_2 volume mixing ratios. Since SO_2 is measured in the UV spectral range, only the UV O_4 slant column density can be used to estimate the light path. In Figure these values can be compared to those from the geometric approximation, showing that a slightly better agreement between MAX-DOAS and in-situ values is achieved by using the O_4-SCD.

MAX–DOAS and in–situ NO$_2$ VMR (Neuwerk, 24.08.2013)

Figure 12.6.: Comparison of MAX-DOAS and in-situ NO$_2$ volume mixing ratios measured on Neuwerk on Saturday, 24 August 2013. The MAX-DOAS VMRs (1° elevation, 0° azimuth) were calculated using the geometric approach with an assumed mixing layer height of 150 m.
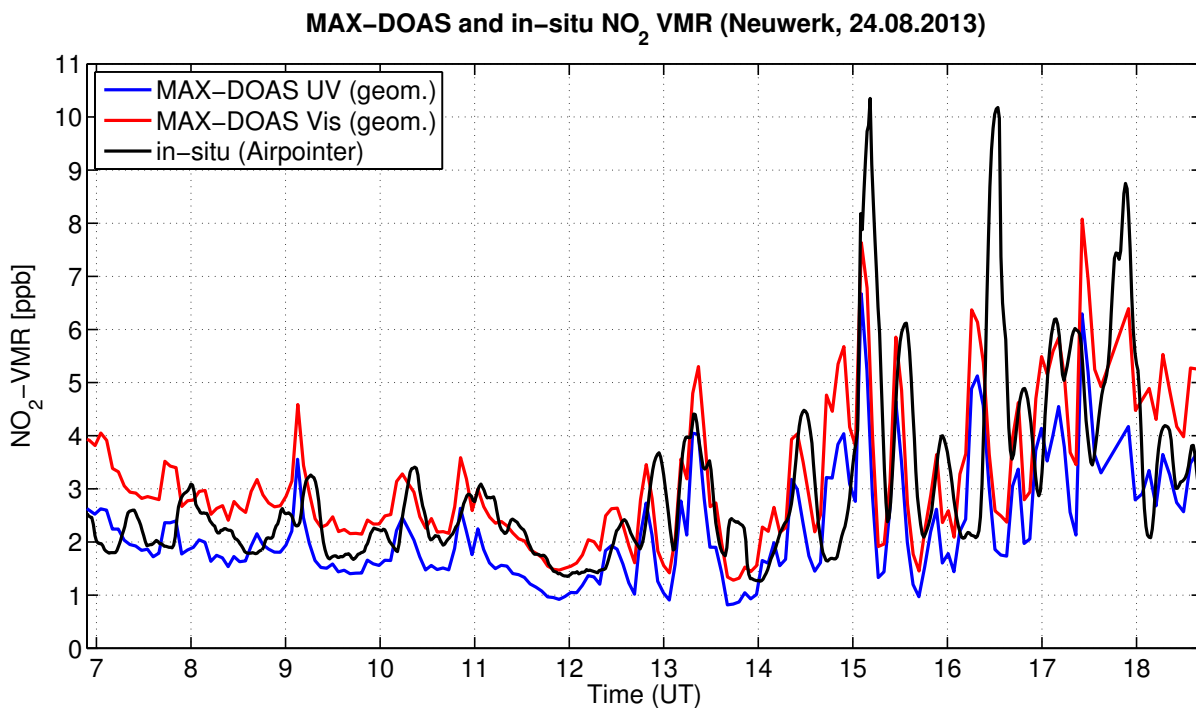
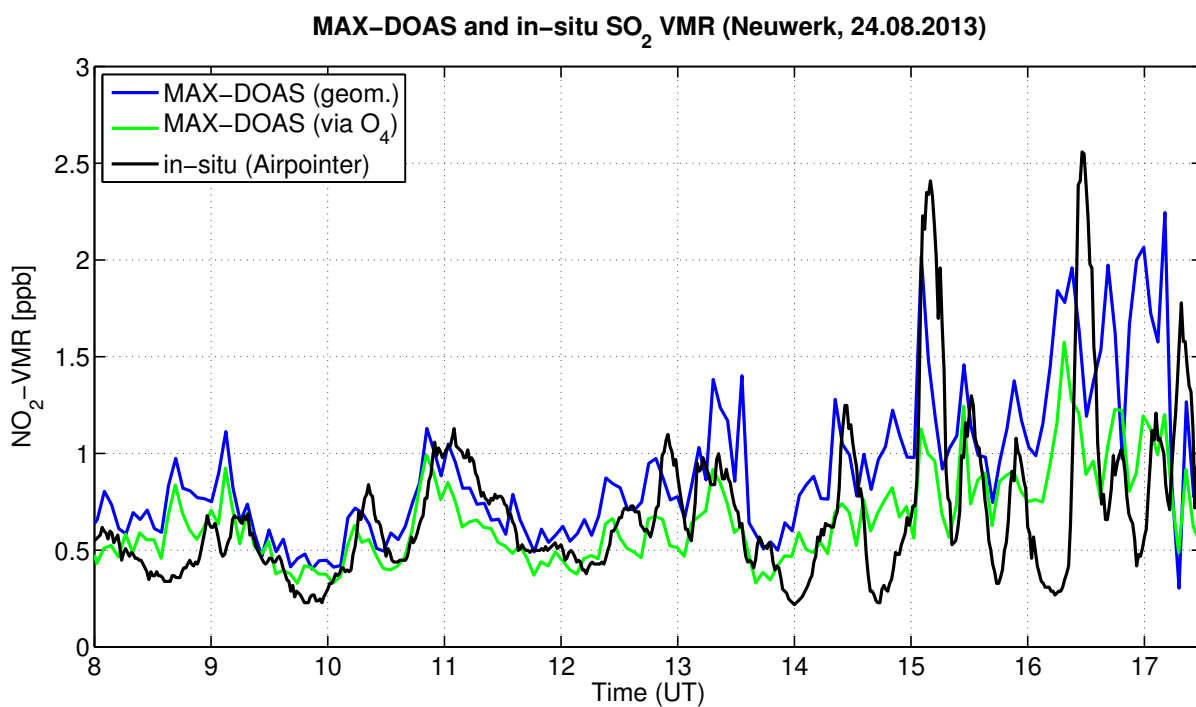**MAX–DOAS and in–situ SO$_2$ VMR (Neuwerk, 24.08.2013)**

Figure 12.7.: Comparison of MAX-DOAS and in-situ SO$_2$ volume mixing ratios measured on Neuwerk on Saturday, 24 August 2013. MAX-DOAS geometric VMRs for 1° elevation, 0° azimuth, 150 m mixing layer height in blue and via O$_4$ (0° elevation, 0° azimuth) in green.

12.3. Allocation to Ships

Like in Wedel, at the Neuwerk station also AIS (*Automatic Identification System*) ship data and weather data are collected. Additional wind speed and direction measurements are availabe for Neuwerk and the neighboring island Scharhörn, measured by the Hamburg Port Authoriy (HPA). This data will be used in the following to allocate the measured emission peaks to the emitting ships. To achieve this, plots combining MAX-DOAS and in-situ VMRs with AIS and wind data, like those seen in Chapter 11.3 for Wedel, are used (for a detailed description, see there).

The first example in Figure 12.8 shows MAX-DOAS and in-situ NO_2 volume mixing ratios measured on Wednesday, 10 July 2013. On this day, the wind was coming from the northwest, directly from the shipping lane. Correspondingly, the absolute values measured on this day are low, ranging up to 2 ppb at maximum. The background values for both instruments are substantially smaller than 1 ppb, but show some deviations especially in the morning. However, especially the in-situ data is very noisy and the measured values are close to the detection limit of 0.4 ppb for NO_2, specified for the Airpointer instrument (see Chapter 7.2).
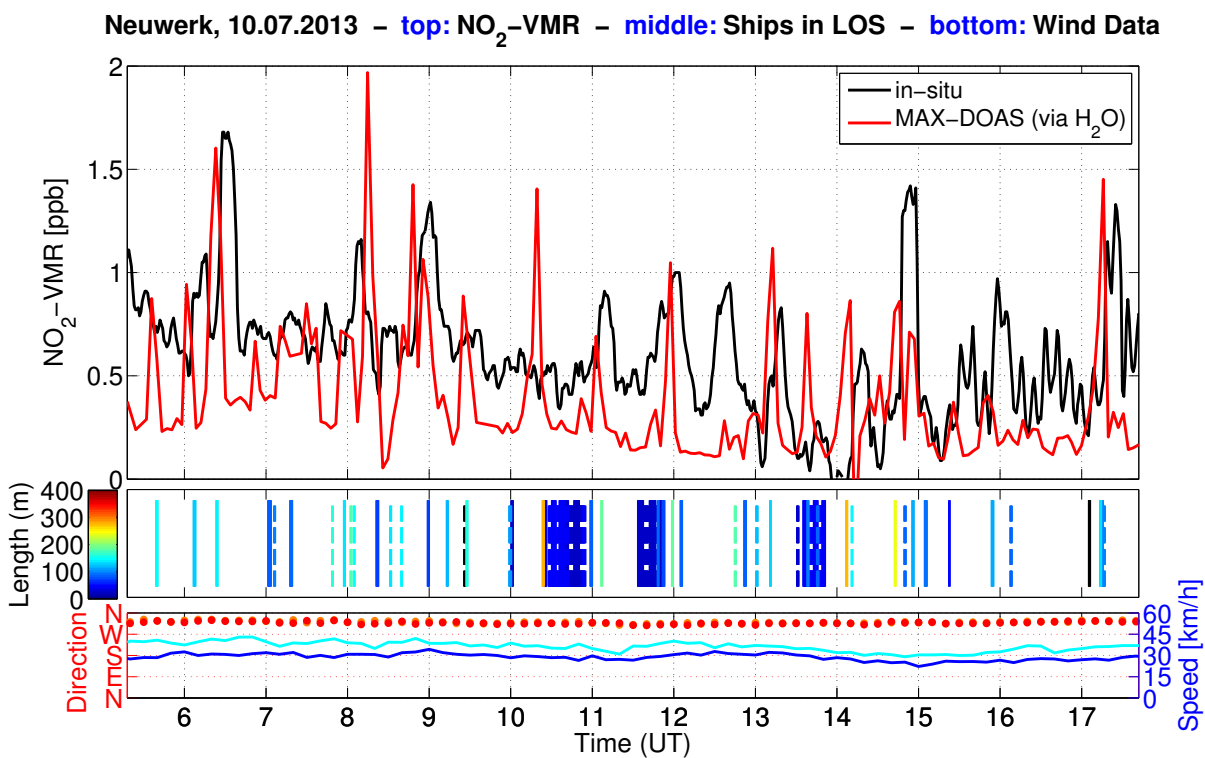
Figure 12.8.: VMR, AIS and wind data for Neuwerk on Wednesday, 10 July 2013.
  On top: in-situ and MAX-DOAS NO_2-VMRs (0° elevation, 0° azimuth)
  In the middle: bars indicating that a ship is in the line-of-sight, solid bars: moves from left to right (west to east), dashed vice versa, colors representing ship length
  On the bottom: wind speed and direction from Neuwerk (blue and red) and Scharhörn (cyan and orange)

Comparing the measured peaks with the location of the vertical bars in the middle sub-figure, that indicate when a ship is in the line-of-sight of the MAX-DOAS instrument, reveals that for the MAX-DOAS measurements, almost all peaks can be allocated to single ships. In the in-situ measurements, the

peaks are broader, making it more difficult to assign them to certain ships.

It is also clearly visible, that often a time-shift between MAX-DOAS and in-situ peaks exists, with the in-situ peaks measured later. This can be explained by the long distance of about 6 km, that the plumes have to travel until they reach the radar tower. Hence, this time-shift should depend on the wind speed.

By looking on the MAX-DOAS measurements in detail, it can be seen that for ships that are coming from the west and go the east (from the left to the right), represented by the solid vertical bars, the peaks are measured slightly before the ship crosses the line of sight. This means that the northwest wind blows the exhausted plumes into the field of view of the MAX-DOAS instrument, before the ships reach the line-of-sight. The broad blue vertical bars in the middle plot indicate the times when the ferry Neuwerk – Cuxhaven (MS FLIPPER) and the small working and survey ships BAUMROENNE (WSA Cuxhaven) and NIGEWARK (HPA) move through the small shipping channel through the Wadden Sea to Neuwerk, that starts at the main shipping lane in the north and crosses the line-of-sight multiple times.

In the next plot in Figure 12.9 NO_2-VMRs as well as SO_2-VMRs are shown for Saturday, 24 August 2013. This day was shown already in Section 12.2 above, but will be analyzed in more detail in the following with the additional AIS and wind information.

Figure 12.9.: VMR, AIS and wind data for Neuwerk on Saturday, 24 August 2013.
On top: in-situ and MAX-DOAS NO_2 and SO_2 VMRs (0° elevation, 0° azimuth)
In the middle: bars indicating that a ship is in the line-of-sight, solid bars: moves from left to right (west to east), dashed vice versa, colors representing ship length
On the bottom: wind speed and direction from Neuwerk (blue and red) and Scharhörn (cyan and orange)

On this day, the wind was coming from the east the whole time. As discussed above, the peaks measured with the MAX-DOAS instrument are broader compared with Figure 12.8 and look blurred. The

background pollution values agree very well between both instruments for NO_2 as well as SO_2. The background is higher, with about $2\,ppb$ NO_2 and 0.5 to $1.0\,ppb$ SO_2. For this wind conditions, the allocation of peaks to single ships is difficult. When a lot of ships are passing Neuwerk shortly after each other, like in the evening, it is even more difficult. And it also looks like the westerly wind mixes and accumulates the emitted plumes along the main shipping lane, where sometimes the ships are moving like a rope of pearls. A correlation between the progression of the NO_2 curve and the SO_2 curve, especially for the large peaks, is clearly visible, although the SO_2 peaks are small compared to the NO_2 peaks.

Another day with wind from northwest is Friday, 19 July 2013. Figure 12.10 shows the measured NO_2 volume mixing ratios for the morning time. For this day, the peaks can easily be assigned to the passing ships. Especially the MAX-DOAS peaks are very sharp, each representing only a small number of enhanced measuements. For this day, the time shift between MAX-DOAS and in-situ peaks mentioned above is clearly observed for all peaks. Like in Figure 12.8 for Wednesday, 10 July 2013, the background values are very small, close to the detection limit of the in-situ device, but in contrast to the other day, show a very good agreement.
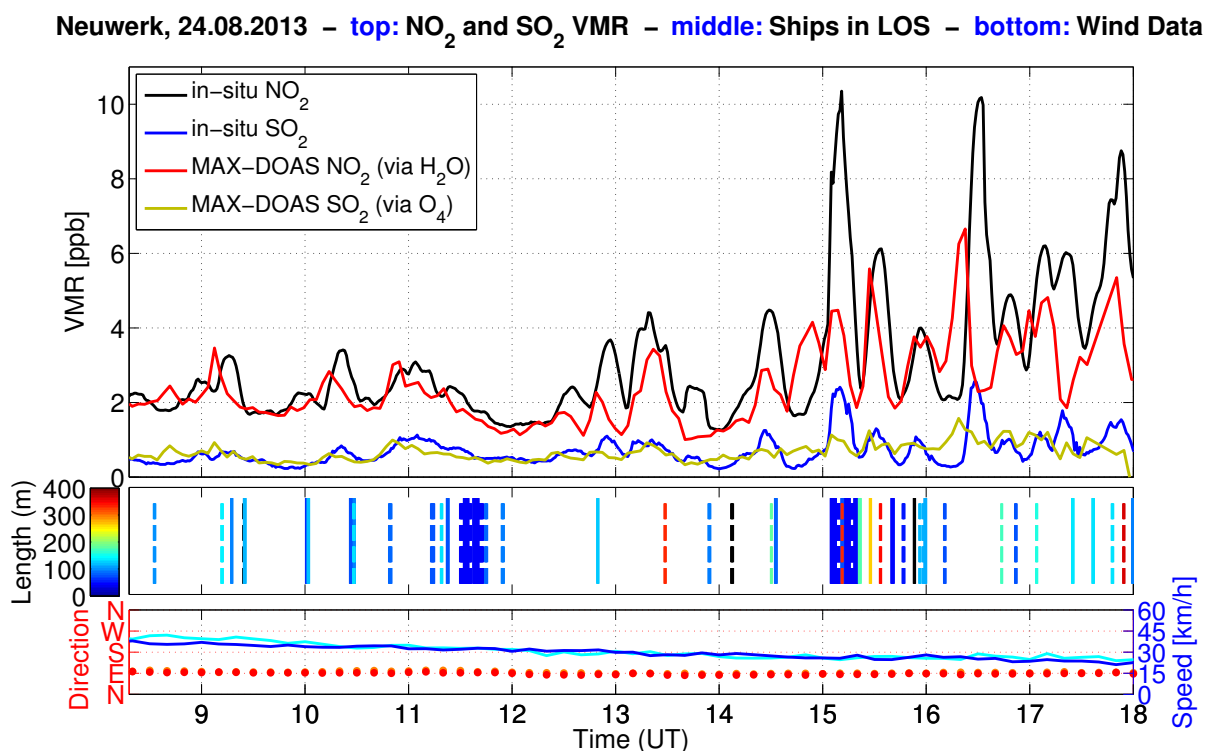

Figure 12.10.: VMR, AIS and wind data for Neuwerk on Friday, 19 July 2013.
  On top: in-situ and MAX-DOAS NO_2-VMRs (0° elevation, 0° azimuth)
  In the middle: bars indicating that a ship is in the line-of-sight, solid bars: moves from left to right (west to east), dashed vice versa, colors representing ship length
  On the bottom: wind speed and direction from Neuwerk (blue and red) and Scharhörn (cyan and orange)

Figure 12.11 displays a zoom into Figure 12.10 with various azimuth viewing directions plotted simultaneously. The evaluation of these horizontal scans illustrates and confirms that the ships A and G/H are moving from the left to the right of the field of view, because the corresponding peaks start to appear in the -25° azimuth direction, after that, successively the measured values in the 0°, 30° and 60° azimuth

angle are increasing. On the contrary, the peak around 10:00 UT, coming from ship B, starts to appear in the 60° azimuth direction. After that, enhanced values in 30°, 0° and -30° azimuth angle follow consecutively. This demonstrates that with the horizontal scans the MAX-DOAS instrument is able to identify the movement of ships and their emitted plumes.

Neuwerk, 19.07.2013 – top: NO$_2$–VMR – middle: Ships in LOS – bottom: Wind Data
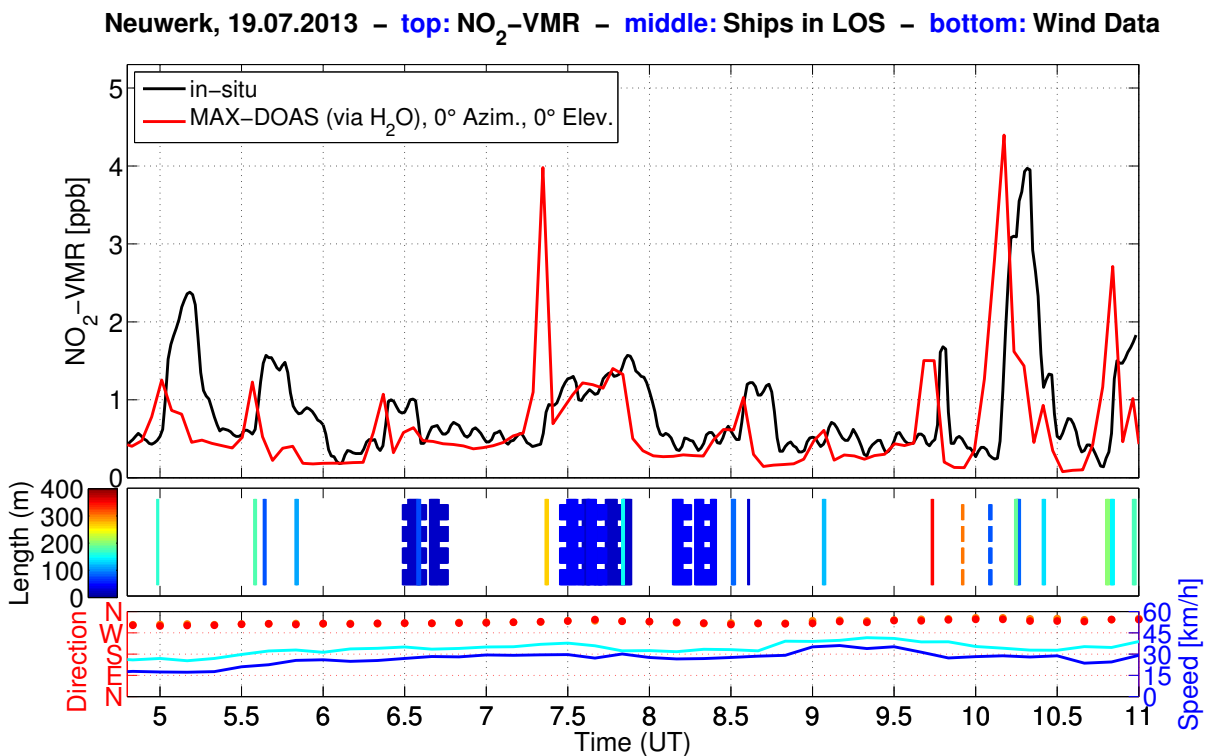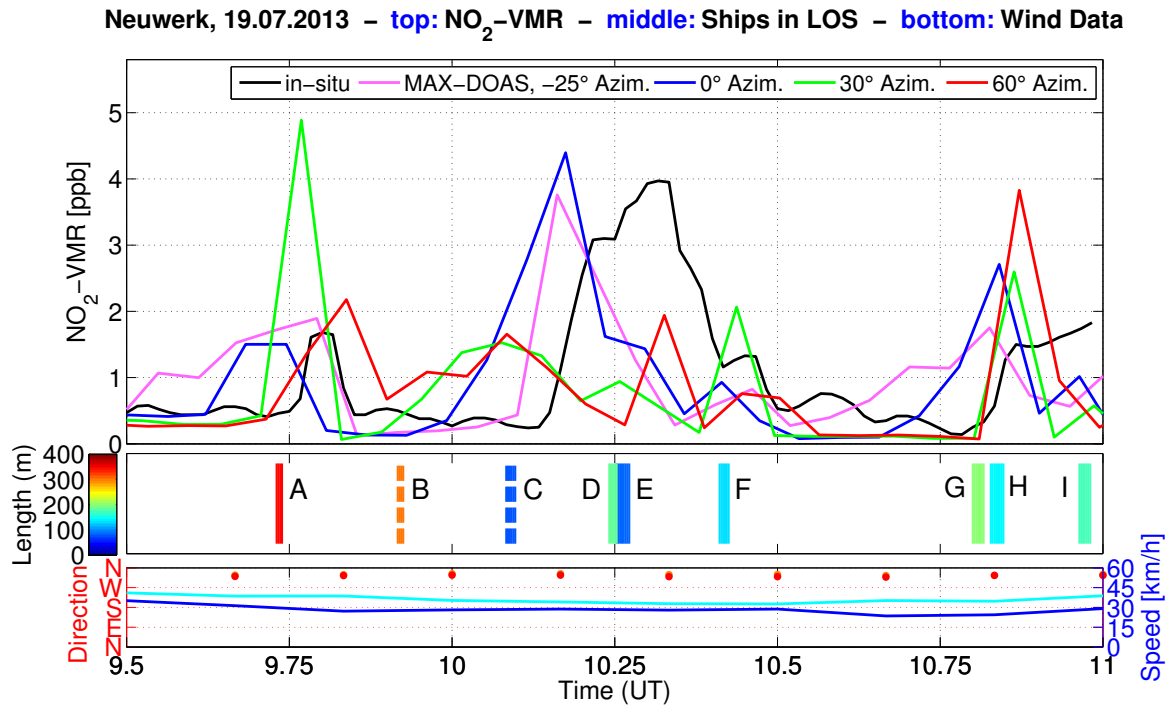
Figure 12.11.: VMR, AIS and wind data for Neuwerk on Monday, 12 August 2013.
On top: in-situ and MAX-DOAS NO$_2$-VMRs (0° elevation, 0° azimuth)
In the middle: bars indicating that a ship is in the line-of-sight, solid bars: moves from left to right (west to east), dashed vice versa, colors representing ship length
On the bottom: wind speed and direction from Neuwerk (blue and red) and Scharhörn (cyan and orange)

Table 12.1.: AIS information for all ships in Figure 12.11

ID	Name	Length [m]	Speed [kn]	Type	MMSI	IMO
A	APL QINGDAO	349	14.0	Container	566408000	9461893
B	MSC BARBARA	304	19.0	Container	353775000	9226932
C	YARA EMBLA	83	13.3	CO2 Tanker	257082000	9279446
D	RIO SAO FRANCISCO	190	15.6	Container	636091467	9339868
E	FRI LANGESUND	90	9.6	Cargo	236111779	9135743
F	TINA	138	13.4	Container	244198000	9277383
G	HASSI MESSAOUD 2	205	12.5	LPG Tanker	636012379	9295581
H	BULK SUNSET	148	10.0	Cargo	636013786	9151395
I	SEASHARK	178	11.3	Oil Tanker	211135000	9298193

For the peaks due to ship A and G/H mentioned above, maps with plotted AIS ship position data can be found in Figures 12.12 and 12.13. The map for the first peak confirms, that this is the plume of ship A. Whether ship G or H or both are responsible for the other peak, cannot be resolved, since both ships

move very close to each other.
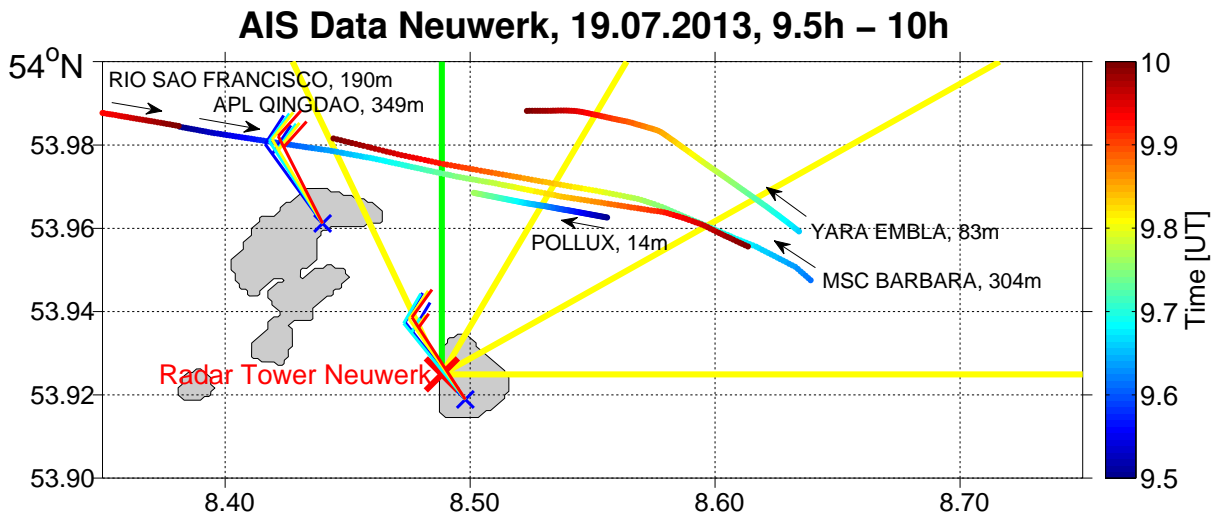
Figure 12.12.: Map with AIS ship position data for Neuwerk on Friday, 19 July 2013, 9:30–10:00 UT. The time is color-coded according to the color-scale on the right. The black arrows show the movement directions of the ships.
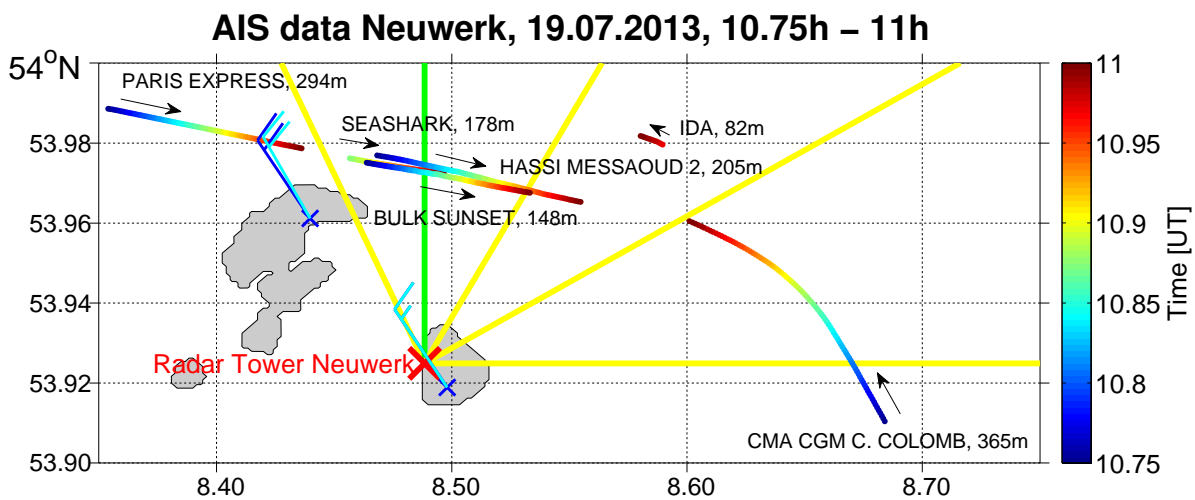
Figure 12.13.: Map with AIS ship position data for Neuwerk on Friday, 19 July 2013, 10:45–11:00 UT. The time is color-coded according to the color-scale on the right. The black arrows show the movement directions of the ships.

If the Wind on Neuwerk is coming from southerly directions, the ship plumes are blown away from Neuwerk. In such conditions, the in-situ device is not able to measure any ship emissions. The MAX-DOAS, however, can still measure the emissions, as it can be seen in Figure 12.14 for Monday, 12 August 2013.
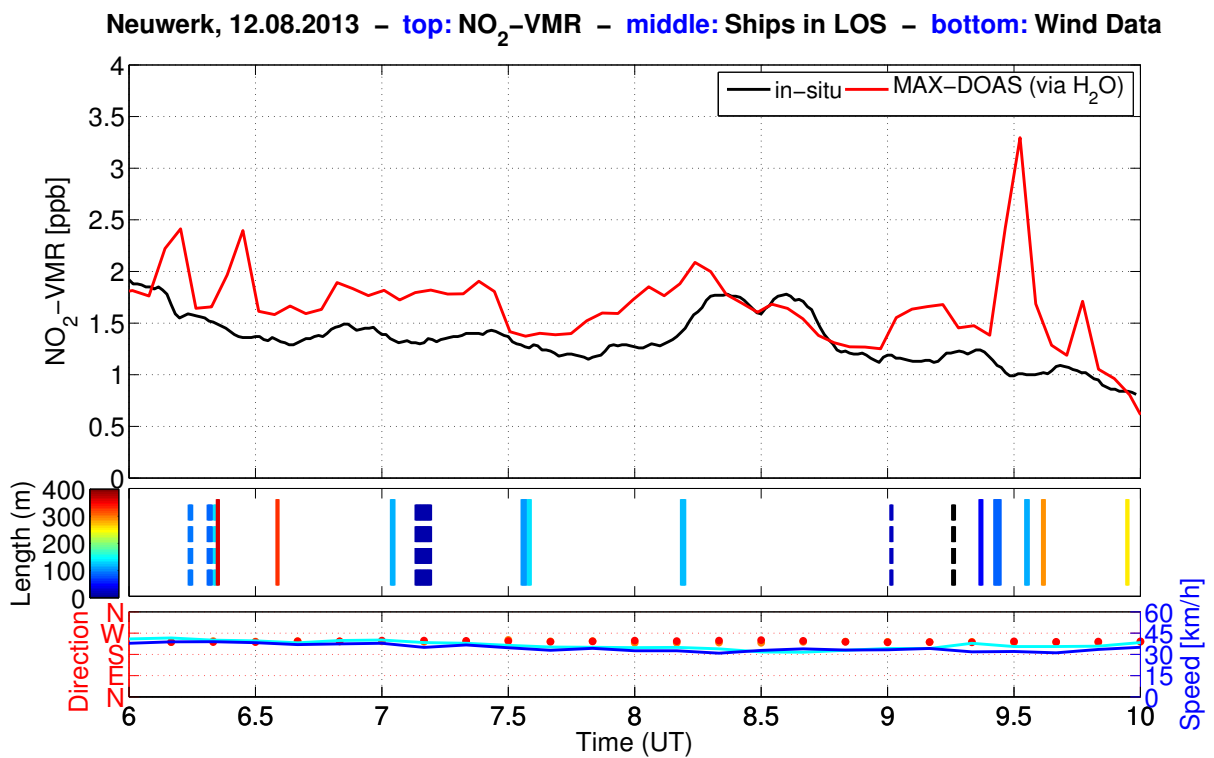
Figure 12.14.: VMR, AIS and wind data for Neuwerk on Friday, 19 July 2013.
  On top: in-situ and MAX-DOAS NO_2-VMRs (via H_2O, 0° elevation)
  In the middle: bars indicating that a ship is in the line-of-sight, solid bars: ship moves from left to right (west to east), dashed vice versa, colors representing ship length
  On the bottom: wind speed and direction from Neuwerk (blue and red) and Scharhörn (cyan and orange)

12.4. NO$_2$/SO$_2$ Ratios

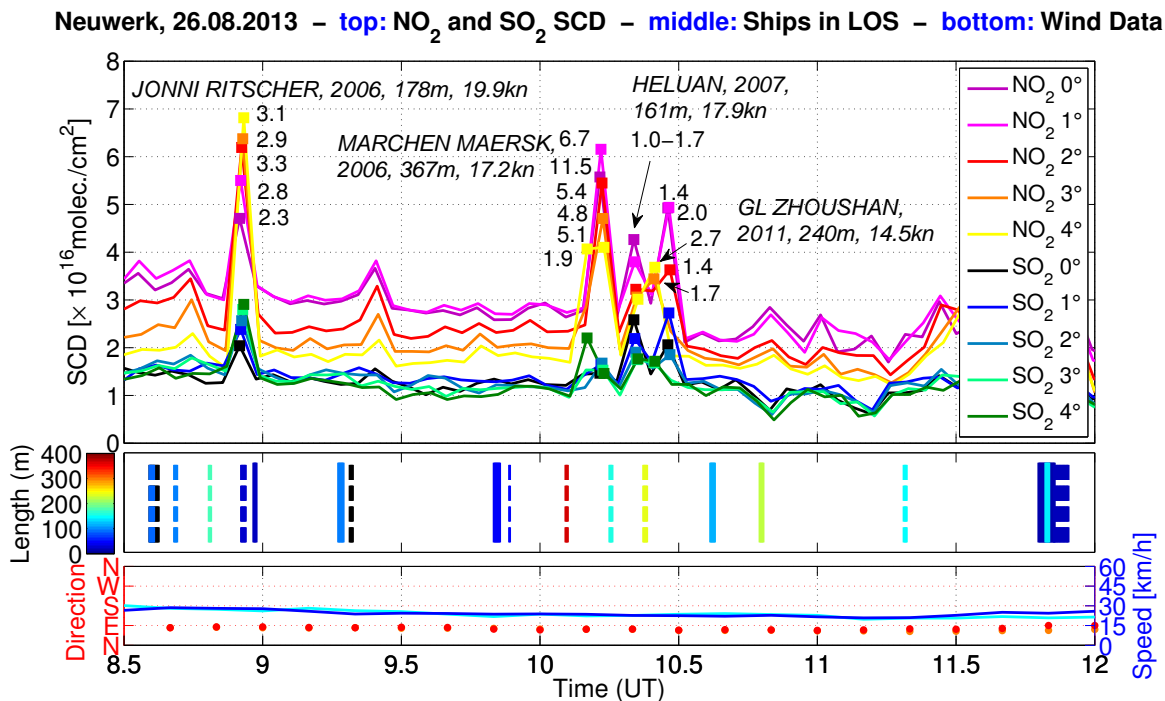A sample plot with calculated NO$_2$/SO$_2$ ratios for Neuwerk can be seen in Figure 12.15.

Figure 12.15.: NO$_2$ and SO$_2$ SCD, AIS and wind data as well as NO$_2$/SO$_2$ ratios for Neuwerk on Monday, 26 August 2013.
On top: MAX-DOAS NO$_2$ and SO$_2$ SCDs measured in vertical scans in the main viewing direction, the numbers close to the peaks denote the NO$_2$/SO$_2$ ratio
In the middle: bars indicating that a ship is in the line-of-sight, solid bars: moves from left to right (west to east), dashed vice versa, colors representing ship length
On the bottom: wind speed and direction from Neuwerk (blue and red) and Scharhörn (cyan and orange)

If we compare this ratios to those measured in Wedel (see Chapter 11.4), these values are approximately one order of magnitude larger and agree very well with the studies mentioned in Chapter 11.4: McLaren et al. (2012) measured a mean ratio of 2.86 (single measurements between 0.77 and 5.64). A range of 3.6 to 7.8 depending on ship size can be derived from Diesch et al. (2013).

This confirms the suggestion that the substantially lower ratios measured in Wedel are due to the short time interval between emission and measurement of the plumes, in which only very little amounts of NO had time to be converted to NO$_2$.

12.5. Wind Direction Dependence

Figure 12.16 shows the wind direction distribution measured at Neuwerk and the neighboring island Scharhörn, 6 km north west of Neuwerk. For both displayed time periods the two curves agree very well and show that wind is more frequently coming from the open North Sea (north-westerly to westerly to

south-westerly directions) as from the near coast. Also a seasonal difference can be seen, in summer more north-westerly wind directions were measured, in autumn more south-westerly directions.
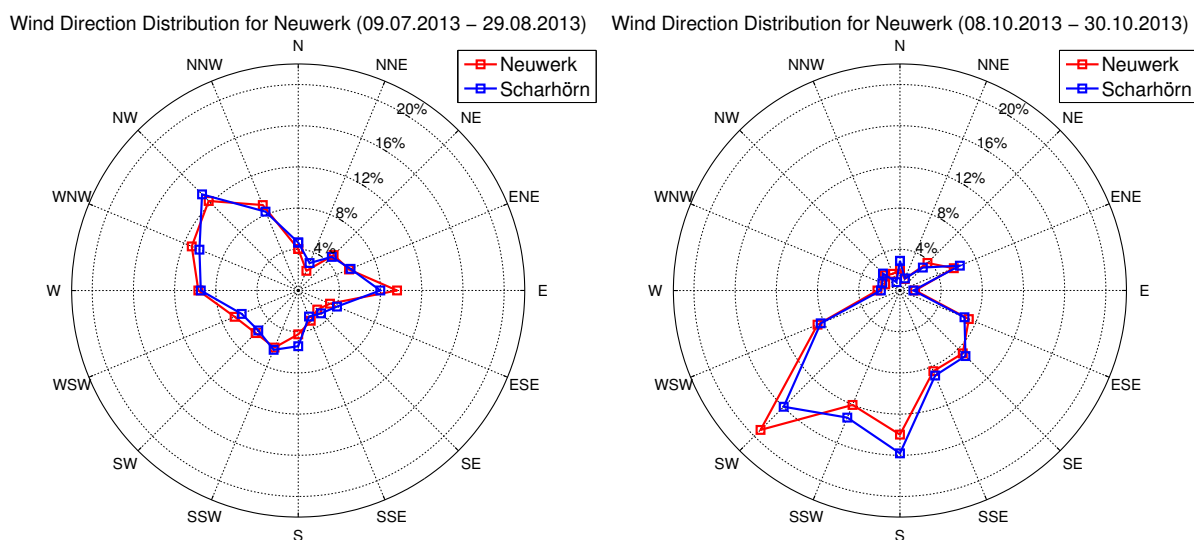

Figure 12.16.: Azimuthal distribution of wind directions measured at two weather stations on Neuwerk and the neighboring island Scharhörn for two different time periods: two months in summer (left) and three weeks in autumn (right)

From the agreement between both stations it follows that the azimuthal wind direction dependence of the measured NO_2 slant column density, shown in Figure 12.17 for both time periods, look very similar for both stations. As expected, the SCDs measured in the visible spectral range are consistently higher than those measured in the UV, due to the longer light path in the visible.

A comparison with a map of the surrounding area (see Figure 12.18) leads to the conclusion that, just like in Wedel, high values correspond to background air pollution, in this case coming from the coast, especially from the city of Cuxhaven with its industrial areas. But to some extend, those high values of NO_2 can also come from the main shipping lane into the river Elbe, which in the river mouth near Cuxhaven runs very close to the bank, as can be seen in Figure 12.1.

In Figure 12.19 the SO_2 slant column density for the first time period (in summer) can be seen. This azimuthal distribution shows the highest values for wind coming from Cuxhaven as well as from the shipping lane north and north-east of Neuwerk.

Figure 12.20 shows the azimuthal distribution of the calculated NO_2 volume mixing ratios for both time periods. For both time periods, the VMRs calculated using the water vapor slant column density show the best agreement with the in-situ measurements. Substantial differences occur for northern wind directions. This is the direction, where measured NO_2 comes only from ships. As seen above, the shape of measured peaks of ship plumes deviate between MAX-DOAS and in-situ measurements due to the different measurement methods. Peaks appear to be higher for in-situ-measurements, because the MAX-DOAS measurement is always an average over a long distance and the plume fills only a certain part of the light path, explaining the deviations between the curves in Figure 12.20.

Figure 12.21 shows again the NO_2-VMRs for water vapor as a light path proxy, this time for all different azimuth angles. There are only slight differences between the various line of sights. The agreement with the in-situ data is very good for most wind directions and both time periods.
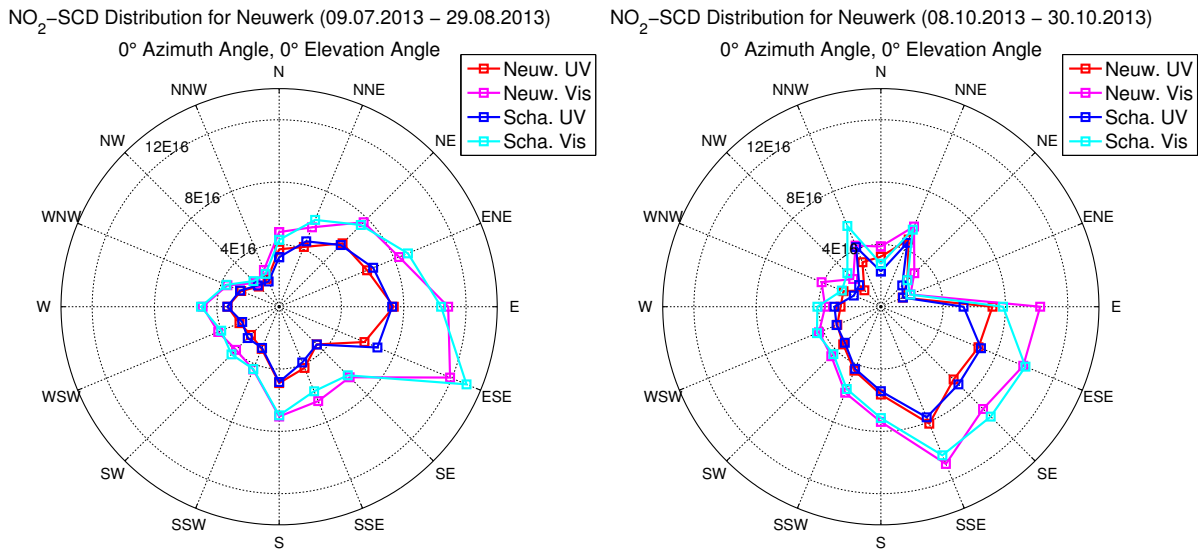
Figure 12.17.: Wind direction dependence of NO$_2$ slant column densities in the UV and visible spectral range measured on Neuwerk. Shown is the mean SCD measured in the main azimuth viewing direction (0°) at 0° elevation angle, using wind direction data from Neuwerk (reddish colors) and Scharhörn (blueish colors).

Figure 12.18.: Wind direction dependence of NO$_2$ slant column densities measured on Neuwerk with underlying map of the region [Image source: `http://www.bing.com/maps/` (01.04.2014)]
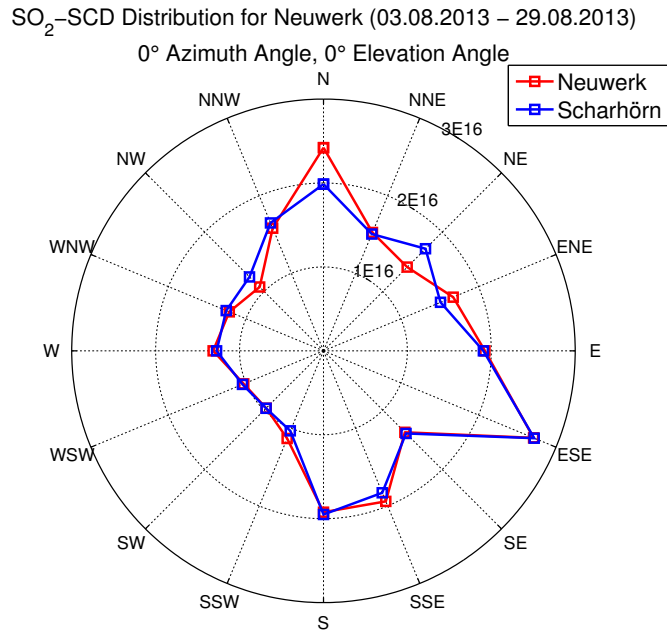
Figure 12.19.: Wind direction dependence of SO_2 slant column densities measured on Neuwerk. Shown is the mean SCD measured in the main azimuth viewing direction (0°) at 0° elevation angle, using wind direction data from Neuwerk (red) and Scharhörn (blue).
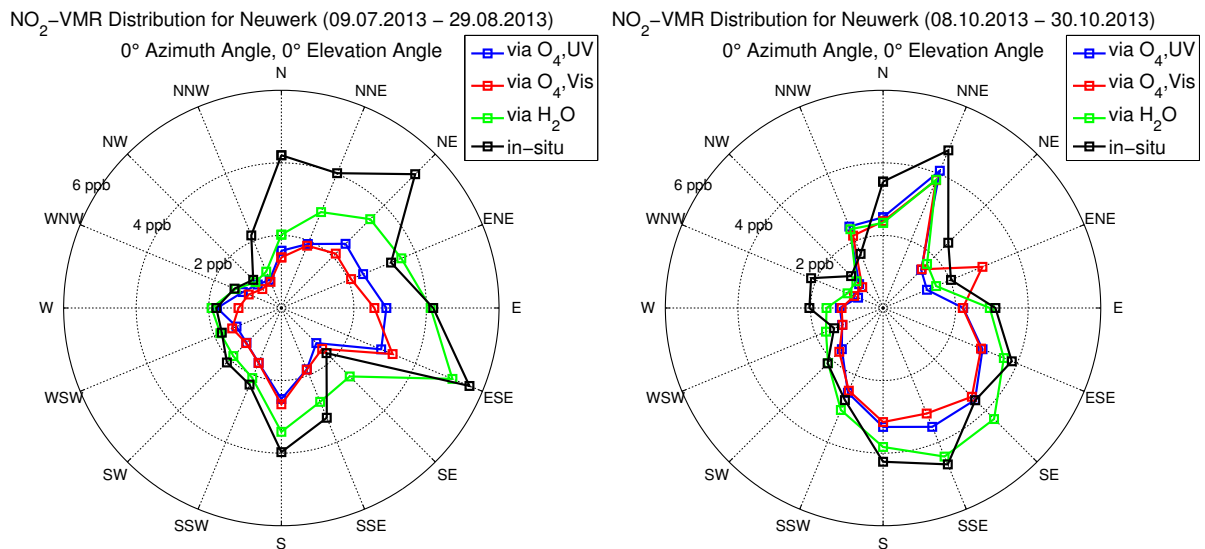
Figure 12.20.: Wind direction dependence of NO_2 volume mixing ratios measured on Neuwerk, calculated using the O_4 and H_2O slant column densities as a tracer for the effective light path. For comparison, also the corresponding in-situ data is shown.

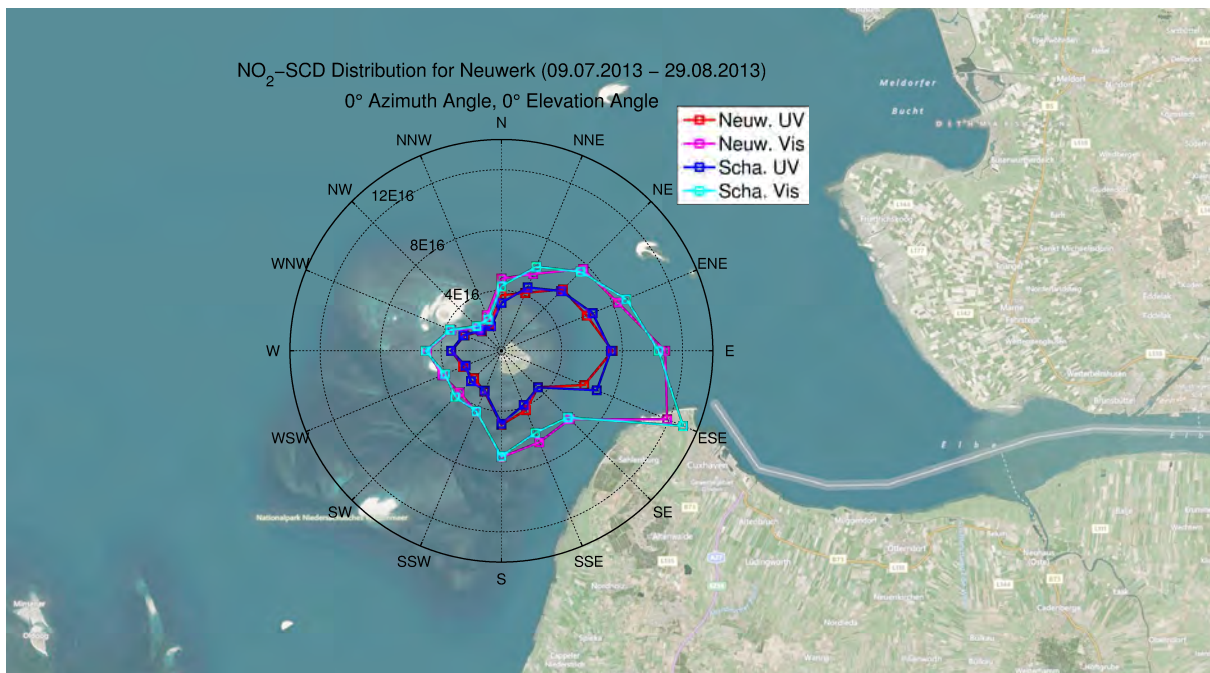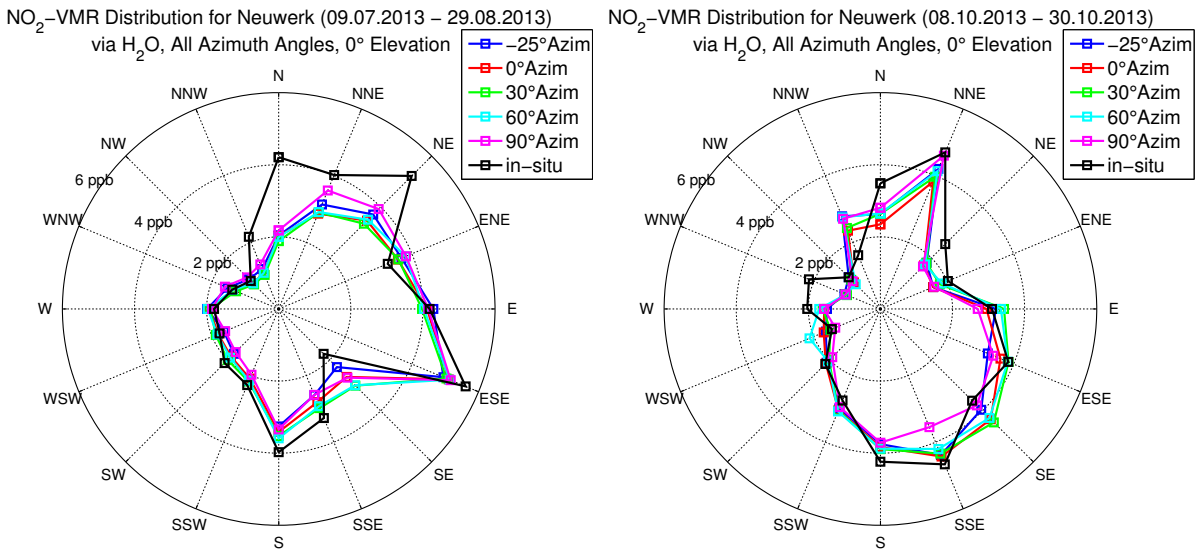Figure 12.21.: Wind direction dependence of NO_2 volume mixing ratios measured on Neuwerk in different azimuth angles and – for comparison – the corresponding in-situ data. The MAX-DOAS NO_2-VMRs are calculated using the water vapor slant column density as a tracer for the light path.

Figure 12.22 shows SO_2-VMRs calculated via the O_4-SCD for different azimuth angles (left sub-figure) as well as the geometric SO_2-VMR for the main viewing direction (right sub-figure). For comparison, also the in-situ measurements are shown.

The agreement between MAX-DOAS and in-situ values is much better if the O_4-SCD is used. This example demonstrates that this approach using a light path tracer gives better results than a simple geometric approximation.
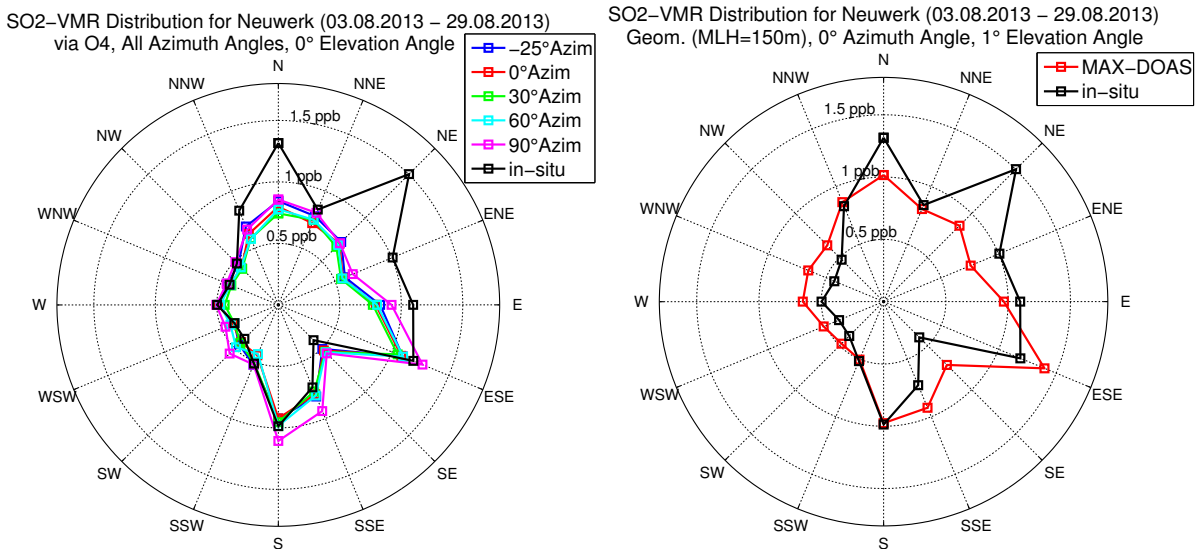
Figure 12.22.: Comparison between the MAX-DOAS and in-situ wind direction dependence of SO_2 volume mixing ratios measured on Neuwerk. The MAX-DOAS NO_2-VMRs in the left figure are calculated using the O_4-SCD as a tracer for the light path, in the right figure by using the geometric approximation.

12.6. Time Series Comparison

A two-month time series of MAX-DOAS as well as in-situ NO_2 volume mixing ratios is plotted in Figure 12.23. Although the MAX-DOAS values are slightly lower, both time series show a very consistent behavior. The same can be done for SO_2 (see Figure 12.24), but covering a different time period. This comparison shows also quite good agreement.
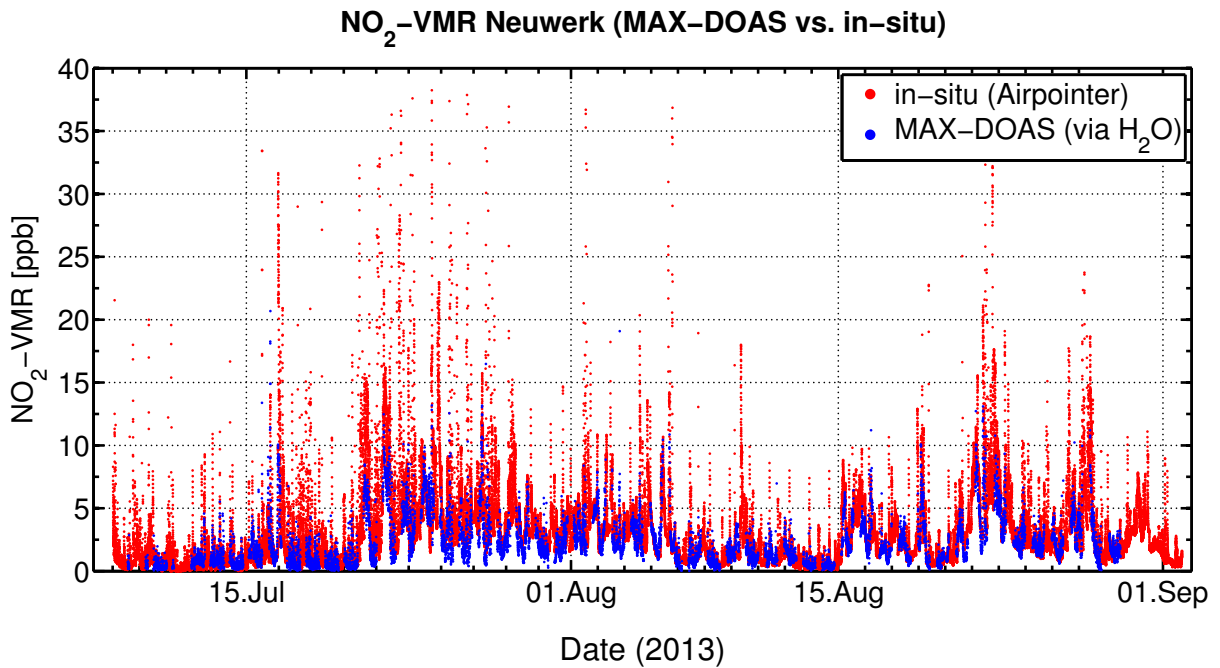
Figure 12.23.: Comparison of MAX-DOAS NO_2-VMR (via H_2O) and in-situ NO_2-VMR time series
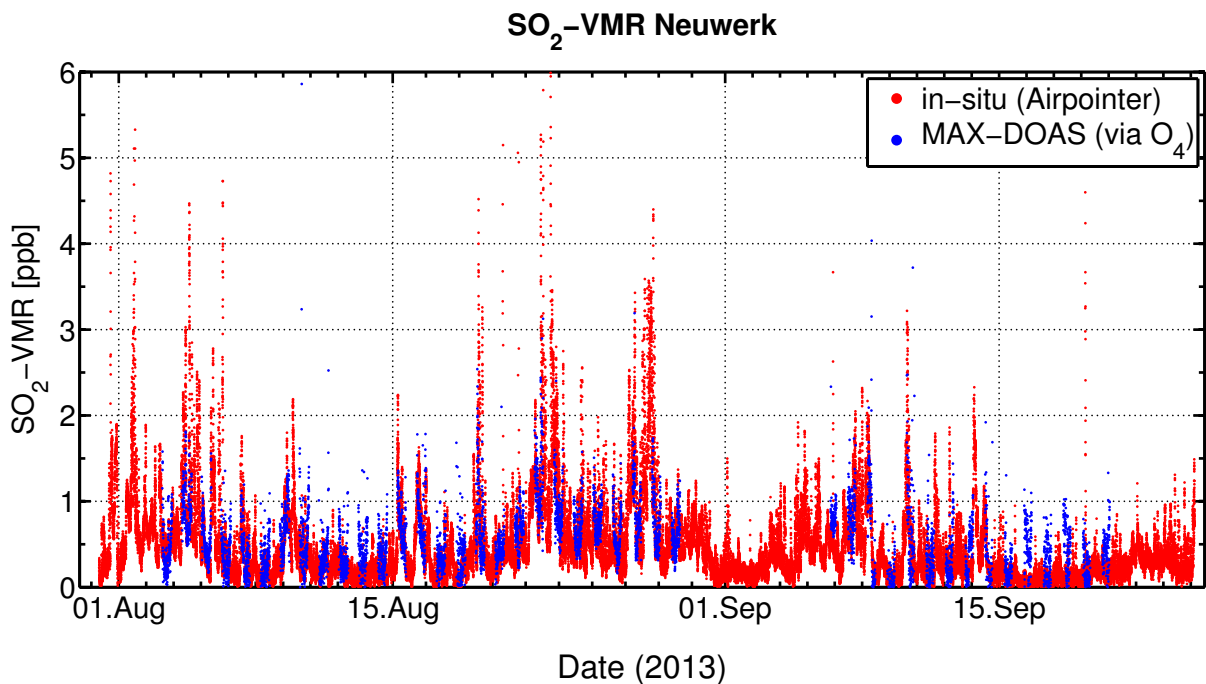
Figure 12.24.: Comparison of MAX-DOAS SO_2-VMR (via O_4) and in-situ SO_2-VMR time series

12.7. Correlation Plots

Another possibility to compare MAX-DOAS measurements with in-situ data is to use a correlation plot as representation and to calculate correlation coefficients. In Figure 12.25 the correlation between the daily means of the in-situ NO_2 volume mixing ratios and the MAX-DOAS NO_2-VMRs determined by the various methods is shown. This daily means were calculated by averaging over all values between 6 AM and 6 PM (UTC) to account for the measurement time of the MAX-DOAS instrument during daylight. Although the best slope can be achieved by using the geometric approximation and assuming an appropriate mixing layer height, the values scatter a lot. The best correlation is gained if water vapor is used as a tracer for the light path, but
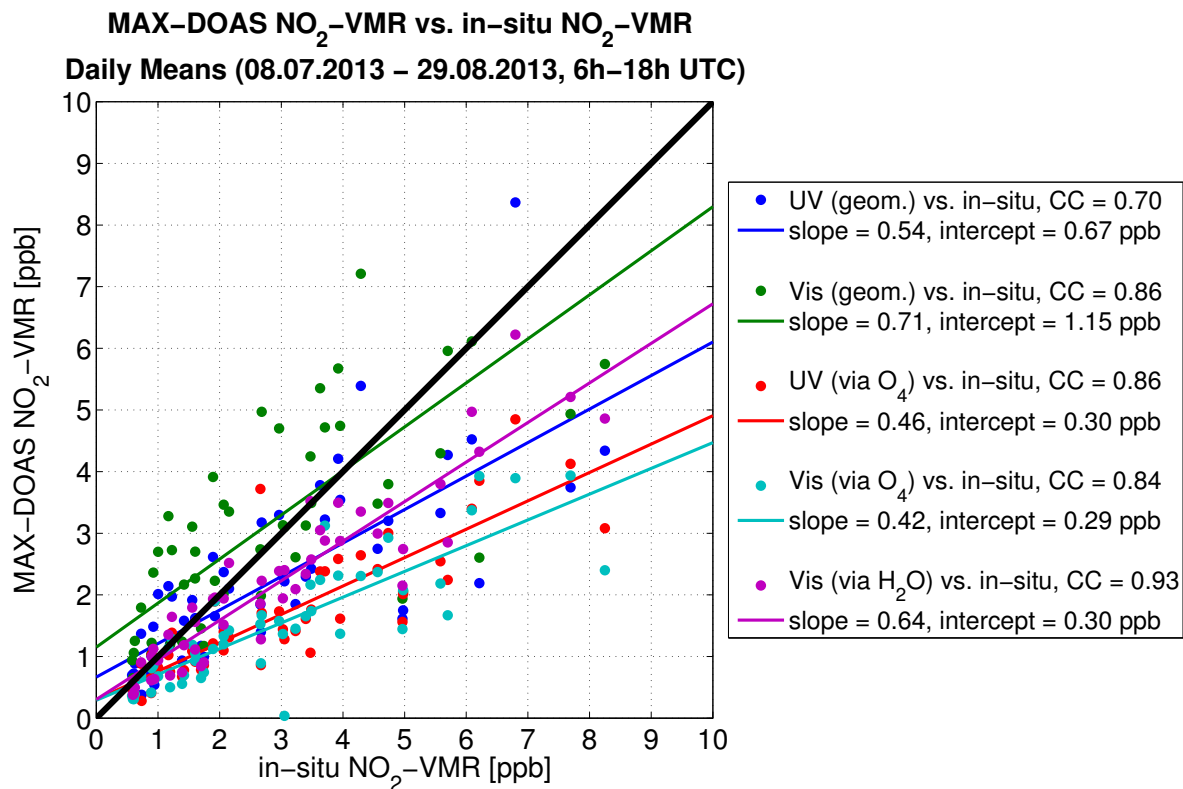
Figure 12.25.: Correlation plot displaying in-situ vs. MAX-DOAS NO_2-VMR daily means for all approaches to calculate the MAX-DOAS VMRs. The values for correlation coefficient (CC) as well as the coefficients of the linear fits are shown in the legend on the right. All MAX-DOAS measurements are taken in the main viewing direction (0° azimuth) for 0° (O_4,H_2O) or 1° elevation angle (geometric) with an assumed mixing layer height of 100 m.

The correlation between all single MAX-DOAS visible NO_2-VMRs for the different approaches can be seen in Figure 12.25 for a period of eleven days. This plot shows that the correlation between NO_2-VMRs calculated using O_4 and H_2O as tracers for the effective light path is very good. This confirms that both methods deliver a consistent progression of NO_2-VMRs, but differ by a scaling factor. Compared to the simple geometric approximation, there is much less scatter if a light path tracer is used.
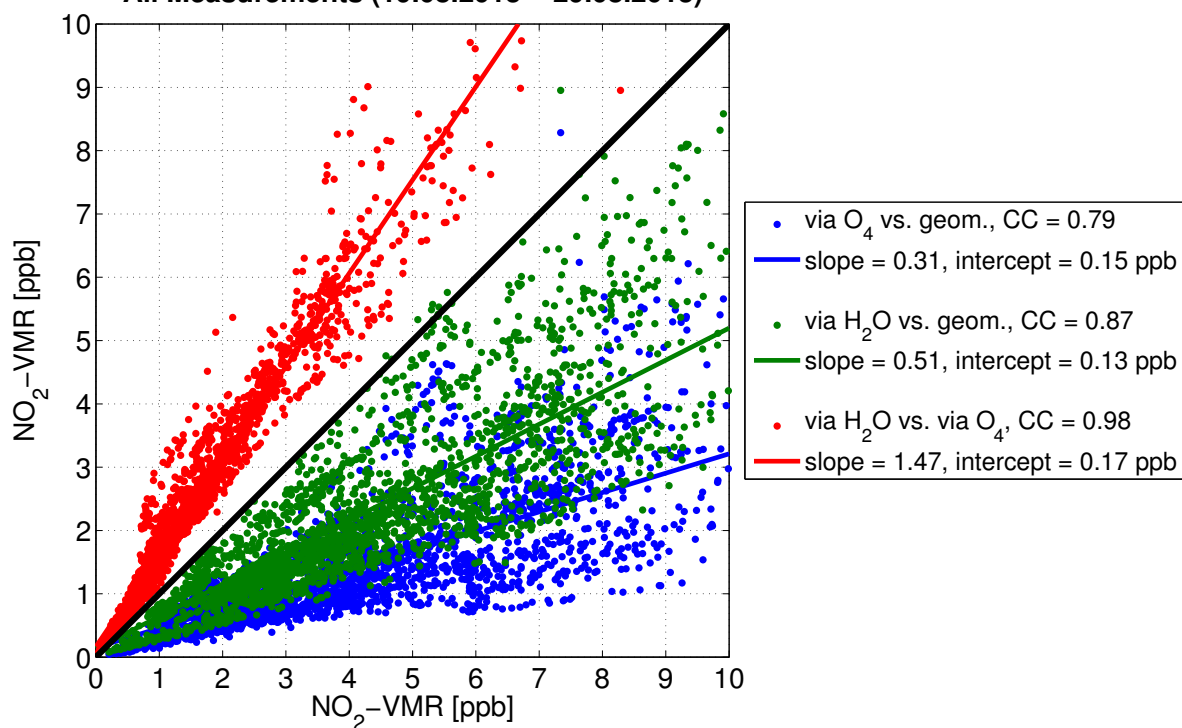
Figure 12.26.: Correlation plot displaying MAX-DOAS NO_2-VMR for all approaches. The values for correlation coefficient (CC) as well as the coefficients of the linear fits are shown in the legend on the right. All MAX-DOAS measurements are taken in the main viewing direction (0° azimuth) for 1° elevation angle. The assumed mixing layer height for the geometric approximation is 100 m.

13. Summary, Conclusions and Outlook

A SO_2 fitting retrieval study for MAX-DOAS data measured on Neuwerk and in Wedel has been carried out, including a systematically analysis of different trace gas cross-sections, polynomial degrees from 2 to 5 and all possible fitting windows in the wavelength range of 306 to 350 nm. Using a fitting window of 307.5 to 328 nm, including the cross-sections for SO_2 (293 K), Ring, O_3 (223 K and 273 K) and NO_2 (298 K) and using a polynomial degree of 5 yields the best results for the evaluated days and was therefore used to retrieve SO_2 slant column densities from the MAX-DOAS measurements in Wedel and on Neuwerk.

For both measurement sites the measured NO_2 and SO_2 SCDs have been evaluated, showing ship emission peaks as well as background pollution. Thereby, it has been shown that ground-based MAX-DOAS instruments used are capable of measuring shipping emissions of NO_2 and SO_2.

Volume mixing ratios have been calculated from the measured SCDs with different approaches: applying a simple geometric approximation (in Wedel and on Neuwerk) and for Neuwerk additionally by using other trace gas SCDs as a tracer for the effective light path. For the first time, the water vapor SCD has been used as such a tracer. The retrieved VMRs were than compared to in-situ VMRs measured by the Airpointer device from MLU.

In Wedel, a consistent behaviour for a three-week time series and a good agreement on the daily measured values, especially for the background pollution, have been found. The ship emission peaks measured with the MAX-DOAS were substantially smaller than the in-situ peaks, which can be explained by the different characteristics of the measurement techniques: The in-situ device measures at one fixed location directly inside the plume, getting really high values. The MAX-DOAS technique averages over a certain light path in which the plume fills only a small part.

For Neuwerk the approach to calculate VMRs by using other trace gas SCDs to estimate the light path length, has shown much better results than a simple geometric approximation. Using the water vapor SCD (retrieved in the visible), performed best for NO_2, yielding a three-month time series of NO_2, that is very consistent to the in-situ measurements and a very good correlation of the daily means. Using both the O_4-SCDs in UV and visible as a tracer gives values that coincide very well with each other, showing that the light path difference between UV and visible can be compensated for, but yields too low values compared to the in-situ measurements.

For SO_2, which is retrieved only in the UV, using the O_4-SCD gives a good agreement with in-situ values for a two-month time series, far better than the geometric approximation.

Incorporating the AIS (Automatic Identification System) ship position data and wind speed and direction measurements, it has been shown that the MAX-DOAS instruments at both sites can measure ship emission plumes, that in the majority can be allocated to single ships. Using the horizontal azimuth scan mode, the horizontal movement directions of the ships and the exhausted plumes can be easily identified on the river Elbe as well as on the shipping lane close to Neuwerk in the North Sea. Due to the shorter

distance to the ships, in Wedel also the vertical distribution of ship plumes reaching into various heights depending on the size of the ship can be studied.

The evaluation of the wind direction dependence of the measured trace gases NO_2 and SO_2 has shown that high mean values were measured from directions where background air pollution is emitted. In Wedel, these emissions were coming mostly from Wedel and the city of Hamburg, incorporating urban road traffic as well as industry. On Neuwerk high mean values were measured for wind coming from the coast, especially for the direction of Cuxhaven, but also from the shipping channel in the mouth of the river Elbe that runs very close to Cuxhaven. For this long-term wind direction dependence analysis also the approach of taking the H_2O-SCD for NO_2 and the O_4-SCD for SO_2 as a light path tracer gives the best agreement with the in-situ VMRs.

As a result of the comparison between the MAX-DOAS instrument and the in-situ device, several advantages of using a MAX-DOAS for the measurement of NO_2 and SO_2 over the often-used in-situ devices have been identified: First, the MAX-DOAS instrument can measure the ship plumes even if the wind is blowing them away from the instruments, while the in-situ device always needs the appropriate wind direction to measure them. Second, the MAX-DOAS instruments is capable of measuring the horizontal and vertical distribution as well as movement of the plumes, while the in-situ device measures only values on a fixed location. For Neuwerk, where the distance between the emitting ships and the instruments is about 6 km, the MAX-DOAS also shows sharper emission peaks, that can be more easily allocated to single ships.

Finally, for the first time it was possible to determine emission ratios of NO_2/SO_2 for single ships with MAX-DOAS measurements, allowing to compare the relative emission rates of NO_2 and SO_2 of different ships. In Wedel, values in the range of 0.09 to 1.23 have been measured, which is about one order of magnitude lower than those measured on Neuwerk (ranging from 1 to 11.5).

Recent studies (McLaren et al., 2012; Diesch et al., 2013) show a good agreement with the values measured on Neuwerk, which suggest the assumption, that the MAX-DOAS instrument in Wedel measures directly through the just-exhausted plumes, in which most of the emitted NO_x is still in the form of NO and had no time to be converted to NO_2. This assumption is supported by the observation, that for a lot of ship plumes that were measured repeatedly the NO_2/SO_2 ratio increases with time.

As an outlook, there is still a lot of work to be done on the data sets for Neuwerk and Wedel. Both data sets grow continuously with on-going measurements. Consequently, future studies can provide more information on the seasonality of the observed trace gases. There was a short inter-comparison campaign with an imaging DOAS (iDOAS) system mounted next to the MAX-DOAS in April and May 2014 in Wedel. In addition to that, several ship cruises in the North and Baltic Sea on the Irish research vessel *Celtic Explorer* have been performed during the MeSmarT project until now, the last in August and September 2013 where I also participated, providing data in a region with no other local sources than shipping.

For the SO_2 fitting retrieval study, a further evaluation using synthetic spectra calculated with a radiative transfer model can be carried out.

For the determined NO_2/SO_2 emission ratios, a systematic evaluation of the whole data set will give a better statistic and also a comparison to the in-situ values as well as the iDOAS measurements would be useful to gain more information on the chemistry in the evolving plumes.

In Wedel, where the emissions can be measured in all elevation angles, a profile retrieval and a comparison to the iDOAS instrument, which measures in several elevations at the same time, will give better knowledge on the vertical distribution of the plumes.

Modelling of the plume distribution and movement on Neuwerk, incorporating the measured wind data, would help to better understand the measurements on Neuwerk.

A. Appendix

Table A.1.: Fit settings for NO_2

Parameter	NO_2 (UV)	NO_2 (Vis)
Fitting window	338–370 nm	425–490 nm
Polynomial degree	5	5
Straylight correction	Constant	Constant
Zenith reference	Closest	Closest
O_3	223 K (Bogumil et al., 2003)	223 K (Bogumil et al., 2003)
NO_2	298 K (Vandaele et al., 1996)	298 K (Vandaele et al., 1996)
O_4	Hermans et al., unpublished	–
H_2O	–	HITEMP (Rothman et al., 2010)
HCHO	297 K (Meller and Moortgat, 2000)	–
Ring	NDSC 2003	NDSC 2003

Table A.2.: Fit settings for SO_2

Parameter	SO_2 (UV)
Fitting window	307.5–328 nm
Polynomial degree	5
Straylight correction	Constant
Zenith reference	Closest
O_3 (stratospheric)	223 K (Bogumil et al., 2003)
O_3 (tropospheric)	273 K (Bogumil et al., 2003)
NO_2	298 K (Vandaele et al., 1996)
SO_2	293 K (Bogumil et al., 2003)
Ring	GOMETRAN (Marco Vountas)

Bibliography

Beirle, S; Platt, U; von Glasow, R; Wenig, M, and Wagner, T. Estimate of nitrogen oxide emissions from shipping by satellite remote sensing. *Geophysical Research Letters*, 31(18):–, 2004. ISSN 0094-8276. doi: 10.1029/2004gl020312. URL `<GotoISI>://000224123000001`.

Bogumil, K; Orphal, J; Homann, T; Voigt, S; Spietz, P; Fleischmann, O.C; Vogel, A; Hartmann, M; Kromminga, H; Bovensmann, H; Frerick, J, and Burrows, J.P. Measurements of molecular absorption spectra with the SCIAMACHY pre-flight model: instrument characterization and reference data for atmospheric remote-sensing in the 230-2380 nm region. *Journal of Photochemistry and Photobiology A: Chemistry*, 157(2-3):167–184, May 2003. ISSN 10106030. doi: 10.1016/S1010-6030(03)00062-5. URL `http://linkinghub.elsevier.com/retrieve/pii/S1010603003000625`.

Böttcher, Jörg. *Handbuch Offshore-Windenergie: rechtliche, technische und wirtschaftliche Aspekte*. Oldenbourg, München, 2013. ISBN 3486715291 and 9783486715293.

Bovensmann, H; Burrows, J P; Buchwitz, M; Frerick, J; Noël, S; Rozanov, V V; Chance, K V, and Goede, A P H. SCIAMACHY: Mission Objectives and Measurement Modes. *Journal of the Atmospheric Sciences*, 56:127–150, 1999.

Brasseur, Guy P. *Atmospheric chemistry and global change: [a textbook prepared by scientists at the National Center for Atmospheric Research, Boulder]*. Topics in environmental chemistry. Oxford Univ. Press, New York, NY [u.a.], 1999. ISBN 0195105214.

Burrows, J P; Hölzle, E; Goede, A P H; Visser, H, and Fricke, W. SCIAMACHY - Scanning Imaging Absorption Spectrometer for Atmospheric Chartography. *Acta Astronautica*, 35:445–451, 1995.

Burrows, J P; Weber, M; Buchwitz, M; Rozanov, V; Ladstatter-Weissenmayer, A; Richter, A; DeBeek, R; Hoogen, R; Bramstedt, K; Eichmann, K U, and Eisinger, M. The global ozone monitoring experiment (GOME): Mission concept and first scientific results. *Journal of the Atmospheric Sciences*, 56(2): 151–175, 1999.

Burrows, John P; Platt, Ulrich, and Borrell, Peter. *The remote sensing of tropospheric composition from space*. Physics of earth and space environments. Springer, Berlin ; Heidelberg [u.a.], 2011. ISBN 978-3-642-14790-6 ; 978-3-642-14791-3.

Callies, J; Corpaccioli, E; Eisinger, M; Hahne, A, and Lefebvre, A. GOME-2 – Metop's Second-Generation Sensor for Operational Ozone Monitoring. *ESA Bulletin-European Space Agency*, 102:28–36, 2000.

Camy-Peyret, Claude and Vigasin, Andrei A. *Weakly Interacting Molecular Pairs: Unconventional Absorbers of Radiation in the Atmosphere: Unconventional Absorbers of Radiation in the Atmosphere*. Kluwer Academic Publishers, Dordrecht, 2003. ISBN 9781402015953.

Corbett, J. J. and Koehler, H. W. Updated emissions from ocean shipping. *Journal of Geophysical Research*, 108(D20):4650, 2003. ISSN 0148-0227. doi: 10.1029/2003JD003751. URL `http://doi.wiley.com/10.1029/2003JD003751`.

Corbett, James J; Winebrake, James J; Green, Erin H; Kasibhatla, Prasad; Eyring, Veronika, and Lauer, Axel. Mortality from ship emissions: a global assessment. *Environmental science & technology*, 41(24): 8512–8, December 2007. ISSN 0013-936X. URL `http://www.ncbi.nlm.nih.gov/pubmed/18200887`.

Darrin, Ann and O'Leary, Beth L. *Handbook of Space Engineering, Archaeology, and Heritage.* CRC Press, 2009. ISBN 1420084321.

Demtröder, Wolfgang. *Laserspektroskopie: Grundlagen und Techniken.* Springer, Berlin [u.a.], 5. edition, 2007. ISBN 354033792X and 9783540337928.

Demtröder, Wolfgang. *Experimentalphysik 1: Mechanik und Wärme.* Springer-Lehrbuch. Springer, Berlin [u.a.], 5. edition, 2008. ISBN 3540792945.

Demtröder, Wolfgang. *Experimentalphysik 2: Elektrizität und Optik.* Springer-Lehrbuch. Springer, Berlin [u.a.], 5. edition, 2009. ISBN 9783540682103.

Demtröder, Wolfgang. *Experimentalphysik 3: Atome, Moleküle und Festkörper.* Springer-Lehrbuch. Springer, Berlin [u.a.], 4. edition, 2010. ISBN 9783642039102.

Diesch, J.-M.; Drewnick, F.; Klimach, T., and Borrmann, S. Investigation of gaseous and particulate emissions from various marine vessel types measured on the banks of the Elbe in Northern Germany. *Atmospheric Chemistry and Physics*, 13(7):3603–3618, April 2013. ISSN 1680-7324. doi: 10.5194/acp-13-3603-2013. URL `http://www.atmos-chem-phys.net/13/3603/2013/`.

Eddy, J A. *The Sun, the Earth, and Near-Earth Space: A Guide to the Sun-Earth System.* Bernan Assoc, 2009. ISBN 9780160838088.

Emeis, Stefan. *Surface-based remote sensing of the atmospheric boundary layer.* Atmospheric and oceanographic sciences library ; 40. Springer, Dordrecht [u.a.], 2011. ISBN 9789048193394.

Endresen, Ø.; Sørgård, E.; Sundet, J. K.; Dalsøren, S. B.; Isaksen, I. S. A.; Berglen, T. F., and Gravir, G. Emission from international sea transportation and environmental impact. *Journal of Geophysical Research*, 108(D17):4560, 2003. ISSN 0148-0227. doi: 10.1029/2002JD002898. URL `http://doi.wiley.com/10.1029/2002JD002898`.

Eyring, V.; Köhler, H. W.; Lauer, A., and Lemper, B. Emissions from international shipping: 2. Impact of future technologies on scenarios until 2050. *Journal of Geophysical Research*, 110(D17):D17306, 2005a. ISSN 0148-0227. doi: 10.1029/2004JD005620. URL `http://doi.wiley.com/10.1029/2004JD005620`.

Eyring, V.; Köhler, H. W.; van Aardenne, J., and Lauer, A. Emissions from international shipping: 1. The last 50 years. *Journal of Geophysical Research*, 110(D17):D17305, 2005b. ISSN 0148-0227. doi: 10.1029/2004JD005619. URL `http://doi.wiley.com/10.1029/2004JD005619`.

Eyring, V.; Bovensmann, H.; Cionni, I.; Dall'Amico, M.; Franke, K.; Khlystova, I.; Klinger, C.; Lauer, A.; Paxian, A.; Righi, M., and Schreier, M. Impact of Ship Emissions on Atmosphere and Climate, SeaKLIM Final Report. Technical report, DLR, 2010a. URL `http://www.pa.op.dlr.de/SeaKLIM/SeaKLIM_Nachwuchsgruppe_Schlussbericht_FINAL.pdf`.

Eyring, Veronika; Isaksen, Ivar S.A.; Berntsen, Terje; Collins, William J.; Corbett, James J.; Endresen, Oyvind; Grainger, Roy G.; Moldanova, Jana; Schlager, Hans, and Stevenson, David S. Transport impacts on atmosphere and climate: Shipping. *Atmospheric Environment*, 44(37):4735–4771, December 2010b. ISSN 13522310. doi: 10.1016/j.atmosenv.2009.04.059. URL `http://linkinghub.elsevier.com/retrieve/pii/S1352231009003379`.

Fuglestvedt, Jan; Berntsen, Terje; Eyring, Veronika; Isaksen, Ivar; Lee, David S, and Sausen, Robert. Shipping emissions: from cooling to warming of climate-and reducing impacts on health. *Environmental science & technology*, 43(24):9057–62, December 2009. ISSN 0013-936X. doi: 10.1021/es901944r. URL `http://www.ncbi.nlm.nih.gov/pubmed/19924852`.

Gomez, L.; Navarro-Comas, M.; Puentedura, O.; Gonzalez, Y.; Cuevas, E., and Gil-Ojeda, M. Long-path averaged mixing ratios of O3 and NO2 in the free troposphere from mountain MAX-DOAS. *Atmospheric Measurement Techniques Discussions*, 6(5):8235–8267, September 2013. ISSN 1867-8610. doi: 10.5194/amtd-6-8235-2013. URL `http://www.atmos-meas-tech-discuss.net/6/8235/2013/`.

Grainger, J F and Ring, J. Anomalous Fraunhofer Line Profiles. *Nature*, 193:762, 1962.

Haken, Hermann and Wolf, Hans Christoph. *Atom- und Quantenphysik: Einführung in die experimentellen und theoretischen Grundlagen ; mit 32 Tabellen, 177 Aufgaben und vollständigen Lösungen.* Springer-Lehrbuch. Springer, Berlin [u.a.], 8. edition, 2004. ISBN 3540026215.

Haken, Hermann and Wolf, Hans Christoph. *Molekülphysik und Quantenchemie: Einführung in die experimentellen und theoretischen Grundlagen ; mit 43 Tabellen und 133 Aufgaben.* Springer-Lehrbuch. Springer, Berlin [u.a.], 5. edition, 2006. ISBN 3540303146 and 9783540303145.

Hecht, Eugene. *Optik.* Oldenbourg, München [u.a.], 4. edition, 2005. ISBN 3486273590.

Holton, James R. *An introduction to dynamic meteorology.* International geophysics series ; 88. Academic Press, Amsterdam [u.a.], 4. ed edition, 2004. ISBN 0123540151 and 012354016X.

Hönninger, G; von Friedeburg, C, and Platt, U. Multi axis differential optical absorption spectroscopy (MAX-DOAS). *Atmos. Chem. Phys.*, 4:231–254, 2004.

Janesick, James R. *Scientific Charge-Coupled Devices.* Press Monographs. SPIE Press, 2001. ISBN 9780819436986.

Lauer, A.; Eyring, V.; Hendricks, J.; Jöckel, P., and Lohmann, U. Global model simulations of the impact of ocean-going ships on aerosols, clouds, and the radiation budget. *Atmospheric Chemistry and Physics Discussions*, 7(4):9419–9464, July 2007. ISSN 1680-7375. doi: 10.5194/acpd-7-9419-2007. URL `http://www.atmos-chem-phys-discuss.net/7/9419/2007/`.

Lawrence, M G and Crutzen, P J. Influence of NOx emissions from ships on tropospheric photochemistry and climate. *Nature*, 402(6758):167–170, 1999. ISSN 0028-0836. doi: 10.1038/46013.

Lipson, Stephen G; Lipson, Henry S, and Tannhauser, David S. *Optik: mit 125 Aufgaben und vollständigen Lösungen.* Springer-Lehrbuch. Springer, Berlin [u.a.], 1997. ISBN 3540619127.

McLaren, Robert; Wojtal, Patryk; Halla, Jamie D.; Mihele, Cris, and Brook, Jeffrey R. A survey of NO2:SO2 emission ratios measured in marine vessel plumes in the Strait of Georgia. *Atmospheric Environment*, 46(2):655–658, January 2012. ISSN 13522310. doi: 10.1016/j.atmosenv.2011.10.044. URL `http://linkinghub.elsevier.com/retrieve/pii/S135223101101123X`.

Meller, Richard and Moortgat, Geert K. Temperature dependence of the absorption cross sections of formaldehyde between 223 and 323 K in the wavelength range 225-375 nm. *Journal of Geophysical Research: Atmospheres*, 105(D6):7089–7101, 2000. ISSN 2156-2202. doi: 10.1029/1999JD901074. URL `http://dx.doi.org/10.1029/1999JD901074`.

Noxon, J F. Nitrogen-Dioxide in Stratosphere and Troposphere Measured by Ground-Based Absorption Spectroscopy. *Science*, 189(4202):547–549, 1975.

Perner, D; Ehhalt, D H; Pätz, H W; Platt, U; Röth, E P, and Volz, A. OH - Radicals in the lower troposphere. *Geophysical Research Letters*, 3(8):466–468, 1976. ISSN 1944-8007. doi: 10.1029/GL003i008p00466. URL `http://dx.doi.org/10.1029/GL003i008p00466`.

Peters, Enno. *Improved MAX-DOAS measurements and retrievals focused on the marine boundary layer*. Phd thesis, Universität Bremen, 2013.

Pfeilsticker, Klaus; Erle, Frank, and Platt, Ulrich. Absorption of Solar Radiation by Atmospheric O 4. *Journal of the Atmospheric Sciences*, 54(7):933–939, April 1997. ISSN 0022-4928. doi: 10.1175/ 1520-0469(1997)054<0933:AOSRBA>2.0.CO;2. URL `http://journals.ametsoc.org/doi/abs/10.1175/1520-0469%281997%29054%3C0933%3AAOSRBA%3E2.0.CO%3B2`.

Pinardi, Gaia and Hendrick, F. On the use of the MAX-DOAS technique for the validation of tropospheric NO2 column measurements from satellite. *. . . satellite conference . . .* , 1(2), 2008.

Platt, Ulrich and Stutz, Jochen. *Differential optical absorption spectroscopy*. Physics of Earth and Space Environments. Springer, Berlin ; Heidelberg, 2008. ISBN 3-540-21193-4 ; 978-3-540-21193-8 ; 978-3-540-75776-4.

Richter, A.; Begoin, M.; Hilboll, A., and Burrows, J. P. An improved NO2 retrieval for the GOME-2 satellite instrument. *Atmospheric Measurement Techniques*, 4(6):1147–1159, June 2011. ISSN 1867-8548. doi: 10.5194/amt-4-1147-2011. URL `http://www.atmos-meas-tech.net/4/1147/2011/`.

Richter, Andreas. *Absorptionsspektroskopische Messungen stratosphärischer Spurengase über Bremen, 53° N*. Phd thesis, Universität Bremen, Göttingen, 1997.

Richter, Andreas; Eyring, Veronika; Burrows, John P; Bovensmann, Heinrich; Lauer, Axel; Sierk, Bernd, and Crutzen, Paul J. Satellite measurements of NO2 from international shipping emissions. *Geophys. Res. Lett.*, 31:L23110, 2004. ISSN 0094-8276. doi: 10.1029/2004GL020822.

Roedel, Walter and Wagner, Thomas. *Physik unserer Umwelt: die Atmosphäre*. Springer, Berlin [u.a.], 4. edition, 2011. ISBN 9783642157288.

Rothman, L.S.; Gordon, I.E.; Barber, R.J.; Dothe, H.; Gamache, R.R.; Goldman, A.; Perevalov, V.I.; Tashkun, S.a., and Tennyson, J. HITEMP, the high-temperature molecular spectroscopic database. *Journal of Quantitative Spectroscopy and Radiative Transfer*, 111(15):2139–2150, October 2010. ISSN 00224073. doi: 10.1016/j.jqsrt.2010.05.001. URL `http://linkinghub.elsevier.com/retrieve/pii/S002240731000169X`.

Schönhardt, A.; Altube, P.; Gerilowski, K.; Krautwurst, S.; Hartmann, J.; Meier, a. C.; Richter, A., and Burrows, J. P. A wide field-of-view imaging DOAS instrument for continuous trace gas mapping from aircraft. *Atmospheric Measurement Techniques Discussions*, 7(4):3591–3644, April 2014. ISSN

1867-8610. doi: 10.5194/amtd-7-3591-2014. URL `http://www.atmos-meas-tech-discuss.net/7/3591/2014/`.

Seinfeld, John H and Pandis, Spyros N. *Atmospheric chemistry and physics: from air pollution to climate change.* Wiley, Hoboken, NJ, 2. edition, 2006. ISBN 0471720186 and 9780471720188 and 0471720178 and 9780471720171.

Solomon, Susan; Schmeltekopf, Arthur L., and Sanders, Ryan W. On the interpretation of zenith sky absorption measurements. *Journal of Geophysical Research*, 92(D7):8311, 1987. ISSN 0148-0227. doi: 10.1029/JD092iD07p08311.

Stull, Roland B. *An introduction to boundary layer meteorology.* Number 13 in Atmospheric sciences library ; 13. Kluwer, Dordrecht [u.a.], repr. edition, 1994. ISBN 90-277-2768-6 ; 90-277-2769-4 ; 978-90-277-2768-8 ; 978-90-277-2769-5.

Vandaele, A C; Hermans, C; Simon, P C; Roozendael, M Van; Guilmot, J M; Carleer, M, and Colin, R. Fourier Transform Measurement of NO_2 Absorption Cross-Section in the Visible Range at Room Temperature. *J. Atmos. Chem.*, 25:289–305, 1996.

Wagner, T.; Ibrahim, O.; Shaiganfar, R., and Platt, U. Mobile MAX-DOAS observations of tropospheric trace gases. *Atmospheric Measurement Techniques*, 3(1):129–140, February 2010. ISSN 1867-8548. doi: 10.5194/amt-3-129-2010. URL `http://www.atmos-meas-tech.net/3/129/2010/`.

Wayne, Richard P. *Chemistry of atmospheres: an introduction to the chemistry of the atmospheres of earth, the planets, and their satellites.* Oxford Univ. Press, Oxford [u.a.], 3. edition, 2006. ISBN 019850375X and 9780198503750.

Wittrock, F; Oetjen, H; Richter, A; Fietkau, S; Medeke, T; Rozanov, A, and Burrows, J P. MAX-DOAS measurements of atmospheric trace gases in Ny-Ålesund - Radiative transfer studies and their application. *Atmos. Chem. Phys.*, 4:955–966, 2004.

Wittrock, Folkard. *The retrieval of oxygenated volatile organic compounds by remote sensing techniques.* Phd thesis, Universität Bremen, 2006.

Eigenständigkeitserklärung

Ich versichere hiermit, dass ich die vorliegende Arbeit mit dem Titel:

"Retrieval of Shipping Emissions from MAX-DOAS Measurements"

————

"Ableitung von Schiffsemissionen aus MAX-DOAS-Messungen"

selbstständig verfasst und keine anderen als die angegebenen Quellen und Hilfsmittel verwendet habe. Die Stellen, die anderen Werken (dazu zählen auch Internetquellen) dem Wortlaut oder dem Sinn nach entnommen sind, wurden durch die Angabe der Quelle als solche kenntlich gemacht.

Die Zeichnungen oder Abbildungen in dieser Arbeit sind von mir selbst erstellt worden oder mit einem entsprechenden Quellennachweis versehen.

Bremen, 16.05.2014

André Seyler